Ultrafast Optical Pulse Manipulation in Three Dimensional-Resolved Microscopic Imaging and Microfabrication

by

Daekeun Kim

B.S. Mechanical Design and Production Engineering
Seoul National University, 1993

M.S. Mechanical Design and Production Engineering
Seoul National University, 1995

SUBMITTED TO THE DEPARTMENT OF MECHANICAL ENGINEERING IN PARTIAL FULFILLMENT OF THE REQUIREMENTS FOR THE DEGREE OF

DOCTOR OF PHILOSOPHY IN MECHANICAL ENGINEERING
AT THE
MASSACHUSETTS INSTUTUTE OF TECHNOLOGY

ARCHIVES

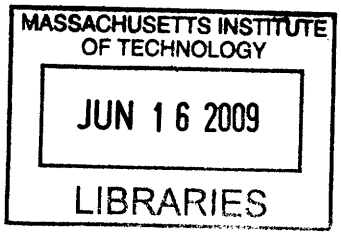

JUNE 2009

© 2009 Daekeun Kim. All rights reserved

The author hereby grants to MIT permission to reproduce and to distribute publicly paper and electronic copies of thesis document in whole or part in any medium now known or hereafter created

Signature of Author: _____
Department of Mechanical Engineering
May 14, 2009

Certified by: _____
Peter T. C. So
Professor of Mechanical Engineering and Biological Engineering
Thesis Supervisor

Accepted by: _____
David E. Hardt
Professor of Mechanical Engineering
Chairman, Committee for Graduate Students

Ultrafast Optical Pulse Manipulation in Three Dimensional-Resolved Microscopic Imaging and Microfabrication

by

Daekeun Kim

Submitted to the Department of Mechanical Engineering
on May 22, 2009 in Partial Fulfillment of the
Requirements for the Degree of Doctor of Philosophy in
Mechanical Engineering

ABSTRACT

The availability of lasers with femtosecond, ultrafast light pulses provides new opportunities and challenges in instrument design. This thesis addresses three aspects of utilizing ultrafast light pulses in two-photon excitation microscopy. First, optical fibers are routinely used in many optical instruments but their use in two-photon microscopy is very limited. As ultrafast light pulses propagate through conventional fiber optics, light pulses are dispersed and broadened, as a result of nonlinear interactions between light and material. Two-photon excitation efficiency is reduced with pulse broadening. The recent development of photonic crystal fibers allows unprecedented control of light properties through them. This thesis provides a thorough quantitative characterization of different conventional optical fibers and photonic crystal fibers enabling better utilization of these fibers for two-photon microscopic imaging. Second, two-photon microscopic imaging is relatively slow due to the sequential nature of raster scanning. Several groups have recently sought to overcome this limitation by developing a 3D-resolved wide-field two-photon microscope using the concept of temporal focusing that is based on manipulating the dispersion of ultrafast light pulses spatially. However, the existing temporal focusing systems have poor optical sectioning capability and, due to a shortage of illumination power, low actual frame rate. In this thesis, a comprehensive mathematical model is derived for temporal focusing two-photon microscope taking key instrument design parameters into account. By optimizing instrument design and the use of high two-photon cross section quantum dots, we demonstrate single quantum dot imaging at micron level resolution at video rate. Lastly, we realize that the temporal focus concept may also be used for microfabrication. A prototype three-dimensional lithographic microfabrication system is developed and micropatterning capability based on photobleaching process is demonstrated.

Thesis Supervisor: Peter T. C. So
Title: Professor of Mechanical Engineering and Biological Engineering

Acknowledgement

During my stay at MIT, I have had a lot of assistance as well as memorable experiences. While it is almost impossible to express my gratitude to everyone who helped me finish my Ph.D. program, I would like to mention some of them here.

First, I would like to thank Prof. Peter T. C. So, my thesis advisor. For the past six and a half years, he has supported my research and thesis and provided me with his insight and intuition whenever I was stuck in my research. Moreover, he has frequently advised me about my future career in academia. I thank my thesis committee members, Prof. Martin L. Culpepper, Prof. Michael S. Feld, and Prof. Guillermo J. Tearney, who gave me advice on my thesis research. I would also like to acknowledge Prof. Thomas Sherridan, my former research advisor. He had supported my research for a while before I joined Prof. So's Lab. I would like to express my gratitude to Prof. Kyo Il Lee, my M.S. advisor at Seoul National University. I cannot list all the names of colleagues I have met at Prof. So's Lab, but I deeply appreciate useful discussions with them. I should thank Dr. Hyungsuk Lee, Yongdae Shin, Dr. Won Shik Choi, and Seungeun Oh for preparing samples and invaluable discussions. Without their help, my thesis would still be in limbo.

I also acknowledge Korean Graduate Student Association in Mechanical Engineering and Korean Graduate Student Association at MIT where I met so many good friends. I would like to express special gratitude to Dr. Se June Hong and his family. They have invited me to all the events and occasions to celebrate, and gave me emotional support when I was in trouble. I also appreciate Dr. Hong's being my thesis reader.

I should never miss my parents, Yong Teak Kim and Sook Ja Park, who never ceased to support me from the day I was born. They have believed in my ability to accomplish my work at MIT, and I could not be what I am now without their endless love. I have and will always love and respect them. I am also grateful to my parents-in-law, Dr. Myung Chey and Kwang Ja Lee. They have always had the trust and patience waiting for me to finish my degree. I was not alone at MIT since my younger brother, Dr. Taehyun Kim, and his wife, Dr. Jooyoung Kwak, were at the same campus. I thank them for the good times we had in Cambridge and for helping me survive at MIT.

Lastly, I would like to express deep thanks to my lovely wife, Jung In Chey. She has always supported whatever I was doing, helped me with whatever decisions I had to make, and cheered me up whenever I was down and low. She is a wife, a partner, and an advisor in my life. As a thesis reader, she has given me a lot of advice on my writing. I do not think I could ever have finished my Ph.D. program without her. Most importantly, I acknowledge our first baby due this September.

I dedicate my thesis to my family.

Table of Contents

List of Figures

List of Tables

Abbreviations

2D	two-dimensional
3D	three-dimensional
AOM	acousto-optic modulator
BS	beam splitter
CCD	charge-coupled device
CMOS	complementary metal oxide semiconductor
CPN	conjugated polymer nanoparticle
CW	continuous-wave
D&C	divide and conquer
DMEM	Dulbecco's modified eagle medium
DRWFI	depth-resolved wide-field illumination
DLP	digital light processor
DMD	digital mirror device
DPBS	Dulbecco's phosphate buffered saline
DPSS	diode-pumped solid-state
EUS	endoscopic ultrasound
FBS	fetal bovine serum
FCS	fluorescence correlation spectroscopy
FOV	field of view
FROG	frequency-resolved optical gating
FWHM	full-width-at-half-maximum
GDD	group delay dispersion
GFP	green fluorescence protein
GI	gastrointestinal
GRIN	graded index
GVD	group velocity dispersion
iCCD	intensified charge-coupled device
ICS	image correlation spectroscopy

ICCS	image cross-correlation spectroscopy
k-ICS	k-space image correlation spectroscopy
MA	micromirror array
MEMS	micro-electro-mechanical system
MMM	multifocal multiphoton microscopy
MSD	mean square displancement
MTF	modulation transfer function
MTIR	modified total internal reflection
μTM	microtransfer molding
NA	numerical aperture
NIR	near infrared
OCT	optical coherence tomography
OPA	optical parametric amplifier
QD	quantum dot
QWP	quarter-wave plate
PALM	photo-activated localization microscopy
PBG	photonic bandgap effect
PBS	polarization beam splitter
PCF	photonic crystal fiber
PMT	photomultiplier tube
PSF	point spread function
RI	refractive index
SLM	spatial light modulator
SNR	signal-to-noise-ratio
SPM	self-phase modulation
SPT	single particle tracking
STICS	spatio-temporal image correlation spectroscopy
STORM	stochastic optical reconstruction microscopy
SWDRWFI	standing-wave depth-resolved wide-field illumination
TIR	total internal reflection
TIRFM	total internal reflection fluorescence microscopy

TOD	third order dispersion
TPE	two-photon excitation
TPM	two-photon excitation fluorescence microscopy
UV	ultraviolet

Chapter 1

Introduction

The advent of ultrafast laser technology has enabled the observation of the nonlinear optical processes that occur when electric field interacts strongly with materials. For several decades, ultrafast lasers producing femtosecond optical pulses have found applications in the fields such as telecommunication and biomedicine. Focusing on the use ultrafast optical pulses for microscopic imaging, the use of femtosecond pulses has inherent difficulties and potential opportunities. The main difficulty is due to the fact that the strong electric field of ultrafast optical pulses can cause unintended nonlinear interactions in materials, resulting in processes such as dispersion and self-phase modulation (SPM). Nonetheless, ultrafast lasers enable many new imaging modalities based on nonlinear spectroscopy such as multiphoton fluorescence excitation [1], second and higher harmonic generation [2], coherent anti-stoke and resonance Raman imaging [3]. Among these modalities, two-photon excitation fluorescence microscopy (TPM) is one of the most powerful and versatile tools for biomedical investigation. Within the field of TPM, the broad spectral bandwidth of ultrafast light pulse further provides the opportunity for coherent control [4] offering the potential for selective excitation of fluorophores [5], modifying two-photon excitation cross section [6], and reducing photobleaching [7]. Manipulating pulse spectral profile spatially further enables novel focusing and scanning mechanisms.

In this chapter, some basic characteristics of ultrafast optical pulse and some methods for their manipulation are introduced. The basic concept and instrument design for TPM are briefly discussed. Conventional TPMs obtain depth resolution based on spatial focusing; the concept of temporal focusing will be introduced and its application for wide-field two-photon imaging will be discussed. Finally, the motivation of the research and the scope of this thesis are described.

1.1 Ultrafast Optical Pulse

Ultrafast optical pulse is defined as electromagnetic wave with pulse width that is on the order of femtosecond (10^{-15} sec). It is a wave packet of monochromatic waves and has ultrahigh peak power in picosecond or femtosecond range from 20 kW to 70 GW. Optical pulse is called chirp-free or transform-limited pulse when all the waves in the pulse are in-phase. This type of pulse has the shortest pulse duration at a given bandwidth. Time-bandwidth product is the product of temporal duration and spectral bandwidth of the pulse, and it depends on the envelope of the optical pulse (it is typically considered to be either a Gaussian or a hyperbolic secant squared function.). Nonlinear optical processes require high electric field strength and were demonstrated with the invention of the laser [8, 9]. With the advent of femtosecond pulsed lasers in 1990s [10], the application of nonlinear optical processes for biomedical applications became more routine. Figure 1.1 presents the typical spectral-temporal profiles of a transform-limited optical pulse that has a Gaussian temporal profile with a full-width-at-half-maximum (FWHM) of 100 fs.

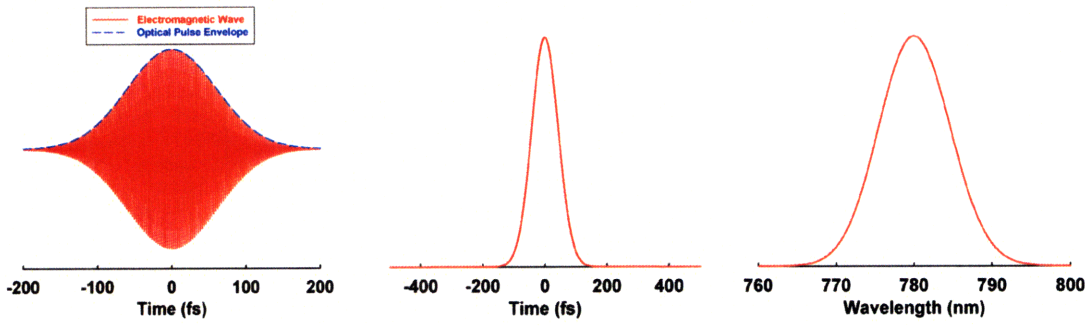

Figure 1.1 Numerical simulation of a transform-limited ultrafast optical pulse: (a) electromagnetic field distribution in time (b) intensity profile in time and (c) optical spectrum distribution in wavelength.

One of the limitations of using ultrafast optical pulse is the difficulty in maintaining its shape temporally and spectrally. Its sensitivity to dispersion results in the pulse broadening. Pulse broadening is a major limitation in ultrafast pulse delivery using waveguide for telecommunication where the carrier optical frequency should be the near zero dispersion band. Figure 1.2 shows the simulation of pulse broadening induced by the group delay dispersion (GDD). However, dispersion does not always lead to negative effects. Fourier transform

femtosecond pulse shaping can be realized by controlling the dispersion with diffraction grating pair, and the ultrafast optical pulse shape is modified with spatial light modulator (SLM) in its Fourier plane [11]. (See figure 1.3)

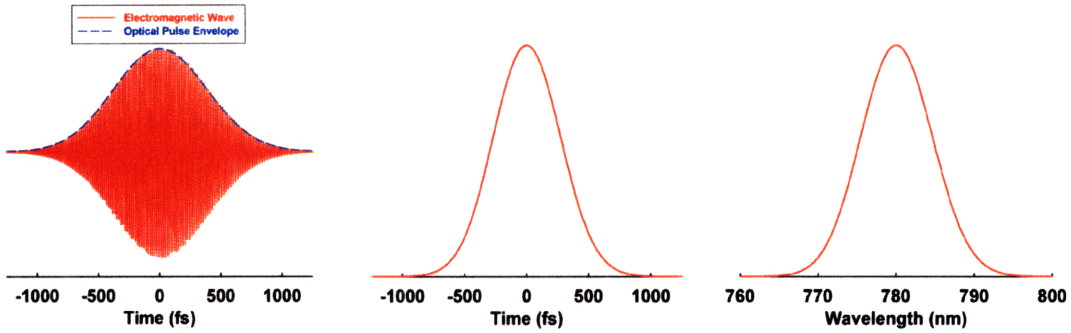

Figure 1.2 Numerical simulation of pulse broadening due to dispersion: (a) electromagnetic field distribution in time (b) intensity profile in time and (c) optical spectrum distribution in wavelength. Dispersion is resulted from transmitting through 0.5 m of fused silica that has a GVD parameter of 378.27 fs^2/cm.

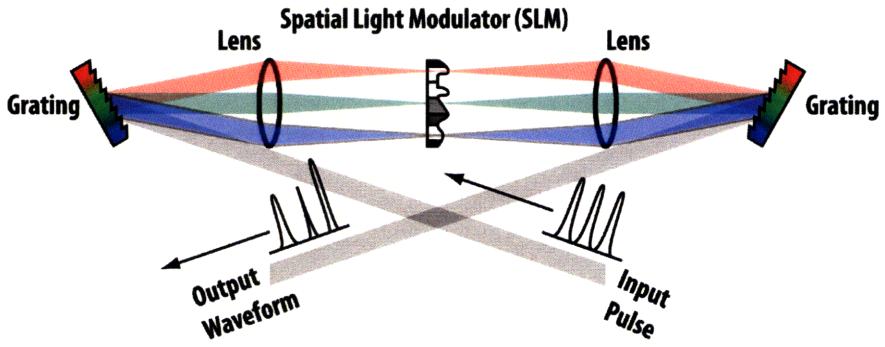

Figure 1.3 Fourier transform femtosecond pulse shaping with SLM

1.2 Dispersion

Dispersion is defined in two different ways: dispersion in time and dispersion in space. The former is any phenomenon associated with the propagation of individual waves at speeds that depend on their wavelengths or optical frequencies in wave motions (See figure 1.4). It generally happens when the optical pulse propagates in the dispersive media such as lens and optical fiber. The latter is the separation of light into colors by refraction or diffraction with the formation of a

spectrum (See figure 1.5) such as using a prism (refractive element) or a diffraction grating (diffractive element).

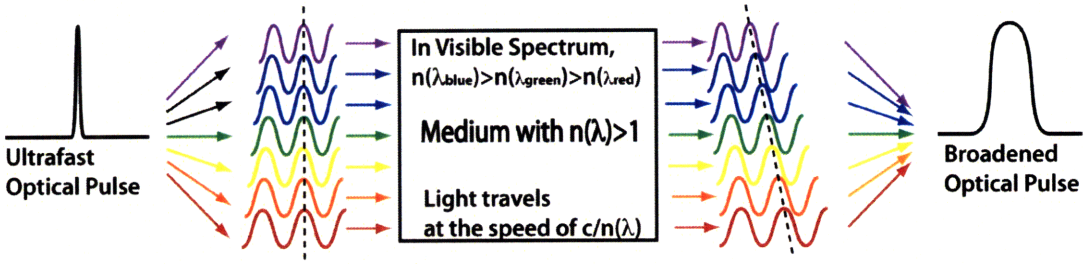

Figure 1.4 Dispersion in time.

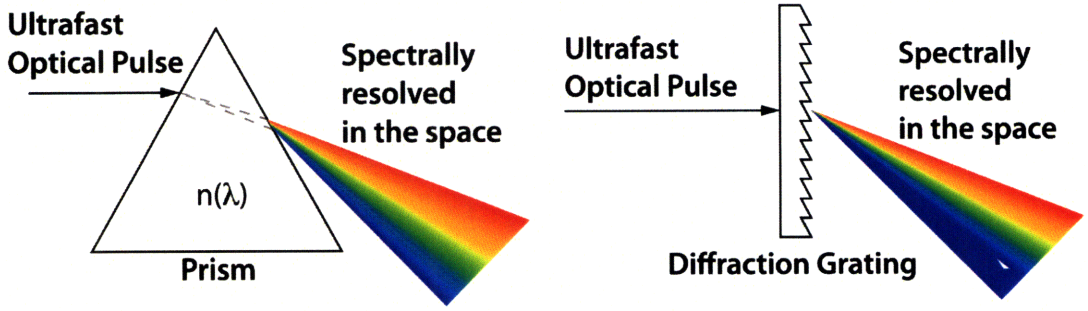

Figure 1.5 Dispersion in space.

1.2.1 Group Velocity Dispersion

In electromagnetic optics [12], optical pulse has a group velocity that is the speed for optical pulse envelope:

$$\frac{1}{v_g} = \left.\frac{dk}{d\omega}\right|_{\omega_0} = \frac{1}{c}\left(n(\omega_0) + \omega_0 \left.\frac{dn(\omega)}{d\omega}\right|_{\omega_0} \right) \tag{1.2.1}$$

where c is speed of light in a vacuum, n is refractive index, ω is optical angular frequency, ω_0 is optical angular frequency for center wavelength of the optical pulse, and k is wave vector. For each monochromatic wave in the optical pulse, phase velocity is also defined as:

$$v_p = \frac{\omega}{k} = \frac{c}{n(\omega)} \tag{1.2.2}$$

In non-dispersive medium, such as free space, $v_g = v_p = c/n$ since $n(\omega) = n = const$ over all optical angular frequencies of the optical pulse. When there is no dispersion, the optical pulse shape does not change. However, when the optical pulse propagates through dispersive medium,

group velocity is no longer the same as phase velocity and this results in dispersion related to group delay:

$$\tau_d = \left.\frac{dk}{d\omega}\right|_{\omega_0} \cdot z = \frac{z}{v_g} \tag{1.2.3}$$

Thus, time delay between two wavelengths can be calculated as:

$$\Delta\tau \simeq \frac{d\tau_d}{d\lambda} \cdot \Delta\lambda = \frac{d}{d\lambda}\left(\frac{z}{v_g}\right) \cdot \Delta\lambda = D(\lambda) \cdot z \cdot \Delta\lambda \tag{1.2.4}$$

where λ is wavelength in free space. $D(\lambda)$ is called group delay dispersion (GDD) or dispersion parameter, and it is also expressed as

$$D(\lambda) = \frac{d}{d\lambda}\left(\frac{1}{v_g}\right) = -\frac{2\pi c}{\lambda^2}\beta_2 = -\frac{\lambda}{c}\frac{d^2 n}{d\lambda^2} \tag{1.2.5}$$

where β_2 is GVD parameter. It is noted that the eq. (1.2.5) includes only second order term in the Taylor expansion of the refractive index, and the effects of higher order terms are not considered. Therefore, group velocity dispersion (GVD) is defined as the phenomenon where the optical pulse is broadened due to the wavelength dependence of the group velocity. GVD is critical in the application of ultrafast optical pulse since it causes significant pulse broadening whereas group velocity does not affect the pulse shape. The pulse broadening σ_τ can be obtained from eq. (1.2.4):

$$\sigma_\tau = |D(\lambda)| \cdot \sigma_\lambda \cdot L_D \tag{1.2.6}$$

where σ_λ is bandwidth of the optical pulse, and L_D is dispersion length or the distance where optical pulse propagates through the dispersive media. From eq. (1.2.6), it is clear that shorter pulse duration (or larger spectral width) or longer dispersion length generates more significant pulse broadening. The highly dispersive optical elements commonly used in microscopy are the objectives [13] and the optical fibers since they have relatively long dispersion length. It is very important to manage GVD with these elements, and GVD can be compensated or minimized with the pulse stretcher or pulse compressor, which is further discussed in chapter 2.

1.2.2 Angular Dispersion

The refraction- or diffraction-induced dispersions are often very useful in manipulating ultrafast optical pulses. Angular dispersion represents color-resolving power which shows how much dispersive angle is deviated depending on wavelength.

In the refractive optics, a triangular prism is a commonly used dispersive element. To use it in generating uniform angular dispersion over wavelength, incident angle on the prism ϕ_1 should be set at the Brewster's angle ($\tan\phi_1 = n(\lambda)$) to minimize reflection on the surface, and refractive angle at the prism ϕ_2 should be equal to ϕ_1 to minimize angle of deviation ε. (See figure 1.6(b)) Angular dispersion is expressed as a derivative of angle of deviation with respect to wavelength [14]:

$$\frac{d\varepsilon}{d\lambda} = \frac{b}{l_1}\frac{dn(\lambda)}{d\lambda} \tag{1.2.7}$$

Since $dn(\lambda)/d\lambda$ is not constant over broad wavelength range, angular dispersion is not constant. In addition, angular dispersion with dispersive prism is relatively small compared to one with diffraction grating. Therefore, dispersive prism is useful in applications where optical loss should be little or dispersion can be small, such as for compressing ultrafast optical pulse.

In diffractive optics, diffractive grating also generates dispersion. Diffractive grating is an array of equally spaced identical diffracting elements where the distance between elements (groove spacing or pitch) is comparable to the illumination light wavelength. Figure 1.6(c) shows the schematics of diffraction grating. Diffraction of light from different elements enables optical pulses to be color-resolved with different angles (β) at same incident angle (α). Angular dispersion at the diffractive grating is defined as below [14]:

$$\frac{d\beta}{d\lambda} = Gm\sec\beta \tag{1.2.8}$$

where $G = 1/d$ is groove frequency, and m is diffraction order (1^{st} order diffraction ($m = 1$) is used for most of applications.) From eq. (1.2.8), angular dispersion is constant over broad wavelength range since it is independent of wavelength, and it has large wavelength-resolving power due to large angular dispersion. One major drawback is lower efficiency for 1^{st} order

diffraction (~70-80%) compared with prism since some power is lost to the higher diffraction orders. In any case, diffractive gratings are routinely used in spectroscopic applications because of their large wavelength-resolving power despite their large optical loss. A pair of diffraction grating is sometimes used for dispersion compensation or optical pulse shaping.

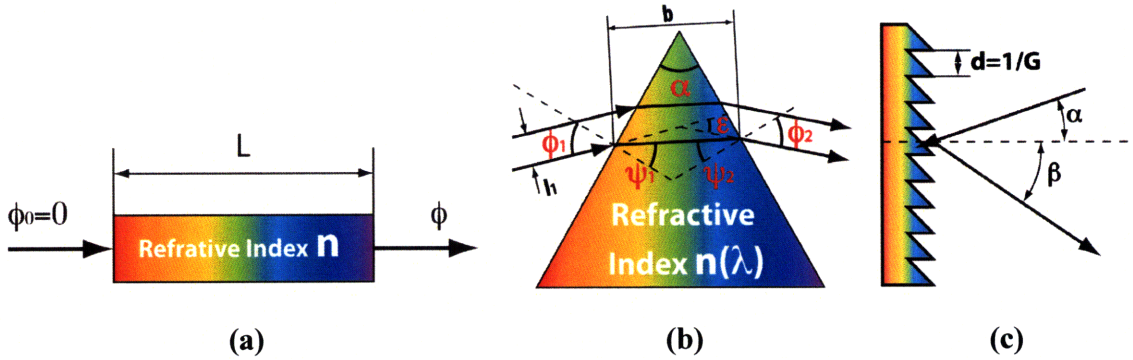

Figure 1.6. Schematic diagram of dispersion components: (a) dispersive medium (b) prism (c) reflective diffraction grating

1.3 Two-Photon Excitation Fluorescence Microscopy

One of the most popular imaging techniques that utilize ultrafast optical pulses in biology and medicine is TPM. It uses two-photon absorption process predicted by Dr. Göppert-Mayer in 1931 and was utilized by Dr. Webb's group in the form of the optical microscopy [1]. Conventional confocal microscopy places a pinhole at a location which is conjugated to the excitation focus in the detection light path. The conjugated pinhole rejects out-of-focus background from the specimen and enables optical sectioning. In contrast, TPM has intrinsic optical sectioning capability based on nonlinear excitation that is maximized at the focal spot. In following sections, two-photon absorption process and TPM are introduced.

1.3.1 Introduction to Fluorescence and Two-Photon Absorption Process

After photon absorption that induces an electronic state transition of an atom or a molecule, a lower energy photon is emitted when the atom or molecule returns to the ground electronic state after vibrational relaxation, which is called fluorescence. Absorption process occurs on the order of femtosecond coupling a singlet ground state to a singlet excited state. Once the electron is excited, relaxation to the lowest vibronic level in the excited electronic state occurs on the order

of picoseconds including internal conversion where energy is lost thermally. Finally, the electron returns to the ground state after staying in the excited electronic state for a period of time that is typically on the order of nanoseconds; this characteristic time of the fluorescence molecule is called fluorescence lifetime. Figure 1.7(a) represents a simplified Jablonski diagram for single photon fluorescence process. Some features of fluorescence not shown in the figure are Stokes shift and fluorescence quantum yield. Stokes shift is referred to when the emission wavelength is a little longer than that of absorption wavelength. Stokes shift originates from the fact that emission photons always have lower energy than absorption photons due to internal conversion processes. Some molecules in the excited state do not relax by generating fluorescence; non-radiative relaxation from excited state to ground state may occur where energy is lost by other mechanisms such as dynamic quenching or fluorescence energy transfer. Additionally, intersystem crossing to triplet state with delayed emission or phosphorescence occurs. Fluorescence quantum yield is defined as the ratio of the number of emission fluorescence to the number of photons absorbed (in the case of two-photon absorption, photon pairs absorbed). Photobleaching is another important characteristic of fluorescence molecules. A molecule may become optically inactive after repeated absorption–emission cycles. Photobleaching is often caused by the production of reactive oxygen molecules during fluorophore excitation and the subsequent chemical interaction between these reactive oxygen molecules and the fluorophore.

Fluorescence is typically generated through single photon absorption process, but it can also be produced via a two-photon absorption process with high intensity illumination. Figure 1.7 shows how two-photon absorption occurs compared with single photon absorption process. With two-photon absorption process, a pair of photons that arrives at a molecule within a time interval on the order of femtoseconds are absorbed by the molecule via transition through a virtual state, as shown in figure 1.7(b). Fluorescence emission by two-photon absorption process is the same as by single photon absorption process since fluorescence emission occurs from the lowest vibronic level of the excited state after internal conversion in both cases. To increase the probability of simultaneous absorption of two photons, it requires high peak power of ultrafast optical pulses and tight spatial focusing of these pulses; it is one of reasons why TPM has intrinsic optical sectioning capability.

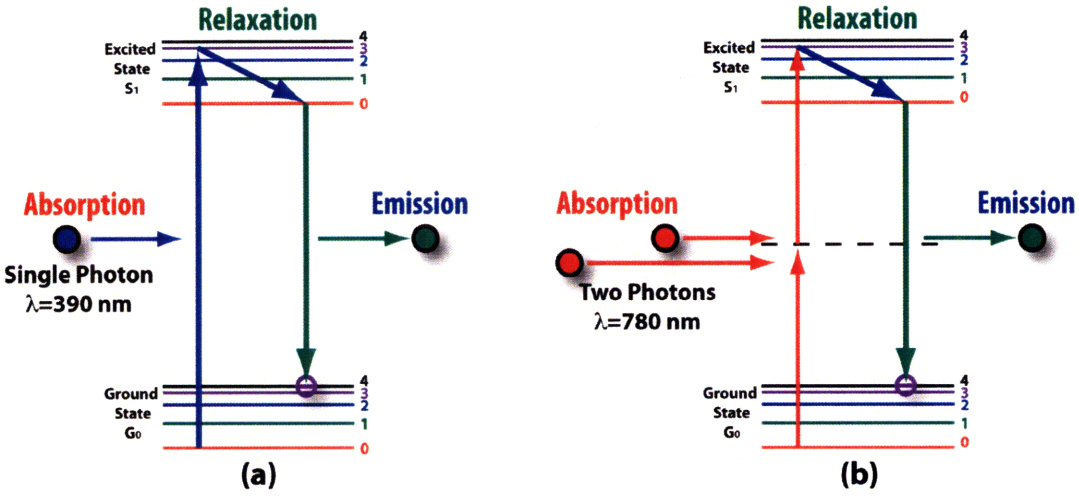

Figure 1.7 Conceptual diagram on how fluorescence works (a) one-photon absorption process and (b) two-photon absorption process

1.3.2 Quantitative Analysis of Two-Photon Absorption Process

In this section, the theory of two-photon absorption process is reviewed. From the viewpoint of quantum mechanics, single photon and multiphoton absorption processes can be derived from Schrödinger equation by incorporating perturbation theory [15, 16]. The probability of being excited to energy level n from the ground state g through a two-photon process is

$$p_n^{(2)}(t) = R_{ng}^{(2)} \cdot t \tag{1.3.1}$$

where $R_{ng}^{(2)}$ is transition rate of two-photon absorption (sec^{-1}). It is also expressed as

$$R_{ng}^{(2)}(t) = \bar{\sigma}_{ng}^{(2)} \cdot \bar{I}^2(t) \tag{1.3.2}$$

where $\bar{\sigma}_{ng}^{(2)} \approx \dfrac{\left|\mu_{nm}\mu_{mg}\right|^2}{4\varepsilon_0^2\hbar^2c^2\Gamma_n} = \delta$ is two-photon cross section for the molecule ($m^4sec/photon^2$), c is speed of light in a vacuum, μ_{nm} is interaction energy between level n and m, ε_0 is permittivity of free space, $\hbar$ is reduced Plank constant, Γ_n is the width of level n, and $\bar{I}(t)$ is intensity ($photon/m^2/sec$). For femtosecond lasers, optical pulse width (τ_p) is so short that a single molecule can absorb at most one photon pair for a single laser pulse since the molecule life time (τ_s) is much longer than optical pulse width ($\tau_s \gg \tau_p$). In this case, n_a, the number of photon pairs absorbed in single molecule during single optical pulse, is:

$$n_a = \left\langle p_n^{(2)}(t) \right\rangle = \left\langle R_{ng}^{(2)} \right\rangle \cdot (t_2 - t_1) = \delta f_p^{-1} \left\langle \bar{I}^2(t) \right\rangle \tag{1.3.3}$$

where $\langle \bullet \rangle$ is time average over the one period ($t_2 - t_1 = f_p^{-1}$). For laser scanning microscopy, the absorption probability is a function of the time-dependent lateral intensity profile in the focal spot $I(r,t)$ (assuming Gaussian beam profile):

$$P(t) = \iint I(r,t) \cdot dA = I(t) \int_0^{+\infty} \exp\left(-\frac{2r^2}{\omega_0^2} \right) \cdot 2\pi r \, dr = I(t) \frac{\pi \omega_0^2}{2} = I(t) \frac{\lambda^2}{2\pi NA^2}$$

$$\text{and } \bar{I}(t) = \frac{I(t)}{hc/\lambda} = \frac{NA^2}{\hbar c \lambda} P(t) \tag{1.3.4}$$

where $P(t)$ is the instantaneous laser power, $\omega_0 = \frac{1}{\pi} \cdot \frac{\lambda}{NA}$ is the beam waist , and $NA = n \sin\theta$ is NA of the objective. This approach provides similar results if Fraunhofer diffraction intensity profile is assumed instead of Gaussian beam. Therefore, eq. (1.3.3) can be rewritten:

$$n_a = \delta f_p^{-1} \left(\frac{NA^2}{\hbar c \lambda} \right)^2 \left\langle P^2(t) \right\rangle = \delta f_p^{-1} \left(\frac{NA^2}{\hbar c \lambda} \right)^2 \xi P_0^2 \tag{1.3.5}$$

$$\text{where } \xi = \frac{\left\langle P(t)^2 \right\rangle}{\left\langle P(t) \right\rangle^2} = \frac{(t_2 - t_1) \int_{t_1}^{t_2} P^2(t) dt}{\left(\int_{t_1}^{t_2} P(t) dt \right)^2}.$$

For the Gaussian pulse temporal profile, $\xi = \sqrt{\frac{2 \ln 2}{\pi}} \cdot \frac{1}{f_p \tau_p}$. From eq. (1.3.5), it is seen that n_a is proportional to average intensity square. Significant deviation from this proportional relationship may result as n_a becomes larger because of fluorophore ground-state depletion, a process called fluorescence saturation [17]. This process leads to excitation saturation where excitation intensity profile broadens when n_a exceeds certain threshold level ($n_a = 0.1$ as a rule of thumb) [18].

1.3.3 Introduction to Two-Photon Excitation Fluorescence Microscopy

In this section, the instrumentation design of TPM is introduced. Since nonlinear process such as two-photon absorption requires high intensity, pulsed laser on the order of femtosecond or picosecond should be focused on the sample. Once the fluorescence is emitted, its intensity or optical spectrum at the focal volume can be measured by a photodetector. Since excitation occurs

at a single focus, raster scanning of the laser in two-dimensional (2D) plane is required to produce an image and the focal plane must be translated to obtain a three-dimensional (3D) map of the specimen.

Figure 1.8 shows a typical TPM system. Either femtosecond or picosecond pulsed laser may be used as a light source. A two-axis laser scanner deflects the collimated laser beam laterally from the optical axis as shown in the diagram. Through the relay lenses (the scan lens and the tube lens) that act as a beam expander, the back aperture of the objective is filled with the collimated laser beam. Subsequently, the objective focuses the excitation light at diffraction limit to induce localized two-photon excitation (TPE). Axial scan can be accomplished by either physically translating the objective or the specimen. Fluorescence is emitted omnidirectionally and approximately 30% of the fluorescence can be collected by the high numerical aperture (NA) objective. At the dichroic mirror, fluorescence is transmitted to the collection lens and filter sets. The fluorescence signal is measured by a photodetector such as a photomultiplier tube (PMT), an image sensor such as a charge-coupled device (CCD), or a complementary metal oxide semiconductor (CMOS) sensor. Fluorescence intensity measurement is transferred to the computer where the image is digitally constructed.

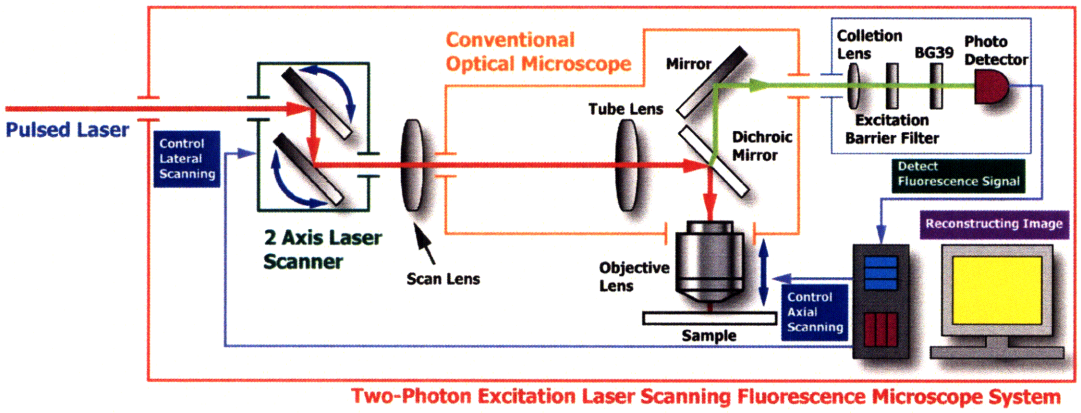

Figure 1.8 Schematic diagram of conventional two-photon laser scanning microscopy

TPM has several advantages in 3D depth-resolved image acquisition. First, the probability of TPE has a quadratic dependence on photon flux. The high photon flux at the focal volume results in depth discrimination where over 80% of fluorescent signal is localized to within a 1 μm thick region centered at the focal plane. Second, during the imaging of the fixed cell, reducing the

chromophore photobleaching is critical, and localized excitation minimizes the photobleaching outside the focal plane. Similarly, in live cell imaging, photodamage affects cellular viability and may be minimized by the excitation localization. Third, in the case of single photon process, excitation spectrum and emission spectrum of the chromophore are partially overlapped, and it is difficult to reject background due to the leakage of excitation light. In TPM, excitation spectrum is located far from the emission spectrum in the visible region. Therefore, fluorescence signal is easily separated from the excitation light resulting in higher signal-to-noise-ratio (SNR). Fourth, TPM excitation wavelength lies in the infrared region resulting in significantly lower tissue scattering and absorption and deeper imaging. Finally, both confocal microscopy and TPM has 3D resolution, but there is major difference in terms of the underlying principle of depth discrimination. Confocal microscope rejects unwanted out-of-focus fluorescence with a conjugated emission pinhole. TPM inherently produces fluorescence signal only at focal volume through the nonlinear two-photon absorption process. Therefore, TPM utilizes excitation manipulation to achieve 3D resolution while confocal microscopy exploits emission manipulation. Eliminating the need for the detection pinhole is critical for the imaging of turbid tissues. The emission photons scattered by the tissue are blocked by the detection pinhole, but they can be collected in the TPM case.

Although two-photon microscopy is a powerful tool for 3D volumetric imaging, one of the major drawbacks is its relatively slow imaging speed limited by the sequential nature of scanning and the bandwidth of the scanning subsystem. Image acquisition in two-photon scanning microscopy takes much longer than conventional wide-field illumination microscopy. To reduce image acquisition time, either pixel resolution needs to be reduced or pixel dwell time needs to be shortened. However, lower pixel resolution generates much coarser image and fine image features may be lost. As the dwell time at a location shortens, the number of detected photons decreases, and SNR is deteriorated. Since the concentration of fluorophores and the lifetime of these probes are dictated by the relevant biological system, the maximum SNR is fundamentally determined by the pixel dwell time. Several techniques to improve imaging speed while maintaining the SNR have been proposed. Depth resolved wide-field illumination based on temporal focusing is one of these techniques and will be discussed later in detail.

1.4 Temporal Focusing

Conventional fluorescence microscopy illuminates sample using wide-field geometry resulting in 2D images without depth resolution. In 3D optical microscopy such as confocal and two-photon excitation microscopy, excitation light is focused to a diffraction-limited spot that results in optical sectioning but requires sequential raster scanning of the excitation volume to produce a 3D image. A consequence of raster scanning is that image acquisition time becomes slower as sample size or resolution increases. As mentioned in the previous section, finite fluorophore concentration and fluorescence saturation ultimately limits fluorescence photon generation rate even when a very fast scanning mechanisms, such as acousto-optical deflectors, may be used. Therefore, the most effective way to improve imaging speed is to parallelize the excitation process. The most successful approach utilizing this concept is the multifocal multiphoton microscopy (MMM) [19-22]. Temporal focusing is another interesting idea which was recently proposed to produce depth-resolved wide-field illumination (DRWFI) [23, 24].

Temporal focusing is applicable to nonlinear microscopic imaging where ultrafast optical pulses with relatively broad spectral band are used. Figure 1.9 demonstrates the underlying concepts behind spatial focusing and temporal focusing. In figure 1.9(a), optical pulse is focused laterally, traveling along axial direction. Note that its temporal pulse width is kept constant. The intensity at the focal spot reaches a maximum. Nonlinear optical process such as two-photon absorption is proportional to the power of the intensity resulting in optical sectioning. For high NA objective, submicron lateral and axial resolution can be achieved. With temporal focusing, the optical pulse travels in axial direction without changing the beam diameter unlike spatial focusing (See figure 1.9(b)). However, the instantaneous intensity will be maximized at the focal plane if the temporal width of the optical pulse can be manipulated spatially such that it is minimized at focal plane. This approach allows wide-field imaging with depth discrimination. The implementation of temporal focusing will be discussed in detail in chapter 3. One drawback in using temporal focusing is that it requires high illumination power. Two-photon absorption process depends on quadratic excitation intensity. Since excitation intensity is inverse proportional to the illumination area, excitation power must increase as illumination area becomes large in order to maintain the same SNR. However, the power of typical Ti:Sapphire

laser produces femtosecond pulses with average limited to several watts. Simple calculation similar to eq. (1.3.5) shows that efficient excitation ($n_a \sim 0.1$) of most organic dyes cannot be achieved for imaging area larger than 20 μm by 20 μm. One option to alleviate this power problem is to use optical parametric amplifier (OPA) or regenerative amplifier that has much higher peak power with similar average power but much lower repetition rate on the order of 1 kHz. Another option is to use fluorophores with much higher two-photon cross section such as quantum dot (QD). With QD, large fluorescence signal can be obtained despite low illumination intensity on the sample.

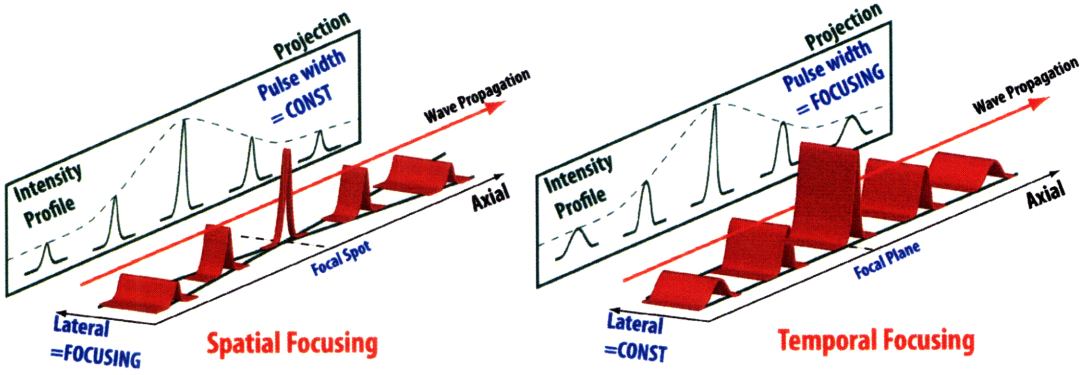

(a) **(b)**

Figure 1.9 Pictorial description of (a) spatial focusing and (b) temporal focusing

1.5 The Motivation and the Scope of This Thesis

In this thesis, we explore several interesting methods to manipulate ultrafast optical pulse for microscopic imaging and fabrication. This thesis covers two aspects of ultrafast optical pulse manipulation: dispersion management in optical fibers and temporal focusing depth-resolved wide-field imaging and fabrication.

Ultrafast optical pulse delivery via optical fiber is very important in microscopic imaging in terms of portability. In conventional laboratory microscopes, portability is less critical. However, portability becomes a prime consideration for clinical applications. Clinical usage is limited if the microscope itself is not in a handheld format. One of key applications is the development of TPE endoscopies for 3D optical biopsy. Histological analysis is now the clinical standard to

assess the pathological states of a tissue, but it requires the tissue to be excised, fixed, sectioned, stained, and examined under optical microscope. The invasive nature of histopathology limits the number of suspicious sites to be examined, and supplementary microscopic imaging modality may be useful to select better biopsy sites to enhance the chance of disease detection. Handheld MMM may be used for diagnosis of skin cancer. While excisional biopsy provides the diagnostic accuracy for skin lesions, there are cases that excisional biopsy should be minimized such as when lesion occurs in the facial area and two-photon microscopic diagnosis may be utilized. This approach may also be used during surgical removal of lesions. A more thorough examination of surgical margin may avoid missing very small malignant tissue (true negative) while sparing healthy tissues. This approach can minimize follow-up surgery, reduce surgical trauma, and improve post-surgery recovery rate. Another important application is TPE microendoscopy. Endoscopy is very popular imaging modality in diagnosing diseases that occur inside body cavities. Conventional optical endoscopy provides low-resolution images of only tissue surface. Medically approved endoscopic ultrasound (EUS) can image down to submucosa layer, but has very limited resolution. Optical coherence tomography (OCT) [25], one of the most promising methods, provides 3D imaging into millimeter thick tissue structures. Unfortunately, its spatial resolution is still too coarse to produce subcellular details. Reflected confocal microscopy [26] is an excellent method to obtain tissue morphological information, but offers little biochemical specific signals. On the other hand, TPE microendoscopy incorporated into conventional microscopy will provide submicron optical resolution high enough to resolve subcellular structures required for definitive pathological analysis. TPE microendoscopy also provides fluorescence based contrast and complements other endomicroscopic approaches such as confocal and OCT. Consequently, developing portable multiphoton handheld probes or microendoscopes are important for biomedical diagnosis and will require understanding ultrafast optical pulse delivery by optical fibers.

While there are high speed two-photon imaging techniques such as MMM, there remains a need for depth-resolved high-throughput imaging without lateral scanning that significantly simplifies instrument design and lowers cost. The temporal focusing approach based on the inherent broad spectral bandwidth of ultrafast pulses should be further explored since it enables DRWFI [23, 24]. Temporal focusing based TPM may allow efficient imaging of biological

systems labeled with super high two-photon cross section fluorophores such as QDs. The capability of this technique to improve the two-photon microfabrication efficiency also opens up many potential applications areas in biomedicine and beyond.

The organization of this thesis is as follows. The delivery of ultrafast pulses by different commercial fibers is evaluated in terms of optical pulse shape and TPM performance: fiber coupling efficiency, spectral bandwidth and temporal pulse width of the optical pulse, two-photon excitation efficiency, and optical resolution. Minimizing dispersion effect of pulses propagating through these fibers using a pulse compressor is also evaluated (Chapter 2). The spectral bandwidth of ultrafast optical pulses is exploited for DRWFI based on temporal focusing. A mathematical model based on diffraction theory is derived to evaluate its performance in terms of depth-resolving capability as a function of instrument design parameters. With optimized design parameters, a TPE DRWFI microscope is implemented. The axial optical resolution of this microscope is assessed, and its sensitivity and imaging speed are evaluated using QDs with high two-photon cross sections (Chapter 3). Two DRWFI applications are examined. Live cell labeled with QDs are imaged using TPE DRWFI microscope (Chapter 4). 3D lithographic microfabrication based on photobleaching process (Chapter 5) are demonstrated. Lastly, this thesis is concluded with an outlook of future DRWFI applications (Chapter 6).

References

1. W. Denk, J. H. Strickler, and W. W. Webb, "2-Photon Laser Scanning Fluorescence Microscopy," Science **248**, 73-76 (1990).
2. P. A. Franken, A. E. Hill, C. W. Peters, and G. Weinreich, "Generation of Optical Harmonics," Physical Review Letters **7**, 118 (1961).
3. P. D. Maker, and R. W. Terhune, "Study of Optical Effects Due to an Induced Polarization Third Order in the Electric Field Strength," Physical Review **137**, A801 (1965).
4. I. Pastirk, J. M. Dela Cruz, K. A. Walowicz, V. V. Lozovoy, and M. Dantus, "Selective two-photon microscopy with shaped femtosecond pulses," Optics Express **11**, 1695-1701 (2003).
5. J. P. Ogilvie, D. Debarre, X. Solinas, J. L. Martin, E. Beaurepaire, and M. Joffre, "Use of coherent control for selective two-photon fluorescence microscopy in live organisms," Optics Express **14**, 759-766 (2006).
6. D. Meshulach, and Y. Silberberg, "Coherent quantum control of two-photon transitions by a femtosecond laser pulse," Nature **396**, 239-242 (1998).

7. H. Kawano, Y. Nabekawa, A. Suda, Y. Oishi, H. Mizuno, A. Miyawaki, and K. Midorikawa, "Attenuation of photobleaching in two-photon excitation fluorescence from green fluorescent protein with shaped excitation pulses," Biochemical and Biophysical Research Communications **311**, 592-596 (2003).
8. W. Kaiser, and C. G. B. Garrett, "Two-Photon Excitation in CaF2: Eu2+," Physical Review Letters **7**, 229 (1961).
9. W. L. Peticolas, J. P. Goldsborough, and K. E. Rieckhoff, "Double Photon Excitation in Organic Crystals," Physical Review Letters **10**, 43 (1963).
10. F. W. Wise, I. A. Walmsley, and C. L. Tang, "Simultaneous Formation of Solitons and Dispersive Waves in a Femtosecond Ring Dye-Laser," Optics Letters **13**, 129-131 (1988).
11. A. M. Weiner, "Femtosecond pulse shaping using spatial light modulators," Review of Scientific Instruments **71**, 1929-1960 (2000).
12. B. E. A. Saleh, and M. C. Teich, *Fundamentals of photonics* (Wiley-Interscience, Hoboken, N.J., 2007).
13. J. B. Guild, C. Xu, and W. W. Webb, "Measurement of group delay dispersion of high numerical aperture objective lenses using two-photon excited fluorescence," Applied Optics **36**, 397-401 (1997).
14. M. Born, E. Wolf, and A. B. Bhatia, *Principles of optics : electromagnetic theory of propagation, interference and diffraction of light* (Cambridge University Press, Cambridge [England] ; New York, 1999).
15. R. W. Boyd, *Nonlinear optics* (Academic Press, Amsterdam ; Boston, 2008).
16. B. R. Masters, and P. T. C. So, *Handbook of biomedical nonlinear optical microscopy* (Oxford University Press, New York, 2008).
17. C. Xu, and W. Webb, "Multiphoton Excitation of Molecular Fluorophores and Nonlinear Laser Microscopy," in *Topics in Fluorescence Spectroscopy*(2002), pp. 471-540.
18. K. Berland, and G. Q. Shen, "Excitation saturation in two-photon fluorescence correlation spectroscopy," Applied Optics **42**, 5566-5576 (2003).
19. J. Bewersdorf, R. Pick, and S. W. Hell, "Multifocal multiphoton microscopy," Optics Letters **23**, 655-657 (1998).
20. A. H. Buist, M. Muller, J. Squier, and G. J. Brakenhoff, "Real time two-photon absorption microscopy using multi point excitation," Journal of Microscopy-Oxford **192**, 217-226 (1998).
21. L. Sacconi, E. Froner, R. Antolini, M. R. Taghizadeh, A. Choudhury, and F. S. Pavone, "Multiphoton multifocal microscopy exploiting a diffractive optical element," Optics Letters **28**, 1918-1920 (2003).
22. T. Nielsen, M. Frick, D. Hellweg, and P. Andresen, "High efficiency beam splitter for multifocal multiphoton microscopy," Journal of Microscopy-Oxford **201**, 368-376 (2001).
23. D. Oron, E. Tal, and Y. Silberberg, "Scanningless depth-resolved microscopy," Optics Express **13**, 1468-1476 (2005).
24. G. H. Zhu, J. van Howe, M. Durst, W. Zipfel, and C. Xu, "Simultaneous spatial and temporal focusing of femtosecond pulses," Optics Express **13**, 2153-2159 (2005).
25. D. Huang, E. A. Swanson, C. P. Lin, J. S. Schuman, W. G. Stinson, W. Chang, M. R. Hee, T. Flotte, K. Gregory, C. A. Puliafito, and J. G. Fujimoto, "Optical Coherence Tomography," Science **254**, 1178-1181 (1991).
26. B. R. Masters, "Reflected light confocal microscopy of human skin in vivo," Scanning **21**, 133-134 (1999).

Chapter 2

Ultrafast Optical Pulse Delivery with Fibers in Nonlinear Microscopy

2.1 Introduction

Nonlinear microscopy can provide intrinsic 3D resolution, allow deep imaging into tissues, achieve submicron optical resolution, and minimize photodamage and photobleaching [1, 2]. The term nonlinear microscopy now encompasses a broad class of techniques such as multiphoton-excited fluorescence imaging, multiple-harmonic generation imaging, and coherent anti-Stokes Raman imaging [3-5]. While nonlinear microscopy has found applications in numerous biological studies, many in-vivo applications will require adapting this technology into an endoscopic format that involves delivering femtosecond optical pulses through optical fibers. Conduction of light via traditional optical fibers is based on total internal reflection (TIR) and limited by optical loss and dispersion. Optical loss has been dramatically reduced by minimizing impurities during manufacturing process. Dispersion management has focused on chromatic dispersion reduction to optimize long haul optical communication. However, the requirements for optical pulse delivery with fiber optics in nonlinear microscopy are quite different from those for optical communication. First, these two applications operate in different spectral windows. The optical window for nonlinear microscopy is determined by the absorption spectra of typical endogenous and exogenous fluorophores, the wavelength-dependent attenuation coefficients of tissues, and the operating wavelengths of available high-power pulsed lasers. The optical window for optical communication is determined mostly by identifying the spectral range where attenuation due to Rayleigh scattering and chromatic dispersion in fibers are minimized [6]. Given the constraints in the optical window for nonlinear microscopy, chromatic dispersion often cannot be minimized and results in low performance in fiber optic-based nonlinear microscopy. Far from the zero dispersion band, GVD, which characterizes the wavelength dependence of the

group velocity in a medium, becomes dominant. This effect is especially pronounced for femtosecond optical pulses, since a wide spectral bandwidth is needed to produce these ultrafast optical pulses (time-bandwidth limit). Linear prechirping [7, 8] is often needed to compensate for the GVD introduced by the fiber [9, 10]. Second, nonlinear microscopy requires ultrafast optical pulses of substantially higher energy than that required in telecommunication. As optical power through a fiber increases, nonlinear effects become more prominent. These nonlinear effects include SPM that enlarges spectral bandwidth and broadens temporal pulse width [11]. The optical pulse distortion which results from fiber delivery often cannot be fully compensated for these nonlinear effects by simple linear prechirping approach, and the pulse width often increases with input power [9]. Therefore, the effects on high power ultrafast optical pulse delivery require careful investigation for nonlinear microscopy applications.

The recently introduced photonic crystal fibers (PCFs) [12-14] have a number of superior optical characteristics for conducting ultrafast optical pulses than conventional optical fibers in terms of guiding, dispersion and refraction [15]. PCF is a waveguide constructed with photonic crystal, which is dielectric or metallic material with the periodic structure of the refractive index. This material has photonic band gap (PBG), the range of optical frequencies where the light cannot propagate through. The band gap location depends on fiber microstructure and can be made independent of propagation direction and polarization of light. One common example of one-dimensional (1D) photonic crystal is the Bragg mirror [16] which contains a periodic pile of alternating dielectric films along optical axis. Light travels along optical axis with consecutive reflection and transmission at the face of each film, and wave is fully reflected at a given wavelength range for appropriate film thickness. Extension to 2D or 3D PBG effect has been partially successful recently. If a defect is inserted in infinitely periodic microstructure, the defect supports some modes inside the band gap, which is localized in the outskirts of the defect [15, 17]. Line defects create a waveguide, whereas point defects generate a resonant cavity. Therefore, 2D PBG effect with line defect makes PCF a useful waveguide. There are various kinds of PCFs depending on both of core and cladding structures. Figure 2.1 represents the general description of light delivery via several types of PCFs. A popular PCF is a solid core PCF [18, 19] which has a solid core with a microstructured cladding (Figure 2.1(a)). It is sometimes called index-guiding or high-index core fiber. Its cladding consists of silica-air

photonic crystal material. Even though it is made of photonic crystal, PBG effect does not actually occur during the light propagation. Depending on its structure, effective refractive index in the cladding can be controlled: it should always be smaller than refractive index of the core, although the silica refractive indices for both core and cladding are the same. Therefore, light is confined in the fiber core by a mechanism analogous to TIR, which is called modified total internal reflection (MTIR). These PCFs enable single mode delivery over the broadband wavelength regardless of core size [18-20], and even for unusually large mode area [21]. Other applications of these PCFs are optical soliton formation [22], supercontinuum generation [23], and dispersion management [24]. Another form of PCF is the hollow core PCF, or low-index core fiber [14]. Its core is hollow instead of solid, and its cladding is made of microstructured photonic crystal (Figure 2.1(b)). Light is confined to the hollow core by the PBG effect in the microstructured cladding, even if the refractive index in the core is lower than that of the cladding. Its applications are divided into different classes: removing constraints due to the optical properties of the core material and reinforcing interactions between light and gas-filling the fiber core. Some of its applications are high optical power delivery with lower nonlinearity, megawatt optical soliton generation with xenon-filled core [25], and stimulated Raman scattering in hydrogen-filled core [26]. Bragg fiber, the third type of PCF, uses the Bragg mirror as cladding in the fiber (Figure 2.1(c)). The cladding is made with a concentric periodic distribution of alternating materials, and surrounds a hollow or a solid core. It is feasible to deliver light since it is discovered that Bragg mirror has omnidirectional reflection that occurs based on the PBG effect [27, 28]. One of its applications is improving light transmission over certain frequency ranges [29].

One of the challenges in PCF research is inventing the PCF fabrication process. Microstructured PCFs can be manufactured by drawing a silica-air hole preform acquired by stacking silica capillaries, drilling holes, or extrusion [30, 31]. Bragg fiber is made via the cigar-rolling technique. Multilayer mirror is rolled up to make a preform with hollow core, and then drawn [29]. PCFs are mostly made of silica and air to form silica-air holes, but it can also be formed with polymer instead of silica [32].

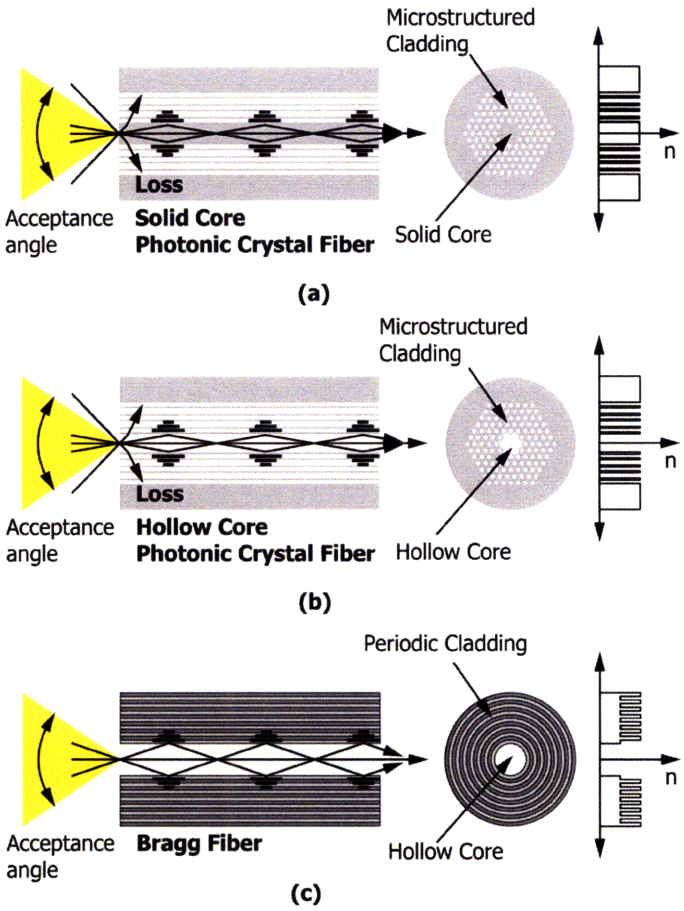

Figure 2.1 Photonic crystal fibers: (a) solid core photonic crystal fiber (b) hollow core photonic crystal fiber (c) Bragg fiber

Several researchers have studied the performance of delivering ultrafast optical pulses with optical fibers. Step-index single-mode fiber delivery has been well characterized [9, 33], but the performances with step-index multimode fiber were only partially described [34]. The use of pulse compressor to compensate for chromatic dispersion of these step-index single-mode fibers has also been studied [9]. Some types of PCFs such as hollow-core PCF [35, 36], TIR-based PCF [37], and double-clad PCF [10, 38], were studied in terms pulse spectral and temporal profiles. Most prior studies have demonstrated only the feasibility for TPE, but the efficiency to induce nonlinear effects by light pulses after fiber delivery has not been quantitatively compared with that of free space delivery. Furthermore, the effects of fiber delivery on optical resolutions in the nonlinear microscopy have not yet been evaluated. Importantly, PCFs also offer better

performance than traditional fibers in conducting high power ultrafast optical pulses since it has better optical characteristics in terms of guidance, dispersion [35-37, 39], and refraction [15]. Though promising, the effects of ultrafast pulse delivery using PCFs on the performance of nonlinear microscopes need further quantification.

In this chapter, we systematically characterize the performance of a nonlinear microscopy, i.e. two-photon microscopic imaging, using a variety of optical fibers for excitation light delivery. The performance is evaluated based on the parameters that include spectral bandwidth, temporal pulse width, TPE efficiency, and microscope optical resolution. Additionally, the effect of optical pulse compensation is evaluated based on optical pulse profile and TPE efficiency.

2.2 Instrumentation

Figure 2.2 shows the experimental apparatus used to characterize the performance of a nonlinear microscope when ultrafast optical pulses are conducted through a variety of optical fibers. The pulses were generated by a Ti:Sapphire femtosecond laser (Tsunami, Spectra-Physics, Mountain View, CA) which was pumped by a continuous-wave (CW) diode-pumped solid-state (DPSS) laser (Millennia V, Spectra-Physics, Mountain View, CA). It is tunable over a broad range in the near-infrared (NIR) wavelength range, producing pulse widths as short as 50 fs with pulse repetition rate of 80 MHz. In our experiment design, we chose 100 fs ultrafast optical pulse with a center wavelength of 780 nm. The pulse width is short enough to achieve efficient TPE. This wavelength is suitable for exciting many endogenous and exogenous fluorophores in biological specimens. A ruled grating-based optical pulse compressor [7] was installed for prechirping to compensate for chromatic dispersion in some measurements. The properties of the ultrafast optical pulses were examined by an optical autocorrelator and a spectrum analyzer in the temporal and the spectral domain respectively. The collimated light after fiber delivery was steered into a TPE fluorescence microscope based on an inverted platform (Axiovert S100TV, Carl Zeiss MicroImaging Inc., Thornwood, NY). A galvanometric laser scanning system (6350, Cambridge Technology, Cambridge, MA) was employed for lateral raster scanning and a piezoelectric objective positioner (P-721.00, Physik Instrumente L.P., Auburn, MA) was installed for axial scanning. These experiments were performed using a high NA objective lens

(Fluar, 40X / 1.30 Oil Immersion, Carl Zeiss MicroImaging Inc., Thornwood, NY) for high-resolution imaging. A PMT (R7400P, Hamamatsu Photonics K. K., Hamamatsu, Japan) was used in single photon counting mode for light detection.

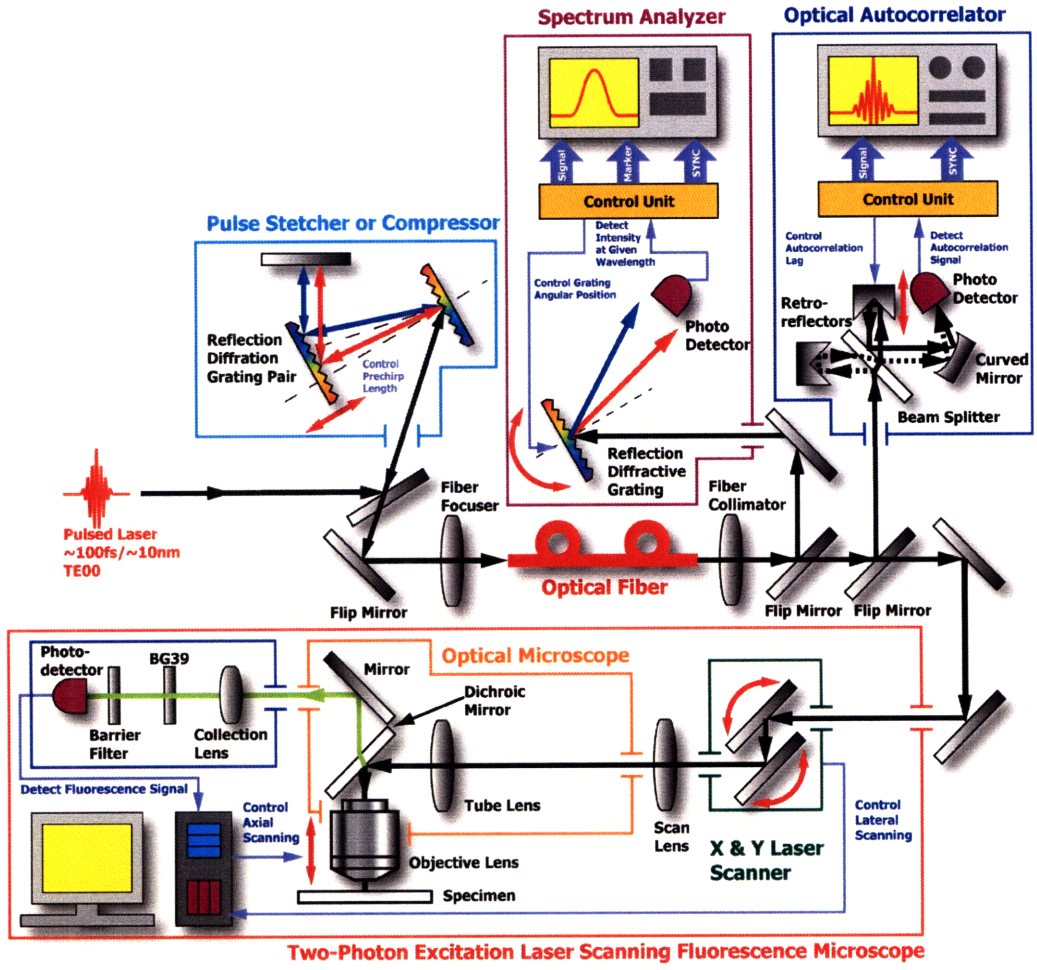

Figure 2.2 Experimental design for measuring ultrafast optical pulse characteristics through optical fibers and resulting TPE fluorescence microscopy performance. The experimental apparatus consists of a pulse compressor, an optical fiber coupling system including a fiber focuser and a fiber collimator, and a TPE laser scanning fluorescence microscope. The pulse compressor provides linear prechirping to compensate for chromatic dispersion in the system. The optical pulse profile can be measured with an optical autocorrelator and a spectrum analyzer. The delivered optical pulses enter into a TPE laser scanning fluorescence microscope where the TPE efficiency and the optical resolution are measured.

2.2.1 Optical Fibers

TIR-based fibers are categorized into step-index fibers, in which the refractive index at the core-cladding boundary changes abruptly, and graded-index fibers, in which the refractive index in the core changes gradually as it approaches to the refractive index of the cladding. They can also be classified into single-mode fibers or multimode fibers, depending on how many transverse modes they propagate. PCF includes MTIR-based fiber and PBG-based fiber as described in the previous section. Among these fibers, six common commercially available optical fibers were selected in this experiment as listed in Table 2.1. For step-index fibers, three fibers with different core size and number of propagating modes were used: a single-mode fiber (SISMF5um), a slightly large-core fiber (SIMMF10um), and a multimode fiber (SIMMF50um). This wide selection allows the effects of different core size and number of propagating modes to be evaluated. Graded-index fiber (GIMMF50um) was also used to compare the effects of graded-index versus step-index. For PCF, we chose two fibers: a hollow-core photonic crystal fiber (HCPCF6um) and a double-clad photonic crystal fiber (DCPCF16um). HCPCF6um employs PBG, whereas DCPCF16um uses MTIR which enables only single-mode light delivery even though its core is large enough to carry multiple modes. In each case, fiber length was two meters, which is a reasonable length for most biomedical applications. All fibers except for PCFs had FC/APC connectors on both ends to avoid back-reflection to light source. No connectors were used with PCFs because the air-silica hole structure used in constructing photonic crystal may be contaminated during the polishing process needed in connectorizing the fiber.

Fiber type (Manufacturer's part number)	Core (μm)	Cladding (μm)	Fiber NA	Manufacturer	Notation
Hollow-core photonic crystal fiber (AIR-6-800)	6	125	0.17	Crystal Fibre A/S, Birkerød, Denmark	HCPCF6um
Double-clad photonic crystal fiber (DC-165-16-Passive)	16	*165 /350	0.04		DCPCF16um
Step-index single-mode fiber (SMJ-3AF3AF-780-5/125-3-2)	5	125	0.14	OZ optics, Ontario, Canada	SISMF5um
Step-index multimode fiber (QMMJ-3AF3AF-UVVIS-10/125-3-2)	10	125	0.10		SIMMF10um
Step-index multimode fiber (QMMJ-3AF3AF-IRVIS-50/125-3-2)	50	125	0.22		SIMMF50um
Graded-index multimode fiber (MMJ-3AF3AF-IRVIS-50/125-3-2)	50	125	0.22		GIMMF50um

* inner cladding/outer cladding

Table 2.1 List of optical fibers used in the fiber characterization

2.2.2 Measurements

We first measured the coupling efficiency, defined here as the ratio of the optical power after fiber output to the optical power before fiber input. It was obtained by measuring average optical power both before and after fiber delivery with a thermopile power meter (LaserMate with LD10 sensor, Coherent Inc., Santa Clara, CA). We further measured FWHM of the temporal and spectral profile of the optical pulse after fiber delivery and compared these parameters with free space propagation. Two different approaches are commonly used to measure the pulse temporal profile: optical autocorrelation [40] and frequency-resolved optical gating (FROG) [41]. FROG measurement provides more detailed information, however, commercially available FROG is designed to measure pulses width in the range of 50 to 200 fs and the optical pulses broadened by some fibers can be as wide as several picoseconds. Thus, an interferometric optical autocorrelator (Autocorrelator MINI, APE GmbH, Berlin, Germany) was chosen in this experiment as it has very high SNR and is capable of measuring autocorrelation up to 15 ps. In this thesis, we define temporal pulse width of the optical pulse as FWHM of autocorrelation function. We also measured power spectrum of these pulses to provide complementary

information since the highly chirped optical pulse shape cannot be adequately characterized by optical autocorrelation alone. Using a laser spectrum analyzer (E201LSA03A, Imaging System Group, Horseheads, NY), we measured the spectral bandwidth of the optical pulse, which is defined as the FWHM of optical power spectrum. Using the TPE fluorescence microscope, we further measured TPE efficiency and optical resolution. TPE efficiency is described as ratio of the number of the fluorescence photons detected from a specimen as a function of optical power delivered by the microscope objective. A 232 μM aqueous fluorescein (fluorescein-5-isothiocyanate, Invitrogen, Carlsbad, CA) solution was used as a standard specimen in all these measurements. For optical resolution measurement, the point spread function (PSF) of 0.1 μm diameter carboxylate-modified yellow-green (505/515) fluorescent beads (F8803, Invitrogen, Carlsbad, CA) mixed with 2% w/v agarose gel (2120, EMD Chemical Inc., Gibbstown, NJ) were imaged in 3D. The resolution is quantified by the FWHMs of the PSF along lateral and axial directions.

2.3 Characteristics of Ultrafast Optical Pulse through the Fibers

2.3.1 Fiber Coupling Efficiency

Figure 2.3 presents maximally achieved coupling efficiency for each fiber with respect to fiber output optical power. First, the coupling efficiency is mostly independent of the fiber output optical power. All the fibers with smaller core have 40-50% coupling efficiency, and the others have 80-90% except for DCPCF16um. With DCPCF16um, the coupling efficiency is similar to smaller core fibers due to low numerical aperture (NA) of the fiber core.

Coupling efficiency is associated with the optical loss. Optical loss generally includes all losses through a fiber such as coupling loss and optical power attenuation which is negligible in two-meter fiber length. Furthermore, collimating the light after the fiber entails little loss, whereas optical loss occurs primarily during the coupling of light into the fiber. The spot diameter of focused rays on the surface of fiber core can be calculated, assuming a diffraction-limited spot size. If we assume that the lens aperture is circular, the rays have uniform intensity

and the NA of the lens (NA_{lens}) is smaller than the NA of the fiber (NA_{core}), the theoretical coupling efficiency $\varepsilon_{coupling}$ can be simplified as follows.

$$\varepsilon_{coupling} \approx \begin{cases} \left(\frac{d_{core}}{d_{FWHM}}\right)^2 = \left(\frac{d_{core} NA_{lens}}{0.5145\lambda}\right)^2 & if\ d_{FWHM} > d_{core} \\ 1 & Otherwise \end{cases} \qquad (2.3.1)$$

where d_{core} is the core diameter of fiber, d_{FWHM} is a spot intensity FWHM for circular aperture, and λ is center wavelength of the optical pulse. The coupling efficiency is a function of NA_{lens}, but it gets more complicated than eq. (2.3.1) if $NA_{lens} > NA_{core}$. The NA_{lens} used in this experiment is 0.10 - 0.30, resulting in a spot diameter of 1.3 - 4.0 μm, and in practice NA_{lens} is not always smaller than NA_{core}. Nevertheless, it is clear that the coupling efficiency of the fiber increases as the fiber core size increases, but a large fiber core allows the propagation of a large number of modes that may interfere resulting in a loss of TPE efficiency and image resolution. For a fiber with much smaller NA_{core} than NA_{lens}, such as DCPCF16um, it has a low coupling efficiency even with a relatively large core size since the difference between NA_{lens} and NA_{core} is dominant in determining the coupling efficiency.

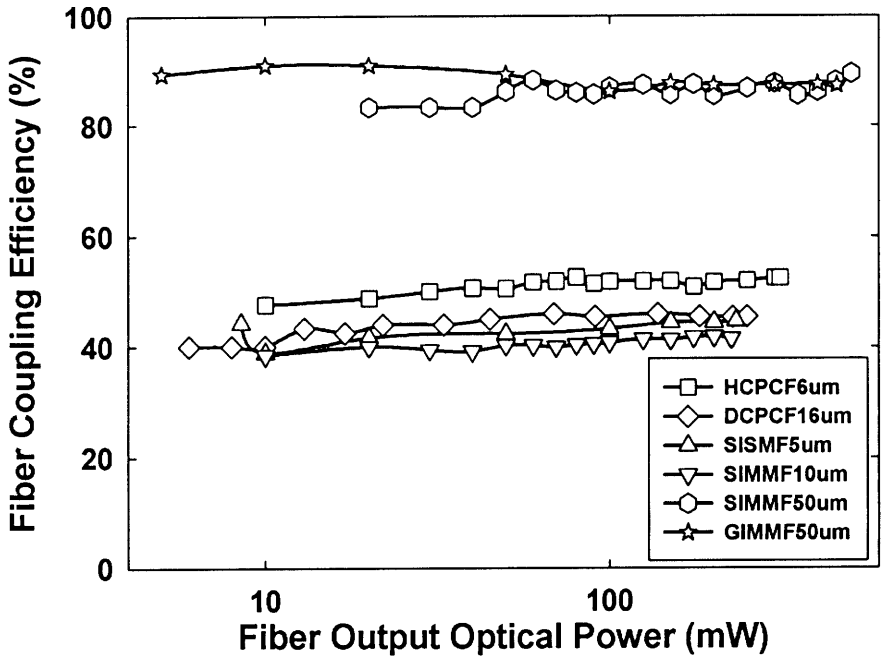

Figure 2.3 Maximum coupling efficiencies for different types of fibers are plotted. The x-axis represents the fiber output optical power on a logarithmic scale. Fiber coupling efficiency is observed to be power-independent. All small-core fibers have 40-50% efficiency, whereas most of the large-core fibers have 80-90% efficiency. Note that DCPCF16um, even with a relatively large core, has similar coupling efficiency to those of small-core ones due to its small fiber core NA.

2.3.2 Temporal and Spectral Optical Pulse Profile

To observe fiber delivery effects on the ultrafast optical pulse, the optical pulse profile should be analyzed both temporally and spectrally since the intensity spectrum complements the temporal profile in the characterization of ultrafast optical pulses. Figure 2.4 plots the temporal pulse width and the spectral bandwidth of the optical pulse with respect to fiber output optical power. Free space light delivery (denoted in figures as AIR) was also measured as a reference. From figure 2.4(a), extrapolating temporal pulse width to low optical power, the temporal pulse broadening is substantially higher than free space delivery for some fibers, indicating that dispersion effects are significant especially with small-core TIR-based fibers (SISMF5um and SIMMF10um). Moreover, they also exhibit strong power-dependent temporal broadening. TIR-based multimode fibers (SIMMF50m and GIMMF50um) and DCPCF16um are relatively power-

independent and maintain relatively short temporal pulse width until the fiber output optical power is very high. Nevertheless, the temporal pulse width of HCPCF6um is almost identical to that in free space delivery. In addition, its temporal pulse width is independent of optical power. In figure 2.4(b), the spectral bandwidth remains narrow for all fibers at low fiber output power. However, the spectra broaden as the fiber output optical power increases in TIR-based fibers (SISMF5um, SIMMF10um, SIMMF50um, and GIMMF50um). The spectral broadening is greater for smaller core fibers. Graded-index fiber (GIMMF50um) has less spectral broadening than step-index fiber (SIMMF50um) of same core size. In contrast, HCPCF6um transmits ultrafast optical pulse without any spectral distortion. Moreover, its spectral bandwidth and temporal profile are independent of fiber output optical power. DCPCF16um has nearly constant spectral bandwidth over most of the optical power range, but demonstrates very low spectral distortion at high fiber output optical power.

These observations can be explained with nonlinear fiber optics theory. From the pulse propagation equation for ultrafast optical pulse through the single-mode fiber, the length scale for dispersion and nonlinearity can be introduced, assuming that the nonlinear effects except for SPM are negligible and GVD is much larger than third order dispersion (TOD), $\beta_2 \gg \beta_3$ [11]. Dimensionless length can be also expressed as below:

$$\frac{L_D}{L_{NL}} = \frac{\gamma P_0 T_0^2}{|\beta_2|} = \frac{n_2 \omega_0}{c A_{eff}} \frac{P_0 T_0^2}{|\beta_2|} = \left(\frac{n_2 \omega_0 T_0^2}{c|\beta_2|} \right) \frac{P_0}{A_{eff}}$$
$$\text{where} \quad L_D = \frac{T_0^2}{|\beta_2|} \quad , \quad L_{NL} = \frac{1}{\gamma P_0} \quad \& \quad \gamma = \frac{n_2 \omega_0}{c A_{eff}} \tag{2.3.2}$$

L_D and L_{NL} represents dispersion length with GVD and nonlinear length respectively. β_2 is a GVD parameter, T_0 is initial pulse width, P_0 is peak power of initial optical pulse and γ is a nonlinear parameter. In addition, n_2 is a nonlinear index coefficient, ω_0 is the center frequency of initial optical pulse, c is the speed of light in a vacuum, and A_{eff} is the effective core area related to core size and core-cladding index difference. From eq. (2.3.2), the nonlinear effect dominates dispersion if L_{NL} is shorter than L_D, and vice versa. Since L_{NL} is proportional to A_{eff}, the nonlinear effects such as SPM and Kerr effect become dominant with decreasing core size.

These nonlinear effects are strongly related to the spectral broadening, irrespective of material dispersion since it is caused by phase mismatching between different wavelengths. Extrapolations of experimental results show that the pulses delivered by all the fibers have the same initial spectral bandwidths at very low optical power; this confirms the spectral bandwidth analysis of the optical pulse. For temporal broadening, its dominant factor depends on the ratio of the dispersion length to the nonlinear length. At very low optical power, chromatic dispersion is the major cause of temporal broadening. At high optical power, temporal broadening is mostly due to nonlinear effects. The level of nonlinear effects also depends on the core size of fiber.

Our experimental results for solid-core fibers (DCPCF16um, SISMF5um, SIMMF10um, and SIMMF50um) agree with this theory for TIR-based single-mode fibers. Material dispersion, in addition to chromatic dispersion, is also present, but it is the same for all fibers at a given fiber length regardless of fiber core size. Furthermore, fiber core size is also associated with the number of modes fiber can deliver. For the single-mode delivery, there is waveguide dispersion [6], which is generally negligible in our spectral range. For the multimode fibers, intermodal dispersion may exist. Therefore, total dispersion at very low optical power also depends on the number of modes, and that explains why different core size fibers show different total dispersion. Regarding fiber core types, light propagates in the graded-index core along the longer optical path compared with the step-index core due to different refractive index profile, and due to the fact that the graded-index core is designed for the light to travel along parabolic instead of linear path. For a given fiber length, greater temporal broadening due to material dispersion occurs with the graded-index fiber, and the result shows that SIMMF50um has lower temporal broadening than GIMMF50um. In addition, two multimode fibers have quite different spectral bandwidths because the spectral profile of the optical pulse depends on the propagating modes in the fiber. It is difficult to measure the spectral bandwidth for multimode fiber due to the sensitivity of propagating modes to fiber bending. Nonetheless, we observed that nonlinear effects are less apparent in large-core fibers since their spectral bandwidths are only weakly dependent on power. Although the pulse propagation equation presented in eq. (2.3.2) is derived for single-mode fibers, it does predict that the nonlinear effects in multimode fibers are not dominant due to the large effective core areas of these fibers. Furthermore, spectral bandwidth in graded-index fiber (GIMMF50um) is less affected by the nonlinear effect than that in the step-index fiber

(SIMMF50um). This difference comes from the different refractive index structures of these fibers.

For PCFs, HCPCF6um does not show material dispersion or nonlinear effects since the ultrafast optical pulse travels mostly through the hollow-core where the refractive index is uniform everywhere. In contrast, the behavior of DCPCF16um is quite different, based on differences in the mechanisms of guiding light. With MTIR-based fiber, similar to the conventional optical fiber, light propagates through material with wavelength and power-dependent refractive index.

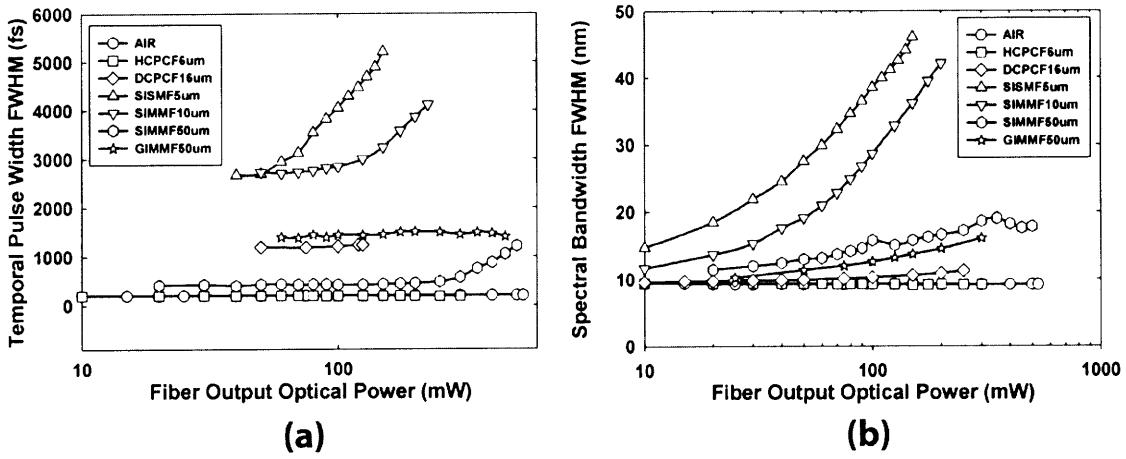

Figure 2.4 (a) Temporal pulse width and (b) spectral bandwidth of the optical pulse after various fiber delivery methods are plotted. Free space delivery is included as a reference. The x-axis represents the fiber output optical power on a logarithmic scale for both (a) and (b). HCPCF6um demonstrates intact optical pulse delivery from the experimental results.

2.4 The Performance in the Nonlinear Microscopy after Fiber Deliveries

2.4.1 Two-Photon Excitation Efficiency

TPE efficiency is the efficiency of fluorophores excited by the ultrafast optical pulses. Figure 2.5 shows TPE efficiency after various fiber deliveries as a function of power. In a log-log plot, a quadratic dependence on power implies that the power dependence should be linear with a slope of 2. TPE efficiency curves after all fiber deliveries show quadratic dependence as expected of

TPE process. In our experiments, hollow-core photonic crystal fiber (HCPCF6um) delivery has the best TPE efficiency after fiber delivery. Due to large temporal pulse width broadening, single-mode fiber (SISMF5um) delivery has the poorest TPE efficiency. TPE efficiency can be theoretically calculated as [1]:

$$n_a \approx \frac{p_0^2 \delta}{\tau_p f_p^2}\left(\frac{\left(NA_{eff}\right)^2}{2\hbar c\lambda}\right)^2 = \left[\frac{\delta}{\tau_p f_p^2}\left(\frac{\left(NA_{eff}\right)^2}{2\hbar c\lambda}\right)^2\right] p_0^2 \qquad (2.4.1)$$

where n_a is the number of photon pairs absorbed per fluorophore per pulse, τ_p is the pulse width, δ is two-photon cross section of the fluorophore at given wavelength λ, p_0 is average laser power, f_p is laser repetition rate, $\hbar$ is reduced Planck's constant, c is the speed of light in a vacuum, and NA_{eff} is the effective NA of objective lens. From eq. (2.4.1), fiber delivery does not change any parameters except for τ_p and NA_{eff}. If NA_{eff} remains constant, the coefficient of TPE efficiency is inversely proportional to τ_p, the temporal pulse width. Since τ_p often broadens with fiber delivery, the TPE efficiency is expected to decrease when light is conducted through fiber. It is interesting to note that the TPE efficiency for hollow-core PCF (HCPCF6um) is significantly lower than free space delivery, even though both spectral bandwidths and temporal pulse widths are comparable for both delivery methods. The discrepancy between the theory and the measurement may originate from the fact that the fiber output light is not single mode and hence there is effectively lower NA. Another possibility is that this TPE theory assumes that optical pulse delivered through fiber is transform-limited, or chirp-free optical pulse. It has been reported that TOD can be significant in PCFs, and the balance between normal GVD and TOD results in soliton-like behavior, resisting dispersion of ultrafast pulses in some cases [25]. However, the phase shift induced by these high order dispersions can also generate chirping of the pulses as well as change pulse shapes. Since optical pulse shape plays major role in TPE efficiency [42], and the temporal width of the autocorrelation profile cannot determine whether the pulse is chirped or chirp-free, chirping effect may be another major cause of deteriorating TPE efficiency. If intermodal dispersion is induced, TPE efficiency can decrease significantly since TPE process is sensitive to the wavefront mismatch caused by intermodal dispersion.

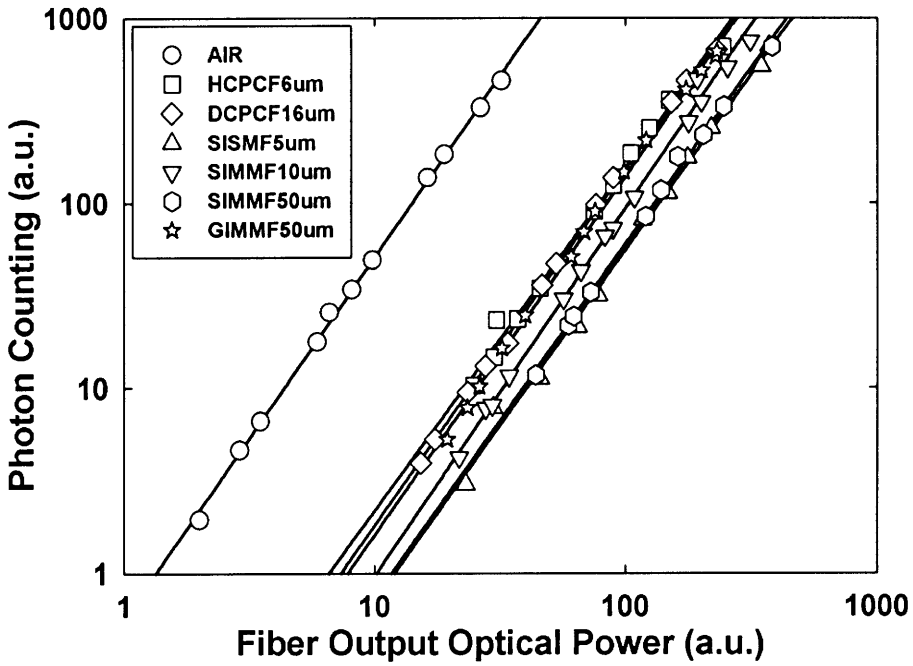

Figure 2.5 TPE efficiency in a TPE fluorescence microscope with light pulses delivered by different fibers. Quadratic dependence of sample fluorescence as a function of power indicates TPE process. Fiber delivery is much less efficient for TPE than for free space delivery. Among all the fibers tested, HCPCF6um is the most efficient fiber delivery medium.

2.4.2 Point Spread Function

Optical resolution is usually defined by the Rayleigh criterion that can be operationally quantified from the FWHM of the PSF. Figure 2.6 shows the measurements of both lateral and axial PSF for the TPE fluorescence microscope after light is delivered by the different fibers. For each fiber delivery method, top figures are the intensity profiles of a point source in the solution, and bottom figures show the FWHM measurements. As seen in the figures, the FWHM of lateral PSF increases with the number of modes that the fiber delivers, whereas the FWHM of axial PSF is not sensitive to the number of modes delivered.

Theoretically, the excitation PSF determines the optical resolution in the TPE fluorescence microscope with a photodetector such as PMT. The excitation PSF intensity profile can be calculated as shown by So et al. [2], and the lateral and the axial optical resolution can be estimated, using a Gaussian fit of the PSF [43].

$$FWHM_{xy} = \begin{cases} \dfrac{0.533\lambda}{\sqrt{2}NA_{eff}} & NA_{eff} \le 0.7 \\ \dfrac{0.541\lambda}{\sqrt{2}NA_{eff}^{0.91}} & NA_{eff} > 0.7 \end{cases} \qquad FWHM_z = \frac{0.886\lambda}{\sqrt{2}}\left[\frac{1}{n-\sqrt{n^2-NA_{eff}^2}}\right]$$

(2.4.2)

n is effective refractive index of the specimen, $FWHM_{xy}$ is the FWHM of lateral PSF and $FWHM_z$ is the FWHM of axial PSF function. As expressed in eq. (2.4.2), optical resolution is determined by NA_{eff} and λ. However, the basic assumption for above equations is that the illumination light has a distortion-free wavefront and its intensity is uniform in the lateral direction. The lateral PSF profile depends on the number of modes delivered. When it is close to unity, the experimentally measured PSF is close to the theoretical value; otherwise, the lateral optical resolution is degraded. The axial resolution was found to be less dependent on the delivery modes, which may be a result of the lateral nature of these spatial modes. In eq. (2.4.2), axial resolution is found to be more sensitive to the objective NA and the refractive index of the sample, but they are irrelevant to our experimental results since same objective and sample were used. The effect of spatial modes on axial resolution requires further investigation.

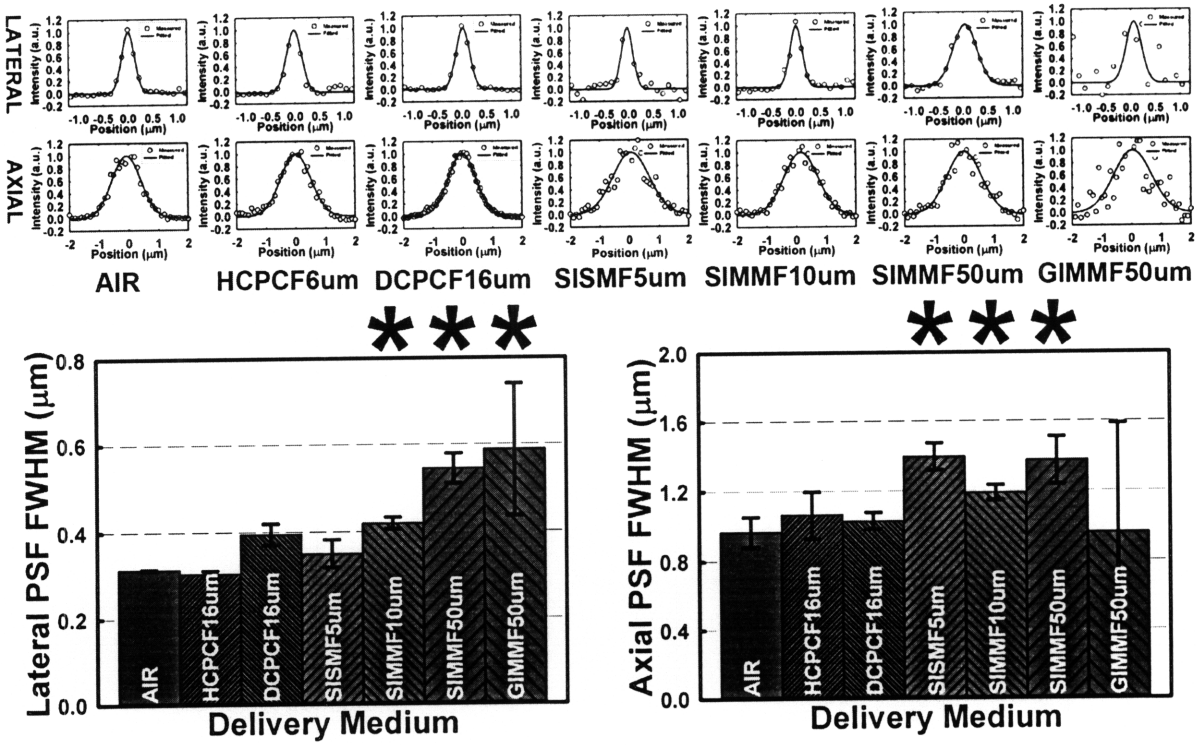

Figure 2.6 PSFs in a TPE fluorescence microscope using different fiber delivery methods. The top figures show both the lateral and the axial PSF measurements with light delivered through various fibers. Free space delivery is included for comparison. Bottom figures represent statistical analysis of the lateral and the axial PSF FWHMs for each delivery method. The lateral resolution is dependent on the number of modes that the fiber supports, whereas the axial resolution is almost independent of delivery method. The symbol * above bars, indicates that optical resolution is statistically different from free space delivery, based on a t-test with $P<0.05$.

2.4.3 Two-Photon Excitation Fluorescence Imaging

The resolution of the TPE fluorescence microscope was further evaluated in the imaging of biological specimen. Using optical fiber for light delivery, the TPE fluorescence microscope can effectively image human skin. Human tissue was fixed and H&E (haematoxylin and eosin) stained. Eosin [44] produces fluorescence during two-photon imaging. With the 40× oil-immersion objective lens (NA=1.3), the image field of view was 120 μm by 120 μm. Figure 2.7(a) shows human skin fluorescence images taken using different fibers for light delivery. In terms of image resolution and detail, the difference between fiber delivery methods appears to be minimal. In order to better quantify these differences, we used power spectral image analysis [45,

46]. The power spectra for human skin were measured with different fiber delivery methods in the figure 2.7(b). As expected, image power spectra confirm the results of the lateral PSF measurements. Images with single-mode fibers have higher power spectral density than those with multimode fibers at a given spatial frequency range where tissue details exist. At high spatial frequency region, there is no power spectral density difference for different delivery methods since these high frequency features are dominated by photon shot noise in the image.

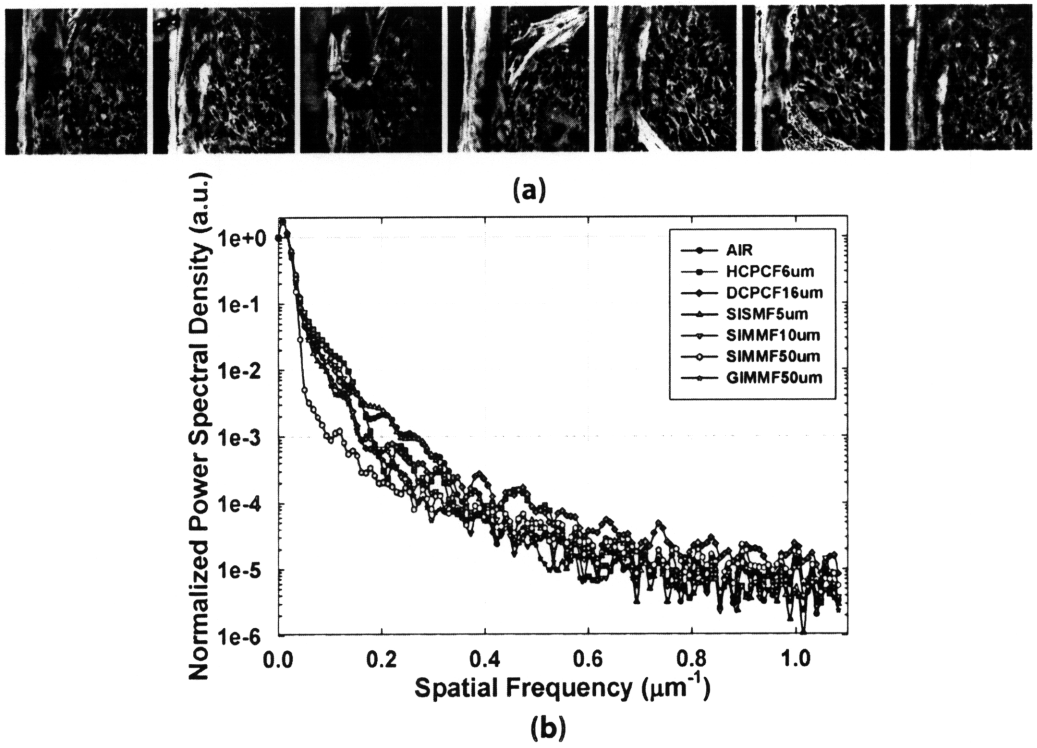

Figure 2.7 (a) TPE fluorescence images for H&E-stained ex-vivo human skin with different fiber delivery methods. From left to right: AIR, HCPCF6um, DCPCF16um, SISMF5um, SIMMF10um, SIMMF50um and GIMMF50um (b) The power spectra of images obtained with different fiber delivery methods. Power spectral image analysis was performed on a series of human skin images obtained in (a). At low spatial frequency range, the images acquired using fibers with small number of modes delivered have higher power spectral densities than those with large number of modes. At high spatial frequency region, power spectral density levels for all the fiber delivery methods, including free space delivery, are same since noise dominates at this regime. The maximum spatial frequency for given NA is 2.3 μm^{-1}

2.5 Linear Prechirping Effects for the Fiber Deliveries

Temporal pulse broadening degrades the TPE efficiency, which is inversely proportional to the temporal pulse width. The major cause of the pulse broadening originates from chromatic dispersion where material dispersion is dominant. To eliminate the broadening effect, an optical pulse compressor is often used for prechirping the pulses linearly [8]. The pulse compressor mainly consists of a reflective diffraction grating pair configured so that the blue components of the optical pulse propagate faster than its red components [7], in contrast to the chirping that occurs in the optical fiber delivery. This effect is called linear prechirping and increases with the grating pair separation. At the grating pair separation where linear prechirping cancels out chromatic dispersion, the optical pulse width can be restored close to original one after the delivery in the fiber. We measured the impact of the linear prechirping on the TPE coefficient as well as on the optical pulse profile. Large-core fibers (SIMMF50um and GIMMF50um) were not used in these experiments since they do not provide good optical resolutions for nonlinear microscopy imaging. In the following discussion, a suffix '.PC' after the fiber name indicates the linearly prechirped result.

2.5.1 Effects of Linear Prechirping on Ultrafast Optical Pulse

Figure 2.8 shows linear prechirping results of the ultrafast optical pulse. The optical pulses after the fiber deliveries with the linear prechirping were measured with respect to the grating pair separation. As shown in figure 2.8(a), the linear prechirping only broadens the pulses for free space (AIR.PC) and hollow-core fiber (HCPCF6um.PC) since the optical pulses which travel through them are chirp-free. For solid-core fibers (DCPCF16um.PC, SISMF5um.PC and SIMMF10um.PC), prechirping is quite effective, but this procedure cannot completely restore the optical pulse back to the original temporal width. As for the prechirping effect on the spectral bandwidth, spectral narrowing occurs for all the fibers, while a little spectral broadening is shown in free space delivery. (See figure 2.8(b).) At the optimal grating pair separation where minimum temporal pulse width was obtained, we measured the temporal pulse width and the spectral bandwidth for solid-core fibers as the functions of fiber output optical power in figure 2.8(c) and 2.8(d), respectively. Note that free space delivery and the hollow-core PCF cases are not shown since their pulse profiles are already optimal with no prechirping. Similar to the

results without linear prechirping, both the temporal and the spectral broadening of the optical pulses are dependent on the fiber output optical power.

Transform-limited ultrafast optical pulses become prechirped or negatively chirped through pulse compression. There may be further temporal broadening due to phase mismatching and the spectral broadening caused by the residual phase distortion [47]. For HCPCF6um.PC, prechirping the optical pulse results in some temporal broadening and spectral narrowing, a behavior that is different from free space delivery. Both DCPCF16um.PC and SIMMF10um.PC have similar pulse compression behaviors for a given fiber length since material dispersion is dominant. The optical grating pair separations to optimize their pulse profiles are also comparable. However, SISMF5um.PC requires much longer distance between gratings to compensate for pulse broadening. This means that the optical pulse delivered with single-mode fiber has additional pulse broadening due to the nonlinear effects in this smaller core fibers. It is interesting to observe that spectral narrowing occurs with solid-core fibers; this observation agrees with spectral narrowing due to SPM [48]. Even after the temporal pulse width is optimized using the pulse compressor, we observe that the pulse profiles for some fibers can be quite different from the original transform-limited condition and the pulse profiles show power dependence due to the nonlinear effects such as SPM and Kerr effect. Finally, our observations for the behaviors of SISMF5um and SIMMF10um for nonlinear microscopy imaging are also consistent with the observation of Helmchen et al. [9].

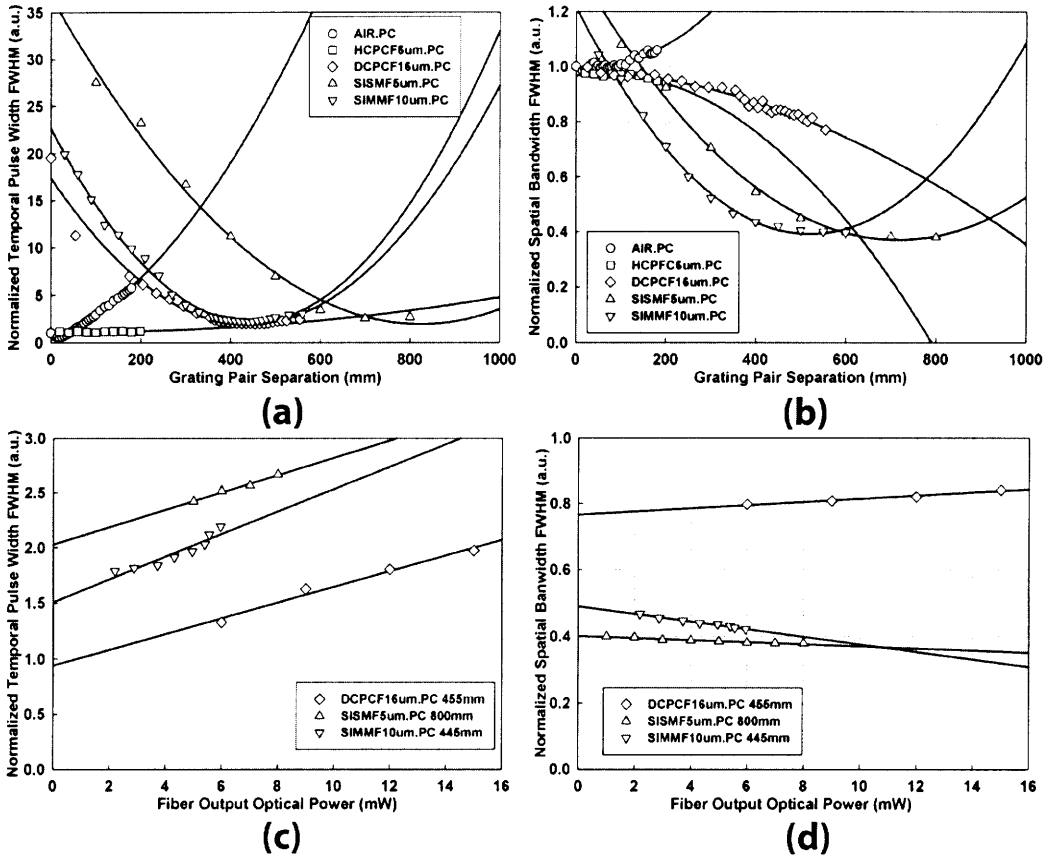

Figure 2.8 The effects of linear prechirping on (a) temporal pulse width and (b) spectral bandwidth of the optical pulse with respect to grating pair separation are shown. At the optimal grating pair separation in the pulse compressor, power dependence is also observed in terms of (c) temporal pulse width and (d) spectral bandwidth.

2.5.2 Effects of Linear Prechirping on Nonlinear Microscopy Performance

Figure 2.9 shows the impact of linear prechirping on the TPE efficiency. The TPE efficiencies for the different fiber deliveries were normalized to that of free space delivery with chirp-free optical pulse, and they are inversely proportional to the temporal pulse widths as shown in the figure 2.8(a). In the TPE efficiency curve, the grating pair separation to maximize TPE efficiency is slightly longer than the distance that minimizes temporal pulse width. This effect is caused by the additional dispersion introduced by the optical components such as the objective in the microscope. Without the linear chirping, HCPCF6um has the best TPE efficiency although it is still 20 times worse than free space delivery. However, with linear prechirping, the TPE

efficiency for solid-core fibers can be significantly improved. At optimal prechirping, the TPE efficiencies of DCPCF16um.PC and SISMF5um.PC are factor of two higher than that of the free space delivery.

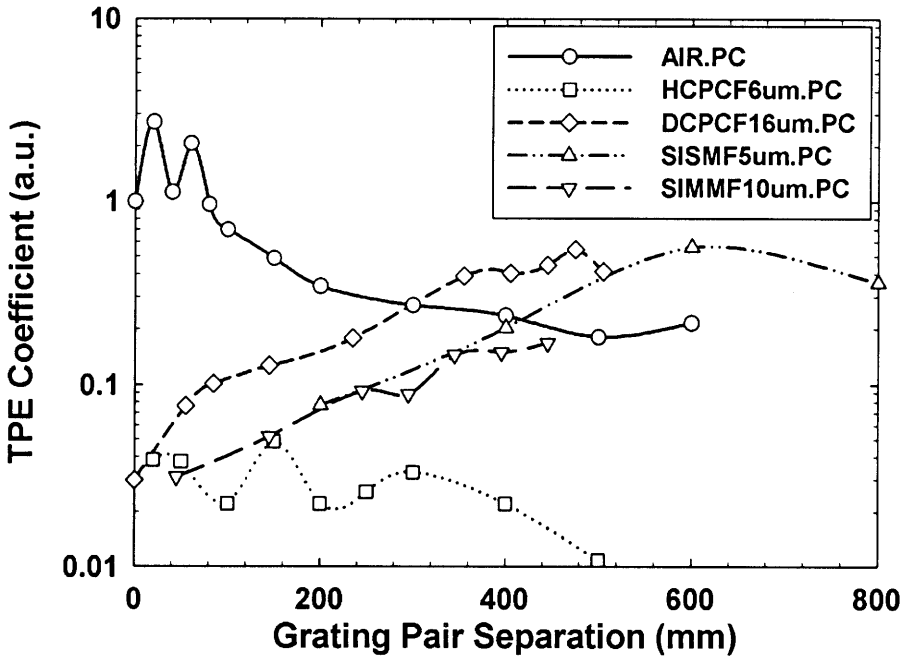

Figure 2.9 The normalized TPE coefficients affected by the linear prechirping were measured as a function of the grating pair separation. The TPE coefficient for each fiber delivery was measured and normalized by that of the chirp-free optical pulse delivery in the free space.

2.6 Summary

In this chapter, we characterized the performance of a variety of optical fibers that may be used for nonlinear optical microscopy. We observed ultrafast optical pulse profile both temporally and spectrally. Spectral bandwidth is sensitive to the nonlinear effects such as SPM and Kerr effect, whereas the temporal pulse width is affected by both nonlinear effects and chromatic dispersion. The nonlinear effects originate from the nonlinearity of refractive index in the fiber core materials. We measured the TPE fluorescence microscopy performance in terms of the TPE efficiency and optical resolution. A TPE process was observed for all fiber delivery methods, but their signal levels depend on spectral bandwidth, temporal pulse width, spatial intensity profile,

and phase mismatch induced by mode shape, chirping, and intermodal dispersion. Optical resolution was evaluated by PSF measurements. We observed that the optical resolution is relatively insensitive to the laser pulse temporal profile, albeit more sensitive laterally than axially. In addition, the linear prechirping is important to maximize the TPE efficiency of solid-core TIR-based and MTIR-based fibers.

In summary, the double-clad PCF and some step-index single-mode fibers are strong candidates for delivering the ultrafast optical pulse for the nonlinear microscopy and the TPE microendoscopy with linear prechirping. However, it should be noted that the performances of these fibers are power-dependent and generally degrade with high power. Since this power degradation behavior is relatively modest for the typical power level used in nonlinear microscope imaging, it is more important to optimize the linear prechirping for different fiber lengths. Although the hollow-core PCF appears to have excellent pulse characteristics after the delivery, its TPE efficiency is not acceptable for most nonlinear microscope applications. The reason for the low TPE efficiency is not fully understood and further investigations based on modal analysis and spatio-temporal analysis using FROG are needed. Nonetheless, this fiber may be used where high power delivery is required without any power-dependent nonlinearity, such as in constructing portable MMM.

References

1. W. Denk, J. H. Strickler, and W. W. Webb, "Two-Photon Laser Scanning Fluorescence Microscopy," Science **248**, 73-76 (1990).
2. P. T. C. So, C. Y. Dong, B. R. Masters, and K. M. Berland, "Two-photon excitation fluorescence microscopy," Annual Review of Biomedical Engineering **2**, 399-429 (2000).
3. B. A. Flusberg, E. D. Cocker, W. Piyawattanametha, J. C. Jung, E. L. M. Cheung, and M. J. Schnitzer, "Fiber-optic fluorescence imaging," Nature Methods **2**, 941-950 (2005).
4. C. H. Yu, S. P. Tai, C. T. Kung, I. J. Wang, H. C. Yu, H. J. Huang, W. J. Lee, Y. F. Chan, and C. K. Sun, "In vivo and ex vivo imaging of intra-tissue elastic fibers using third-harmonic-generation microscopy," Optics Express **15**, 11167-11177 (2007).
5. C. L. Evans, X. Y. Xu, S. Kesari, X. S. Xie, S. T. C. Wong, and G. S. Young, "Chemically-selective imaging of brain structures with CARS microscopy," Optics Express **15**, 12076-12087 (2007).
6. A. K. Ghatak, and K. Thyagarajan, *An introduction to fiber optics* (Cambridge University Press, Cambridge ; New York, 1998).
7. E. B. Treacy, "Compression of picosecond light pulses," Physics Letters A **28**, 34-35 (1968).

8. R. L. Fork, O. E. Martinez, and J. P. Gordon, "Negative Dispersion Using Pairs of Prisms," Optics Letters **9**, 150-152 (1984).
9. F. Helmchen, D. W. Tank, and W. Denk, "Enhanced two-photon excitation through optical fiber by single-mode propagation in a large core," Applied Optics **41**, 2930-2934 (2002).
10. M. T. Myaing, J. Y. Ye, T. B. Norris, T. Thomas, J. R. Baker, W. J. Wadsworth, G. Bouwmans, J. C. Knight, and P. S. J. Russell, "Enhanced two-photon biosensing with double-clad photonic crystal fibers," Optics Letters **28**, 1224-1226 (2003).
11. G. P. Agrawal, *Nonlinear fiber optics* (Academic Press, San Diego, 2001).
12. T. A. Birks, P. J. Roberts, P. S. J. Russel, D. M. Atkin, and T. J. Shepherd, "Full 2-D Photonic Bandgaps in Silica/Air Structures," Electronics Letters **31**, 1941-1943 (1995).
13. J. C. Knight, J. Broeng, T. A. Birks, and P. S. J. Russel, "Photonic band cap guidance in optical fibers," Science **282**, 1476-1478 (1998).
14. R. F. Cregan, B. J. Mangan, J. C. Knight, T. A. Birks, P. S. Russell, P. J. Roberts, and D. C. Allan, "Single-mode photonic band gap guidance of light in air," Science **285**, 1537-1539 (1999).
15. J. M. Lourtioz, *Photonic crystals : towards nanoscale photonic devices* (Springer, Berlin, 2005).
16. F. Zolla, *Foundations of photonic crystal fibres* (World Scientific, Hackensack, N.J., 2005).
17. S. G. Johnson, and J. D. Joannopoulos, *Photonic crystals : the road from theory to practice* (Kluwer Academic Publishers, Boston, 2002).
18. J. C. Knight, T. A. Birks, P. S. Russell, and D. M. Atkin, "All-silica single-mode optical fiber with photonic crystal cladding," Optics Letters **21**, 1547-1549 (1996).
19. J. C. Knight, T. A. Birks, P. S. J. Russell, and D. M. Atkin, "All-silica single-mode optical fiber with photonic crystal cladding: Errata," Optics Letters **22**, 484-485 (1997).
20. T. A. Birks, J. C. Knight, and P. S. Russell, "Endlessly single-mode photonic crystal fiber," Optics Letters **22**, 961-963 (1997).
21. J. C. Knight, T. A. Birks, R. F. Cregan, P. S. Russell, and J. P. de Sandro, "Large mode area photonic crystal fibre," Electronics Letters **34**, 1347-1348 (1998).
22. W. J. Wadsworth, J. C. Knight, A. Ortigosa-Blanch, J. Arriaga, E. Silvestre, and P. S. J. Russell, "Soliton effects in photonic crystal fibres at 850 nm," Electronics Letters **36**, 53-55 (2000).
23. A. V. Husakou, and J. Herrmann, "Supercontinuum generation of higher-order solitons by fission in photonic crystal fibers," Physical Review Letters **8720** (2001).
24. G. Renversez, B. Kuhlmey, and R. McPhedran, "Dispersion management with microstructured optical fibers: ultraflattened chromatic dispersion with low losses," Optics Letters **28**, 989-991 (2003).
25. D. G. Ouzounov, F. R. Ahmad, D. Muller, N. Venkataraman, M. T. Gallagher, M. G. Thomas, J. Silcox, K. W. Koch, and A. L. Gaeta, "Generation of megawatt optical solitons in hollow-core photonic band-gap fibers," Science **301**, 1702-1704 (2003).
26. F. Benabid, J. C. Knight, G. Antonopoulos, and P. S. J. Russell, "Stimulated Raman scattering in hydrogen-filled hollow-core photonic crystal fiber," Science **298**, 399-402 (2002).
27. S. D. Hart, G. R. Maskaly, B. Temelkuran, P. H. Prideaux, J. D. Joannopoulos, and Y. Fink, "External reflection from omnidirectional dielectric mirror fibers," Science **296**, 510-513 (2002).

28. Y. Fink, J. N. Winn, S. H. Fan, C. P. Chen, J. Michel, J. D. Joannopoulos, and E. L. Thomas, "A dielectric omnidirectional reflector," Science **282**, 1679-1682 (1998).
29. B. Temelkuran, S. D. Hart, G. Benoit, J. D. Joannopoulos, and Y. Fink, "Wavelength-scalable hollow optical fibres with large photonic bandgaps for CO2 laser transmission," Nature **420**, 650-653 (2002).
30. P. Russell, "Photonic crystal fibers," Science **299**, 358-362 (2003).
31. J. C. Knight, "Photonic crystal fibres," Nature **424**, 847-851 (2003).
32. A. Argyros, M. A. van Eijkelenborg, M. C. J. Large, and I. M. Bassett, "Hollow-core microstructured polymer optical fiber," Optics Letters **31**, 172-174 (2006).
33. D. Bird, and M. Gu, "Fibre-optic two-photon scanning fluorescence microscopy," Journal of Microscopy-Oxford **208**, 35-48 (2002).
34. A. Lago, A. T. Obeidat, A. E. Kaplan, J. B. Khurgin, P. L. Shkolnikov, and M. D. Stern, "2-Photon-Induced Fluorescence of Biological Markers Based on Optical Fibers," Optics Letters **20**, 2054-2056 (1995).
35. S. P. Tai, M. C. Chan, T. H. Tsai, S. H. Guol, L. J. Chen, and C. K. Sun, "Two-photon fluorescence microscope with a hollow-core photonic crystal fiber," Optics Express **12**, 6122-6128 (2004).
36. W. Gobel, A. Nimmerjahn, and F. Helmchen, "Distortion-free delivery of nanojoule femtosecond pulses from a Ti : sapphire laser through a hollow-core photonic crystal fiber," Optics Letters **29**, 1285-1287 (2004).
37. G. McConnell, and E. Riis, "Two-photon laser scanning fluorescence microscopy using photonic crystal fiber," Journal of Biomedical Optics **9**, 922-927 (2004).
38. L. Fu, X. S. Gan, and M. Gu, "Nonlinear optical microscopy based on double-clad photonic crystal fibers," Optics Express **13**, 5528-5534 (2005).
39. D. Kim, K. H. Kim, S. Yazdanfar, and P. T. C. So, "Optical biopsy in high-speed handheld miniaturized multifocal multiphoton microscopy," in *Multiphoton Microscopy in the Biomedical Sciences V*(SPIE, San Jose, CA, USA, 2005), pp. 14-22.
40. C. Rullière, *Femtosecond laser pulses : principles and experiments* (Springer Science+Business Media, New York, 2005).
41. R. Trebino, *Frequency-resolved optical gating : the measurement of ultrashort laser pulses* (Kluwer Academic, Boston, 2000).
42. C. J. Bardeen, V. V. Yakovlev, J. A. Squier, K. R. Wilson, S. D. Carpenter, and P. M. Weber, "Effect of pulse shape on the efficiency of multiphoton processes: Implications for biological microscopy," Journal of Biomedical Optics **4**, 362-367 (1999).
43. W. R. Zipfel, R. M. Williams, and W. W. Webb, "Nonlinear magic: multiphoton microscopy in the biosciences," Nature Biotechnology **21**, 1368-1376 (2003).
44. I. B. Berlman, *Handbook of fluorescence spectra of aromatic molecules* (Academic Press, New York,, 1971).
45. J. S. Lim, *Two-dimensional signal and image processing* (Prentice Hall, Englewood Cliffs, N.J., 1990).
46. A. V. Oppenheim, R. W. Schafer, and J. R. Buck, *Discrete-time signal processing* (Prentice Hall, Upper Saddle River, N.J., 1999).
47. B. R. Washburn, J. A. Buck, and S. E. Ralph, "Transform-limited spectral compression due to self-phase modulation in fibers," Optics Letters **25**, 445-447 (2000).
48. M. Oberthaler, and R. A. Hopfel, "Special Narrowing of Ultrashort Laser-Pulses by Self-Phase Modulation in Optical Fibers," Applied Physics Letters **63**, 1017-1019 (1993).

Chapter 3

Depth-Resolved Wide-Field Illumination (DRWFI): Optimization and Evaluation

3.1 Introduction

Laser scanning optical microscopies including confocal microscopy [1], TPM [2, 3], and CARS microscopy [4] have optical sectioning capability. These techniques focus the excitation light to a diffraction-limited spot and obtain depth discrimination capability either by using a conjugated detection pinhole or by using nonlinear optical responses of materials. Since signal is produced from a localized focus, 3D structures must be mapped by sequentially raster scanning this focus in 3D. The sequential nature of raster scanning is inherently slower than parallel imaging process where signals from a whole plane are mapped into an imaging sensor such as in the fluorescence microscopy that uses wide-field illumination. Until recently, there has been no wide field imaging method with 3D resolution. DRWFI was first achieved by the introduction of scanningless two-photon excitation microscopy using the concept of temporal focusing [5, 6]. While one may contend that the spinning-disc confocal microscopy [7, 8] or the multifocal multiphoton microscopy [9-12] has achieved DRWFI, these techniques still rely on scanning a parallel array of spots and not simultaneously acquiring information from all locations in the specimen plane. The DRWFI systems based on temporal focusing use a diffraction grating to control the temporal pulse width along optical axis. The high-speed potential of the DRWFI may find applications in biological imaging that have previously utilized scanning microscopy [13-15] and in 3D laser direct writing based on spatial focusing [16-18]. In addition, DRWFI can be combined with stochastic optical reconstruction microscopy (STORM) [19, 20] or photo-activated localization microscopy (PALM) [21, 22] to extend this class of super-resolution imaging to 3D.

Although DRWFI has been around for almost five years, its imaging capabilities have not been fully characterized and the design considerations in a DRWFI system remain to be better defined [5, 6]. In this thesis, we undertake a systematic approach to evaluate the optical imaging performance of TPE based DRWFI. More importantly, DRWFI has been very slowly adapted despite its many advantages. The strength of DRWFI is its ability to simultaneously excite an area. However, for efficient excitation of most fluorophores, the available power from standard Ti:Sapphire lasers limits the field of view (FOV) of DRWFI to several hundreds of square microns. Due to the quadratic dependence of fluorescence signal to the excitation power in TPE, DRWFI becomes less efficient for larger FOVs than even sequential single focus scanning in terms of image frame rate. This thesis further explores the possibility of overcoming this limitation by using contrast agents with high two-photon cross sections. Specifically, we use water-soluble QDs which have been reported to have extraordinarily high two-photon cross sections [23].

In this chapter, the DRWFI based on temporal focusing is introduced. Mathematical model based on the diffraction theory is derived to predict optical sectioning capability in DRWFI. This mathematical model further allows us to optimize the design parameters of a DRWFI system based on numerical simulation. Then, a practical implementation of the TPE DRWFI microcopy is described. Simulation results are compared with experimental measurement in terms of axial optical resolution. In addition, high sensitivity and high-speed imaging of this TPE DRWFI system are demonstrated by imaging single QD.

3.2 Depth-Resolved Wide-Field Illumination

In this section, the basic principle of DRWFI based on temporal focusing is discussed. The first requirement to generate temporal focusing is to control the width of ultrafast pulses or their dispersion. Basically, dispersion in an optical pulse occurs due to optical path difference between its different spectral components. When all the wavelength components in the optical pulse propagate along the same optical path in free space, optical pulse shape does not change and there is no dispersion. In case of the aberration-free lens, optical path lengths from the back focal plane to the front focal plane are same in a 4-f system, independent of the incidence angle of the

ray relative to the optical axis. Temporal focusing principle can be realized in this 4-f system by introducing a dispersive element in the back focal plane of the tube lens by sending different spectral components of an optical pulse to different directions (different incident angles relative to the optical axis). By the definition of being aberration-free (including chromatic aberration), these different spectral components have the same path lengths to the front focal plane where they recombine (See figure 3.1 inset). When all the wavelength components recombine, the ultrafast pulses retain their narrow femtosecond pulse width. For the 4-f system, this path length matching property is true only between the back focal plane of tube lens and the front focal plane of the objective, but not anywhere else. Therefore, outside the focal plane, the path lengths for the different spectral components are different, the pulses broaden, and the TPE efficiency decreases. The optical component used in the optical element can be any spectral-dependent angular dispersive element such as diffraction grating, prism, acousto-optic modulator (AOM), and spatial light modulator (SLM).

Figure 3.1 graphically demonstrates the principle of DRWFI. In the figure 3.1 inset, ultrafast optical pulse is incident on the surface of the reflective diffraction grating. The different spectral components of the ultrafast pulse are dispersed to different angles. Note that figure 3.1 shows only three different color monochromatic waves for illustration purpose, but in reality, actual monochromatic waves disperse continuously in space. After the grating, each monochromatic wave has a different optical path, and the ultrafast optical pulse is broadened between grating and focal plane of the objective, as dictated by the invariance of the time-bandwidth product. The tube lens focuses the wave at the back aperture of the objective as shown in figure 3.1. After the objective, each wave is collimated but arrives to the focal plane with different converging angle. Along the optical axis, the beam diameter of each wave starts overlapping partially as waves approach to the focal plane where they are completely overlapped. The temporal pulse width of the optical pulse at optical axis reaches a minimum or fully restored at the focal plane. As the waves propagate out of the focal plane, temporal pulse width of the optical pulse broadens, and the beamlets from the different spectral components no longer overlap. Since fluorescence yield is inversely proportional to the pulse width in the case of two-photon absorption process, most of the fluorescence is generated at the focal plane in this scheme resulting in an intrinsic optical sectioning effect.

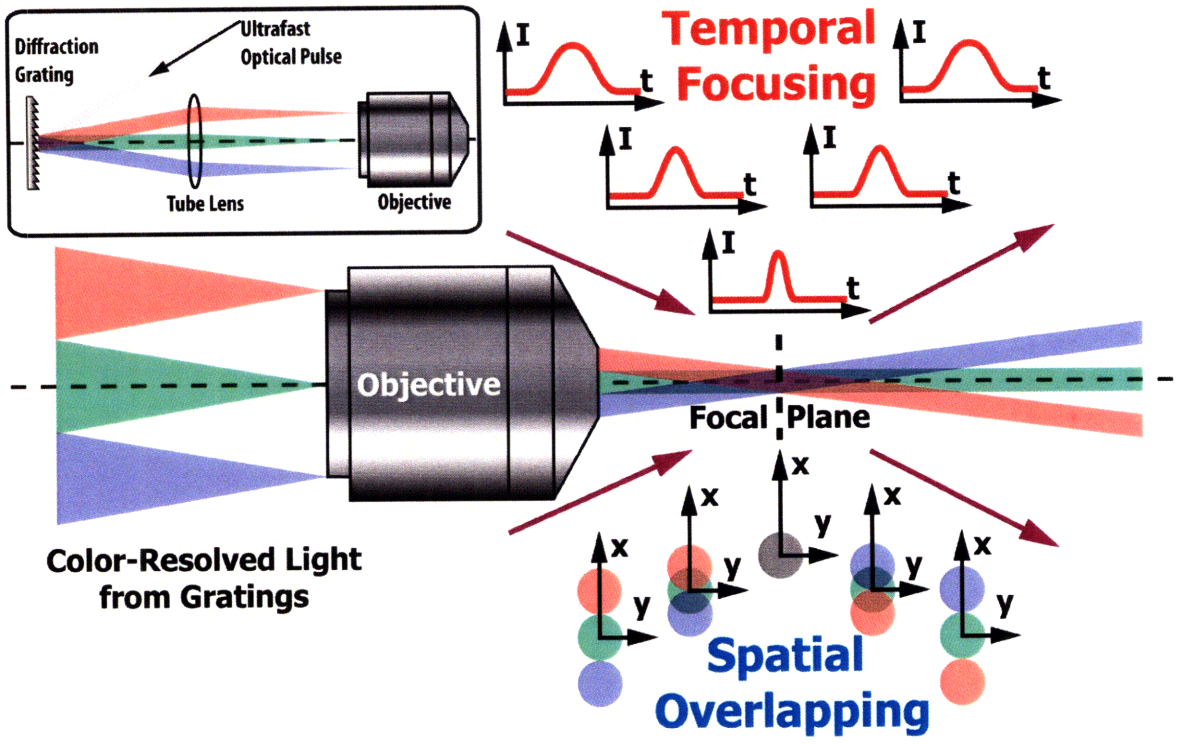

Figure 3.1 A depiction of DRWFI. Inset shows how the color-resolved light is generated before the objective

3.3 Mathematical Model for DRWFI

Here we are motivated to thoroughly understand the theoretical underpinning of the image formation in our approach. We derive an optical model of light distribution near the focal plane based on diffraction theory [24-27] to evaluate axial optical resolution with axial intensity distribution. This optical model allows us to accurately predict the axial optical resolution that can be achieved. Furthermore, it makes us examine the effects of different design parameter choices in optimizing optical sectioning capability.

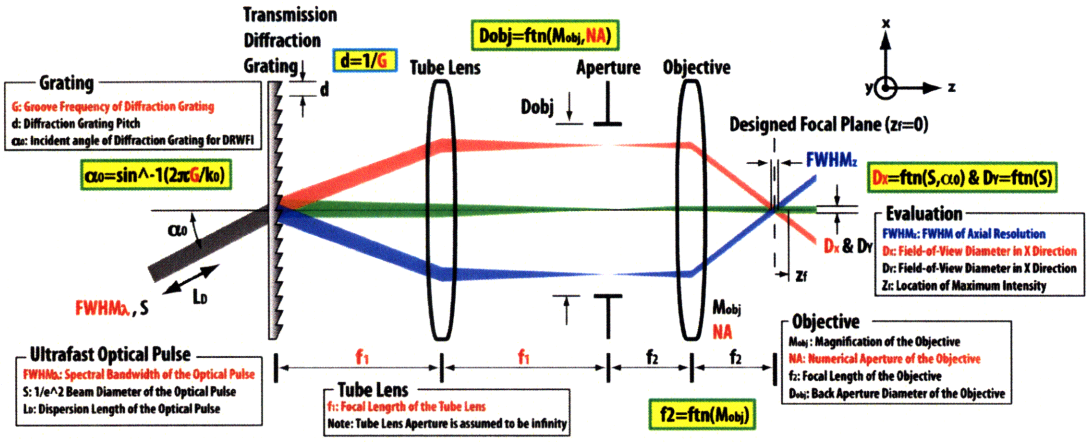

Figure 3.2 Parameters for DRWFI. The physical parameters for the simulation are listed. Red and blue indicate key design parameters and evaluation parameter, respectively.

Figure 3.2 shows how light propagates through an optical system. To simplify this model, the following assumptions are applied: 1) the optical model is diffraction-limited, 2) all the lenses are perfectly chromatic-aberration-corrected, 3) dispersion occurs only at the diffraction grating, 4) the input beam profile is Gaussian with a width of S ($1/e^2$ beam radius), 5) the spectral distribution of the input beam is also Gaussian with a bandwidth of K in terms of the wavenumber, and 6) the ultrafast optical pulse is chirp-free. Then ultrafast optical pulse can be defined as below:

$$U(x,y,z,t)=\int_{-\infty}^{+\infty}U(\vec{r},k)e^{i(\vec{k}\cdot\vec{r}-\omega t)}\,d\omega = c\int_{-\infty}^{+\infty}U(x,y)e^{ikz}W(k)e^{-ikct}\,dk$$

$$\text{where}\quad U(x,y)=A_0\exp\left\{-\frac{x^2+y^2}{S^2}\right\}\ \text{and}\ W(k)=B_0\exp\left\{\frac{\Delta k^2}{K^2}\right\} \qquad (3.3.1)$$

A_0 and B_0 are the amplitudes, and $\Delta k = k - k_0$ is the difference between $k = 2\pi/\lambda = \omega/c$, the wavenumber for the given wavelength, and k_0, the wavenumber for the center wavelength. Moreover, λ is wavelength, ω is optical angular frequency, and c is the speed of light in a vacuum. Since diffraction theory is valid for monochromatic wave, divide and conquer (D&C) method is applied: the optical pulse separates into monochromatic wave components, the electromagnetic wave fields are calculated with diffraction theory, and the time domain behavior at the focal plane is obtained by recombining the spectral components. For each k, the transverse field at grating surface [28] can be written as

$$U_1(x_i, y_i, k) = U(x_i \cos\alpha, y_i) \cdot \exp\{i \cdot \Delta k \sin\alpha_0 \cdot x_i\} \tag{3.3.2}$$

(x_i, y_i) is the lateral coordinate at the grating plane. The grating effectively introduces a phase chirp along one direction. $\alpha_0 = \sin^{-1}(2\pi G/k_0)$ is the incident angle of the light incident upon the grating, with groove frequency G, such that the center wavelength of the input beam propagates along the optical axis. Since the grating and the microscope focal plane are conjugated by a 4-f imaging system, the field can be readily predicted along the optical path. Ignoring the field aperture of the microscope, the field at back aperture of the objective is

$$U_2(x_b, y_b, k) = -ik \frac{\exp\{ik2f_1\}}{2\pi f_1} \int_{-\infty}^{+\infty}\int_{-\infty}^{+\infty} U_1(x_i, y_i, k) \exp\left\{-ik \frac{x_b x_i + y_b y_i}{f_1}\right\} dx_i\, dy_i \tag{3.3.3}$$

f_1 is the focal length of the tube lens, and (x_b, y_b) is the lateral coordinate of the back aperture plane. When the waves propagate into the objective, the back aperture size in the objective should be considered, and it is incorporated as:

$$U_3(x_b, y_b, k) = U_2(x_b, y_b, k) \cdot circ\left(\frac{\sqrt{x_b^2 + y_b^2}}{D/2}\right)$$

$$\text{where} \quad circ(r) = \begin{cases} 1 & \text{for } |r| < 1 \\ 1/2 & \text{for } |r| = 1 \\ 0 & \text{Otherwise} \end{cases} \tag{3.3.4}$$

D is the diameter of the back aperture in the objective. The field near the focal plane of the objective can be calculated as:

$$U_4(x_f, y_f, z_f, k)$$
$$= -ik \frac{\exp\{ik(2f_2 + z_f)\}}{2\pi f_1} \int_{-\infty}^{+\infty}\int_{-\infty}^{+\infty} U_3(x_b, y_b, k) \exp\left\{-i\pi \frac{x_b^2 + y_b^2}{f_2} \frac{z_f}{f_2}\right\} \exp\left\{-ik \frac{x_f x_b + y_f y_b}{f_2}\right\} dx_b\, dy_b \tag{3.3.5}$$

(x_f, y_f, z_f) is the coordinate placed on the focus of the objective. Since the tube lens and the objective are chromatic-aberration-corrected, the effective optical path lengths (phase terms) are the same for all wavenumbers k at the focal plane.

$$\exp\{i2k(f_1 + f_2)\} = const \tag{3.3.6}$$

To reconstruct the optical pulse, all the monochromatic waves delivered to focal plane of the objective are combined vectorially since they propagate along paths of different incident angles. Therefore, the temporal evolution of the field around focal plane can be shown as:

$$\vec{U}_5(x_f,y_f,z_f,t)=$$
$$c\int_{-\infty}^{+\infty}U_4(x_f,y_f,z_f,k)\left(\vec{x}_f\sin\beta'(k)+\vec{z}_f\cos\beta'(k)\right)W(k)\exp\left\{-i\left(kct-\phi(x_f,y_f,k)\right)\right\}dk$$
$$\text{where } \phi(x_f,y_f,k)=k\left(\frac{z_f}{\cos\beta'(k)}\left[1-\sin\alpha_0\cdot M\sin\beta'(k)\right]-\sin\alpha_0\cdot Mx_f\right) \tag{3.3.7}$$

$\beta'(k)$ is the incident angle for each k with respect to optical axis after objective, $\phi(x_f,y_f,k)$ is the pulse front delay which comes from diffraction grating, and $M = f_1/f_2$ is magnification with the lenses. Time-averaged intensity close to the focal plane can be expressed as:

$$I(x_f,y_f,z_f)=f_p\int_0^{1/f_p}\left|\vec{U}_5(x_f,y_f,z_f,t)\right|^2dt \tag{3.3.8}$$

f_p is repetition rate of the ultrafast pulsed laser. Since two-photon excitation is a nonlinear process, TPE efficiency is proportional to 2nd power of the intensity with TPE process.

$$I_{2p}(x_f,y_f,z_f)=I^2(x_f,y_f,z_f)=f_p\int_0^{1/f_p}\left|\vec{U}_5(x_f,y_f,z_f,t)\right|^4dt \tag{3.3.9}$$

where $I_{2p}(x_f,y_f,z_f)$ is TPE intensity. With axial intensity profiles obtained in eq. (3.3.9), axial optical resolution can be calculated.

3.4 DRWFI Design Optimization Based on Numerical Simulations

3.4.1. Selection of Key Design Parameters

In the previous section, a mathematical model was obtained with diffraction theory. Comparing the axial optical resolution for different instrument design parameters would allow us to quantify the ultimate DRWFI axial sectioning capability, and hence optimize instrument design. In this thesis, axial optical resolution is defined as FWHM of the axial intensity profile. To optimize DRWFI design, key design parameters that affect axial optical resolution are selected. First, the illumination FOV diameter (D_{FOV}) is chosen because we are interested in the effect of field size

on resolution. Furthermore, intuitively, large recombining angle of optical pulse waves at the focal plane enhances axial optical resolution. We select the parameters related to angular dispersion including: the groove frequency of the diffraction grating (G), the tube lens focal length (f_1), and the spectral bandwidth of the optical pulse ($FWHM_\lambda$). In addition, NA of the objective (NA) is clearly important in determining resolution.

3.4.2. Axial Optical Resolution Evaluation through Numerical Simulation

First, the effect of D_{FOV} on axial optical resolution was observed. Figure 3.3 shows the relationship between D_{FOV} and axial optical resolution. For large D_{FOV}, axial resolution remains constant and depends on other parameters such as G, f_1 and $FWHM_\lambda$ (f_1 and $FWHM_\lambda$ effects on D_{FOV} are not shown, but they are confirmed through numerical simulation.). However, axial resolution improves as D_{FOV} gets smaller. This is because very small D_{FOV} becomes equivalent to diffraction-limited focusing, and it is no longer wide-field illumination. In this thesis, only wide-field illumination is considered, so the following equation is valid.

$$FWHM_z(D_{FOV}) \sim const \tag{3.4.1}$$

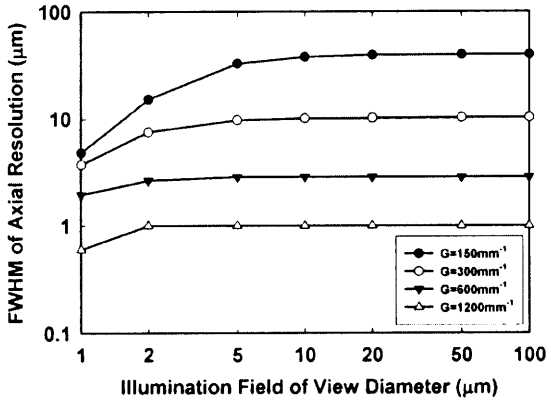

Figure 3.3 Axial optical resolution with different illumination FOV diameter

Next, axial optical resolution was observed to improve as G, f_1 and $FWHM_\lambda$ get larger as shown in figure 3.4. It can be intuitively explained that increasing G or $FWHM_\lambda$ results in greater angular dispersion and larger recombining angle for the optical pulses at the focal plane which lead to better axial optical resolution. In the case of f_1, it does not affect the angular

dispersion, but the separation between different wavelength components becomes large when f_1 is longer. This situation also results in improving axial optical resolution due to a large recombination angle. These effects are limited by the back aperture size of the objective. In figure 3.4(b), the axial optical resolution is very close to the diffraction limited (~0.75 μm) for the largest G (1200 grooves/mm). It does not quite approach diffraction limit because some of spectral components (far-red or far-blue edges of the ultrafast optical pulse) are clipped due to the finite size of back aperture of the objective that is determined by NA of the objective. Therefore, simulation results in the figure 3.4 were fitted to following equation. For the result in the figure 3.4(a),

$$FWHM_z(G, f_1) \sim \frac{A_1}{G^2 f_1^2} + B_1 \tag{3.4.2}$$

where A_1 and B_1 are proportional constants. For the result in the figure 3.4(b),

$$FWHM_z(G, FWHM_\lambda) \sim \frac{A_2}{G^2 FWHM_\lambda^2} + B_2 \tag{3.4.3}$$

where A_2 and B_2 are proportional constants. Each red dotted line indicates the best fit for each simulation result. B_1 and B_2 for the best fit are close to be 0.75 μm.

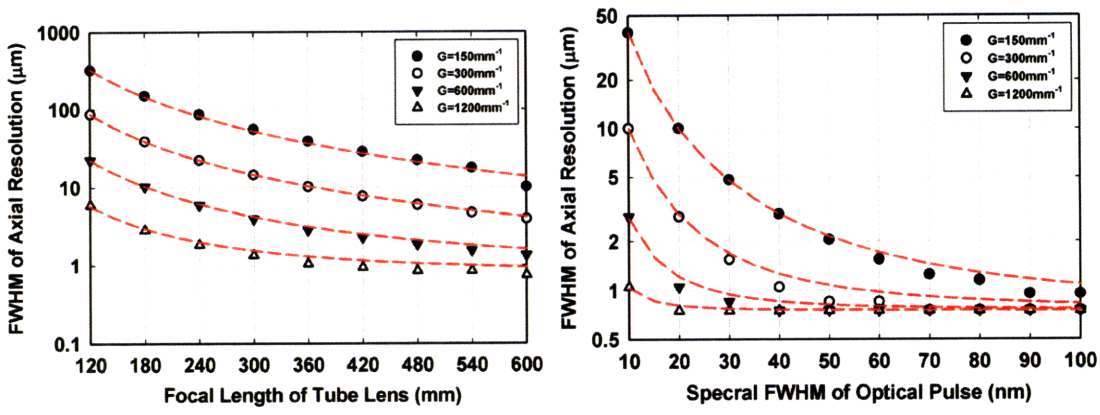

Figure 3.4 (a) Axial optical resolution with different tube lens focal length (b) Axial optical resolution with different optical pulse spectral width. Red dotted lines indicate the curve-fitting.

Lastly, the effects of NA were also investigated. Figure 3.5(a) shows G versus axial optical resolution. For small G, axial optical resolutions are very close to one another and are far from the diffraction-limited one. For larger G, is the dependence on NA can be approximated as:

$$\lim_{G\to\infty} FWHM_z(G,NA) \sim \frac{B_3}{NA} \tag{3.4.4}$$

where B_3 is proportional constant. Near the diffraction limit regime, optical axial resolution is inversely proportional to NA, and it is consistent with the result shown above. In addition, it is expected that $FWHM_z(G,NA)$ is proportional to λ since it is close to diffraction limit.

For different NA of the objective, the best axial optical resolutions in DRWFI were compared with the diffraction-limited axial optical resolutions in laser scanning microscopy as shown in figure 3.5(b). Their resolutions are very similar in the case of high NA objective, and the DRWFI resolution seems to be better than the TPE laser scanning one as NA becomes smaller. In this figure, only the FWHM of intensity profile was quantified. However, it should be noted that the intensity profile of DRWFI which has an approximate Lorentzian dependence has a much longer tail than that of the TPE laser scanning microscope. Figure 3.5(c) represents the modulation transfer function (MTF) for each system. The DRWFI has a narrower bandwidth for spatial frequency than the TPE laser scanning microscope; this confirms that the axial optical resolution in DRWFI is limited by diffraction.

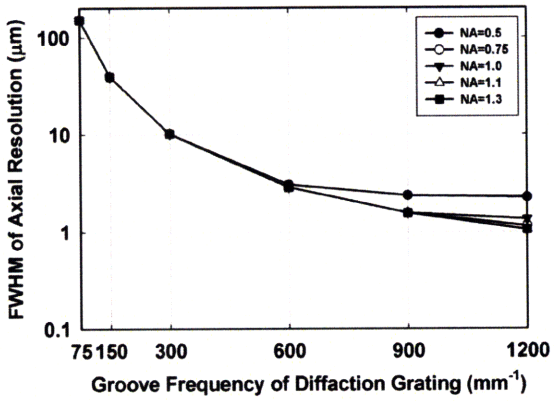

(a)

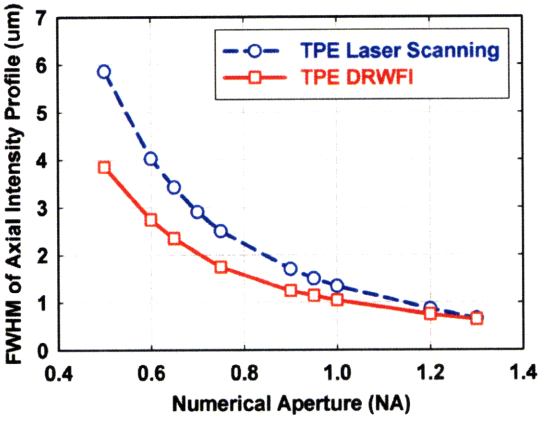

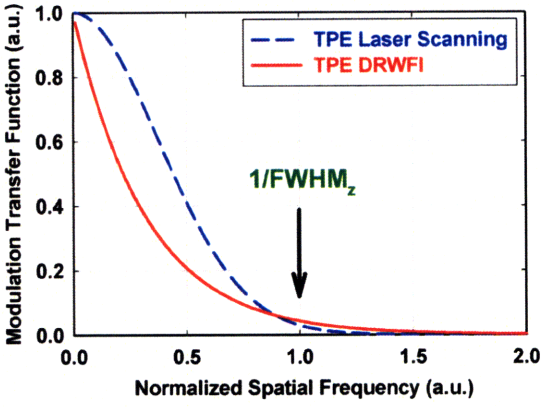

(b) (c)

Figure 3.5 (a) Axial optical resolution with respect to groove frequency of diffraction grating (b) Comparison of the best axial optical resolution in DRWFI and diffraction-limited axial resolution in TPE laser scanning microscope with different NA of the objective (c) MTF of DWRFI and TPE laser scanning microscopy. Assume that PSF for TPE laser scanning microscopy is Gaussian, and PSF for DRWFI is Lorentzian. Spatial frequency is normalized to the FWHM of axial optical resolution.

To summarize, D_{FOV} is irrelevant to the axial optical resolution as long as it is wide-field illumination. The distance between lateral focal points for the shortest and the longest wavelengths at the back aperture of the objective ($L_{\lambda_f-\lambda_i}$) mainly determines the axial optical

resolution, far from the diffraction limit. It is also controlled by G, f_1, and $FWHM_\lambda$ based on following relation:

$$L_{\lambda_f-\lambda_i} = f_1 \cdot \frac{d\beta}{d\lambda} \cdot FWHM_\lambda = f_1 \cdot G \cdot FWHM_\lambda \tag{3.4.5}$$

Near the diffraction limit, as $L_{\lambda_f-\lambda_i}$ goes near zero, the diffraction-limited optical resolution term becomes dominant in the axial optical resolution. Therefore, it is concluded that the axial optical resolution can be quantitatively expressed as below:

$$FWHM_z\left(D_{FOV}, G, FWHM_\lambda, f_1, NA\right) \propto \frac{A}{G^2 f_1^2 FWHM_\lambda^2} + B \cdot \frac{\lambda}{NA} \tag{3.4.6}$$

where A and B is proportional constants.

3.5 Two-Photon Excitation DRWFI Microscopy

In terms of instrument design, the TPE DRWFI microscopy has several advantages over the TPE laser scanning microscopy. Having no moving parts, it has excellent stability and low system cost. In addition, it offers the opportunity for extremely fast data acquisition with wide-field image acquisition. Figure 3.6 depicts the design of a TPE DRWFI microscopy.

This TPE DRWFI microscope was implemented after optimizing the design parameters through numerical simulations. All the design parameters were carefully chosen based on maximizing illumination power per voxel. Ultrafast optical pulses (center wavelength of 780 nm, pulse width of 100 fs, and repetition rate of 80 MHz) were delivered by a tunable Ti:Sapphire pulsed laser (Tsunami, Spectra-Physics, Mountain View, CA) pumped by CW DPSS laser (Millennia Xs, Spectra-Physics, Mountain View, CA). The beam diameter can be controlled with a beam expander. The FOV at the specimen is proportional to the beam diameter. At the surface of the reflective diffraction grating with the groove frequency of 600 grooves/mm (53004BK02-35IR, Richardson Grating Lab, Rochester, NY), ultrafast optical pulses are dispersed angularly, and the pulse profile is restored at the focal plane of the objective (Fluar, 403/1.30 Oil, Zeiss MicroImaging, Thornwood, NY) of an inverted microscope (Axiovert S100TV, Zeiss MicroImaging, Thornwood, NY). A NIR achromatic doublet (AC254-250-B, Throlabs, Newton,

NJ) is used as a tube lens to reduce chromatic aberration. The fluorescence on the specimen is collected through the objective in an epi-geometry. At the beam splitter (700dcxr, Chroma Technology, Rockingham, VT), the fluorescence is reflected and imaged by an intensified CCD (iCCD, PI-MAX, Princeton Instrument, Trenton, NJ). The specimen is placed on a stage that allows controlled lateral motion in the submicron range. The objective is positioned axially by a piezoelectric actuator (MIPOS500, Piezosystem jena Inc., Hopedale, MA) with a closed-loop controller (NV 40/1 CLE, Piezosystem jena Inc., Hopedale, MA). Actuating the objectives results in an axial translation of the focal plane in the specimen.

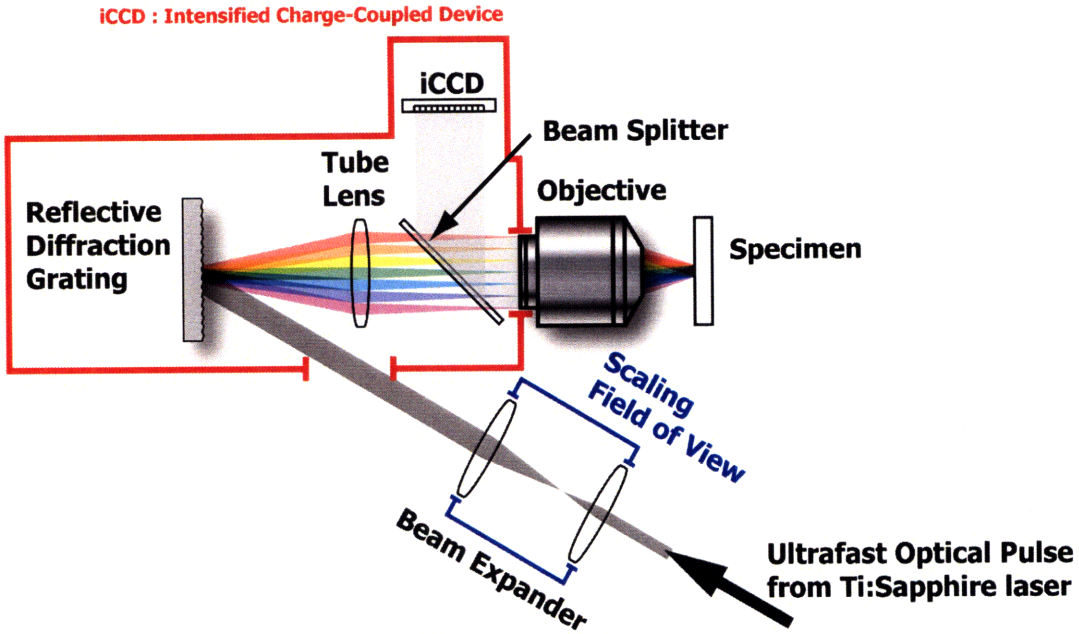

Figure 3.6. Schematic Diagram for TPE DRWFI Microscopy

3.6 Evaluation of Two-Photon DRWFI Microscopy

3.6.1 Two-Photon Excitation Efficiency

First, the TPE efficiency was measured to confirm that the excitation process is based on two-photon absorption. As a specimen, 300 μM fluorescein (46955, Sigma-Aldrich, St. Louis, MO) solution in deionized water was used. Power was measured before the grating, and the number of detected photons was counted by the iCCD. Figure 3.7 shows a measurement of fluorescence signal versus excitation intensity in a log-log plot. Curve-fitting shows a slope of 2 indicating

that fluorescence intensity is proportional to illumination intensity square, confirming TPE process.

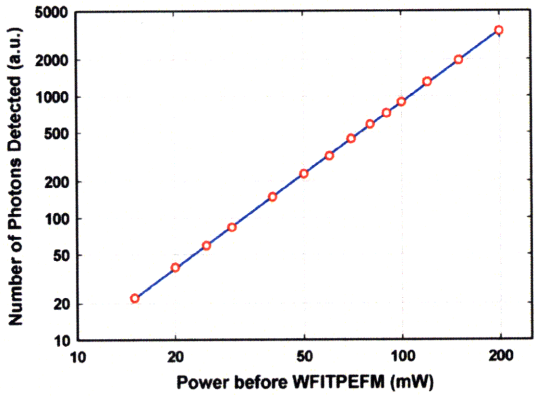

Figure 3.7. TPE efficiency for depth-resolved TPE DRWFI microscopy. Note that both x and y axes are in log scale. Red dot represents measured signal, and blue line is fitted curve with slope of 2.

3.6.2 Axial Optical Resolution

For measuring the axial optical resolution, 0.1 μm diameter yellow-green (505/515) fluorescent polystyrene microspheres (F-8803, Invitrogen, Carlsbad, CA) were used, each of which may be considered as a point source of light. Figure 3.8 shows the axial optical resolution in the simulation using the same design parameters as those of the experimental hardware and a comparison with experimental measurement. From figure 3.8, simulation result gives intensity profile FWHM of 1.60 μm. Measured intensity profile was fitted to Lorentzian function, and its FWHM was 1.65 μm. Measured resolution is very close to the simulated resolution. It confirms that the simulation results are well matched with the measurement and shows the potential to achieve diffraction-limit optical resolution practically with different design parameters.

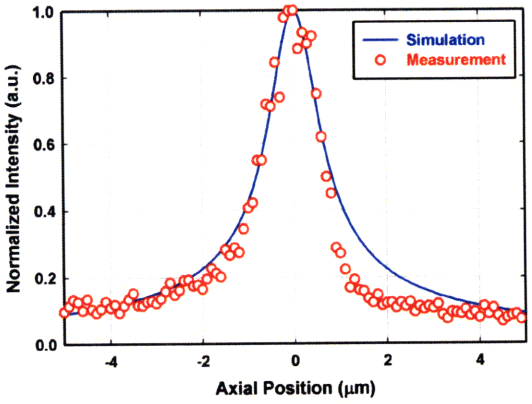

Figure 3.8 Axial intensity profile for 0.1 μm diameter microsphere. Experimental measurement and theoretical calculation are compared.

3.6.3 Single Particle Detection Sensitivity

As discussed at the beginning of this chapter, the use of high two-photon cross section probes may significantly improves the data acquisition speed of TPE DRWFI microscopy. One class of the most promising probes is the QD, a fluorescent semiconductor nanocrystal. The use of QDs for imaging has become popular in the past few decades because of a number of excellent optical properties [29]. As the surface-to-volume ratio of the material gets larger, the electronic energy states become discrete, and the quantum confinement effect becomes more dominant if metal and semiconductor particles are smaller than their exiton Bohr radii (1~5 nm) [30]. As a result of quantum confinement effect, QD has a quite broad absorption spectrum and a quite narrow symmetric emission spectrum controlled by its size [30] unlike conventional chromophores with broad red-tailed emission spectrum [31]. Figure 3.9 compares excitation and emission spectra for standard probe (Alexa568) and QD (QD605) and shows that they have similar emission peaks. The well-confined emission spectrum results in little crosstalk between the different size QDs during multi-color imaging. The surface of a bare QD has free unbounded electrons and crystal defects, and fluorescence quantum yield is reduced due to non-radiative electron energy transition on the surface. By adding a shell that consists of multiple layers of semiconductors to a bare QD, room temperature quantum yield and photostability are significantly improved, and toxicity can be alleviated [32]. It also provides resistance to photobleaching over longer period of time compared with conventional chromospheres.

QD blinking, as known as fluorescence intermittency [33], is observed at the single particle level. A single QD is observed to emit fluorescence for a finite time interval and then suddenly emit no fluorescence for a long period time. The QD blinking characteristic is affected by the illumination intensity and the number of the coated layers on the QD [33]. In addition, the probability density of "on" and "off" time period follows power-law statistics [34]. It is different from the permanent photobleaching since QD can resume emitting fluorescence after a very long time period of dark state [34]. This blinking phenomenon is undesirable in most cases as it interferes with continuous observation of the biomolecules in biological systems. However, it is sometimes useful for distinguishing single QDs from the aggregates.

QD has a broad range of applications in the fields of quantum computing [35], photovoltaic devices [36], and light emitting devices [37] as well as biology and medicine applications [31]. After the introduction of surface modified QD, it became possible to make water-soluble QD [38]. The water-soluble QD, which also has high two-photon cross-section [23], can be utilized in biological applications. Cells with bioconjugated QD have been labeled and imaged [38-40]. For the live cell, avidin-functionalized QD [41] or secondary antibody-conjugated QD [42] has been used since it is efficient to target QD at the cell membrane.

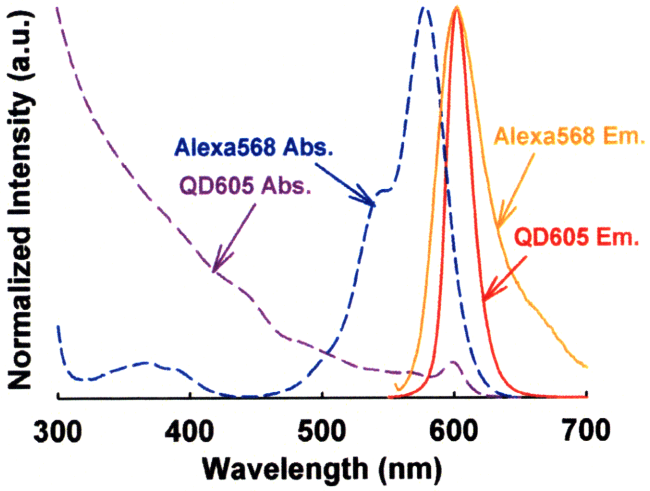

Figure 3.9 Absorption and emission spectrum for quantum dot and organic dye. QD605 is a quantum dot with peak emission of 605nm. Alexa568 is an organic dye with peak excitation of 568. 'Abs.' stands for absorption spectrum and 'Em.' indicates emission spectrum. Data is provided by Invitrogen Corporation.

We seek to demonstrate the sensitivity of the TPE DRWFI microscopy by imaging single QDs at the video rate. Two properties of QD, blinking and photobleaching, are very useful to validate the imaged object is a single QD. Blinking is only observed with the single QDs. Abrupt and complete photobleaching has been long used as a hallmark of imaging single fluorophores. To demonstrate the ability to detect a single QD with TPE DRWFI microscopy, single water-soluble streptavidin-conjugated QD with 585 nm emission peak (Q10111MP, Invitrogen, Carlsbad, CA) was imaged as a function of time. For specimen preparation, a similar protocol described in Hohng et al. [43] was used. Coverslip was etched with KOH to remove pre-existing chromophore. Narrow channel was made on the slide glass by inserting double-side adhesive tape between the slide glass and coverslip. 1 mg/mL biotinylated bovine serum albumin (BSA) (A8549-10MG, Sigma-Aldrich, St. Louis, MO) was added in TN buffer (10 mM Tris-HCl at pH7.4 and 50 mM NaCl), and this injected into the channel to treat the coverslip surface. Ten minutes after the incubation, the channel was washed twice with TN buffer. 1 μM QD was diluted at 1:100 with TN buffer, and this was injected into the channel, followed by 10-minute incubation. This leads to immobilizing the QD through biotin-spreptavidin interactions. Then, the channel was washed again twice with TN buffer, filled with TN buffer, and sealed with transparent nail polish (See figure 3.10 for sample preparation). The TPE DRWFI microscopy described in the previous section was used to image QDs.

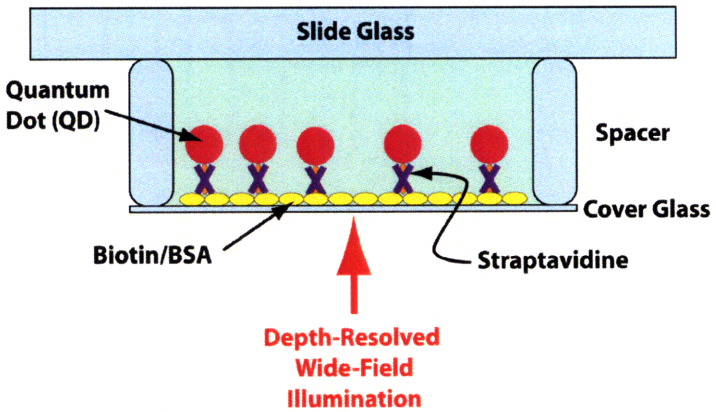

Figure 3.10 Pictorial diagram for QD-immobilized sample

For QD blinking measurement, the laser power used was 500 mW before the grating, and time-lapse images were taken every 100 milliseconds (10 fps) for 20 seconds. Figure 3.11(a)-(c) shows the time-lapse image for QD blinking at different times. QD blinking was identified, and no significant photobleaching was observed. Figure 3.11(d) represents the intensity temporal profile for the single QD in one of the regions of interest (ROIs). Intensity is fluctuating in time, indicating QD transitions between "on" and "off" states.

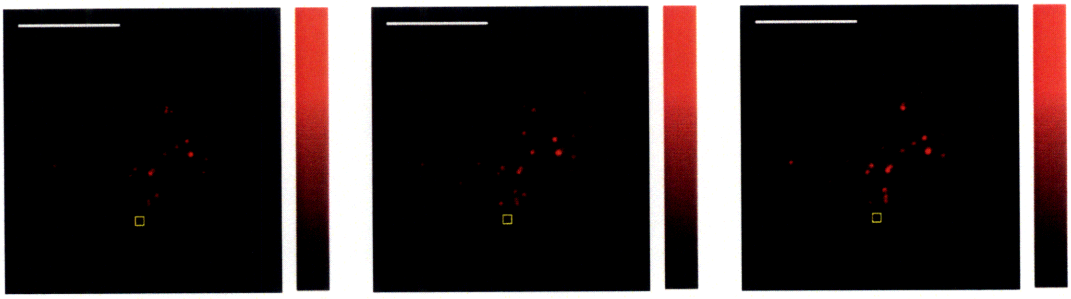

(a) (b) (c)

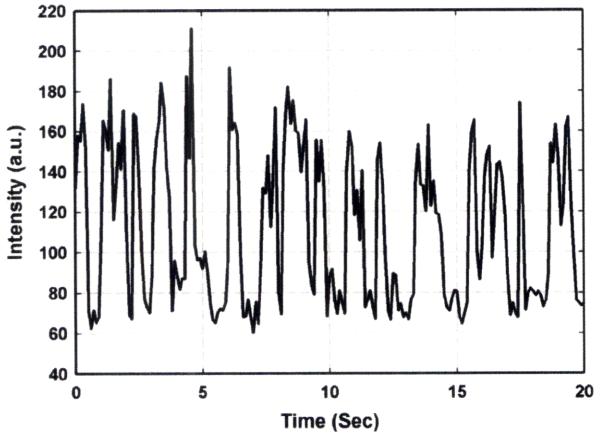

(d)

Figure 3.11 Single QD blinking imaging at (a) t=0 sec (b) t=10 sec and (c) t=20 sec. (Scale bar is 10 μm) (d) Temporal plot for single QD blinking (yellow boxes in (a)-(c))

For QD photobleaching measurement, higher laser power was needed and was set to 2 W. Figure 3.12(a)-(c) shows the time-lapse image of the photobleaching process. As seen in the figure, initially QDs were blinking, and some of QDs were no longer seen at the center of illumination due to photobleaching. The photobleaching process can be better observed from figure 3.12(d). Intensity was fluctuating for the first 4 seconds and suddenly went down to the background level. It is interpreted that QD blinking initially existed, but afterwards QD

permanently lost fluorescence capability. This observed object is a single QD because the intensity drop was a quantized process. Through QD blinking and photobleaching observation, it is concluded that the TPE DRWFI microscopy has the detection sensitivity for readily detecting a single QD at the video rate.

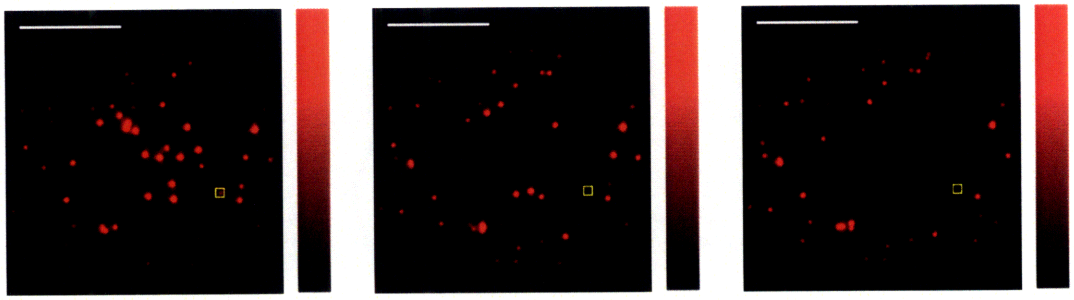

(a) (b) (c)

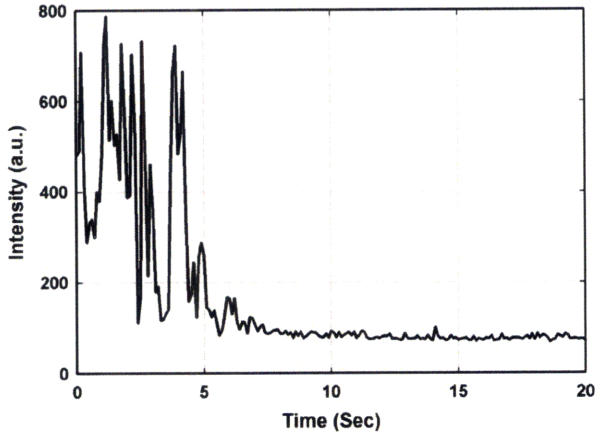

(d)

Figure 3.12 Single QD photobleaching imaging at (a) t=0 sec (b) t=10 sec and (c) t=20 sec. (Scale bar is 10 μm) (d) Temporal plot for single QD photobleaching process (yellow boxes in (a)-(c))

3.6.4 High-Speed Imaging Capability

QD-conjugated integrin-tagged fixed cell was used to show high-speed imaging capability. The following protocol was used: NIH 3T3 cells (CRL-1658, ATCC, Manassas, VA) were prepared and Dulbecco's modified eagle medium (DMEM) (30-2002, ATCC, Manassas, VA) was supplemented with 10% fetal bovine serum (FBS) (30-2021, ATCC, Manassas, VA) and penicillin-streptomycin (100 units of penicillin per mL media, and 100 μg streptomycin per mL

media; 30-2300, ATCC, Manassas, VA). Cells were cultured at 37 °C and 5% CO_2 in sterile condition. A day prior to the cell fixation, cells were incubated in glass bottom microwell dish (P35G-1.5-14-C, MatTek Co., Ashland, MA). Cells were washed three times for 30 seconds with 1X Dulbecco's phosphate buffered saline (DPBS) at pH 7.4 and were fixed with 4% paraformaldehyde in 1X DPBS for 15 minutes. Cells were washed again twice for 30 seconds with 1X DPBS at pH 7.4 and permeabilized with 0.2% Triton X-100 in 1X DPBS for 10 minutes. Then, cells were washed three times for 30 seconds with 1X DPBS at pH 7.4 and were blocked with 1% bovine serum albumin (BSA) (A8549-10MG, Sigma-Aldrich, St. Louis, MO) for an hour. 5 μL of 200 μg/mL anti-integrin α5 monoclonal antibody (sc-71419, Santa Cruz Biotechnology, Inc., Santa Cruz, CA) as a primary antibody was diluted at 1:100 in 1X DPBS with 1% BSA, and cells were incubated with it for an hour at room temperature on the shaker. Cells were washed three times for 5 minutes on the shaker with 1X DPBS at pH 7.4. 1 μM anti-mouse IgG-QD conjugate (Q11002MP, Invitrogen, Carlsbad, CA) as a secondary antibody was diluted at 1:00 with 1X DPBS with 1% BSA, and cells were incubated with it at room temperature for 45 minutes. Cells were washed twice for 30 seconds with 1X DPBS at pH 7.4 and mounted with mounting media (S36936, Invitrogen, Carlsbad, CA).

For high-speed imaging, the image sensor should be fast enough to transfer image information to the computer within exposure time. Due to the relatively slow full-frame readout time (~80 msec) of this iCCD, its maximum speed is at most 12 fps. To demonstrate the suitability of TPE DRWFI microscopy for higher speed imaging without a fast detector, we imaged QDs at much shorter exposure time by installing a fast mechanical shutter before the microscope. At the fastest setting, this mechanical shutter can provide a minimal opening time of 16 milliseconds that is equivalent to the exposure time for imaging at 60 fps. With laser power before the grating set to 1500 mW, figure 3.13 shows QD-tagged fixed cell imaged with a single 16 ms exposure. Most vesicles in the cell have SNR over 30, indicating that super-video rate imaging using TPE DRWFI microscopy is feasible with faster high sensitivity detectors. Therefore, it is demonstrated that the TPE DRWFI microscopy may be a powerful technique to study millisecond scale dynamic processes in cells using high two-photon cross section fluorophores such as QDs.

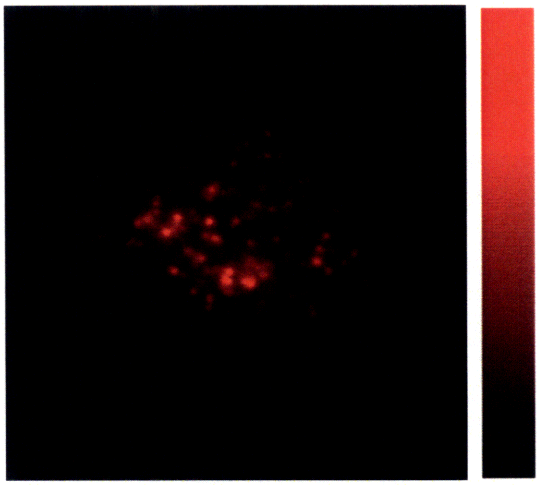

Figure 3.13 QD-tagged fixed cell imaged with 16 ms exposure time (equivalent to 60 fps imaging). The scale bar in the image is 10 μm.

3.7 Summary

In this chapter, DRWFI based on temporal focusing was introduced and its working principle was explained. A mathematical model was derived to identify the key design parameters for optimizing optical sectioning capability. Through numerical simulations, the effects on axial optical resolution with different design parameters were predicted, and the simplified relation between axial optical resolution and design parameters was estimated. Based on DRWFI, the TPE DRWFI microscopy was implemented. It was confirmed that the imaging in the TPE DRWFI microscopy is based on a TPE process. The theoretical calculation and experimental measurement for the axial optical resolution were well matched. In addition, single particle detection capability was demonstrated by observing the single QD blinking and photobleaching. Lastly, high-speed capability was confirmed by imaging QD-labeled fixed cells at a frame speed that is equivalent to super-video rate.

References

1. J. B. Pawley, *Handbook of biological confocal microscopy* (Springer, New York, NY, 2006).
2. W. Denk, J. H. Strickler, and W. W. Webb, "Two-Photon Laser Scanning Fluorescence Microscopy," Science **248**, 73-76 (1990).
3. P. T. C. So, C. Y. Dong, B. R. Masters, and K. M. Berland, "Two-photon excitation fluorescence microscopy," Annual Review of Biomedical Engineering **2**, 399-429 (2000).

4. C. L. Evans, and X. S. Xie, "Coherent Anti-Stokes Raman Scattering Microscopy: Chemical Imaging for Biology and Medicine," Annual Review of Analytical Chemistry **1**, 883-909 (2008).
5. D. Oron, E. Tal, and Y. Silberberg, "Scanningless depth-resolved microscopy," Optics Express **13**, 1468-1476 (2005).
6. G. H. Zhu, J. van Howe, M. Durst, W. Zipfel, and C. Xu, "Simultaneous spatial and temporal focusing of femtosecond pulses," Optics Express **13**, 2153-2159 (2005).
7. M. Petr¡, M. Hadravsk›, M. D. Egger, and R. Galambos, "Tandem-Scanning Reflected-Light Microscope," J. Opt. Soc. Am. **58**, 661-664 (1968).
8. M. Petran, M. Hadravsky, and A. Boyde, "The Tandem Scanning Reflected Light-Microscope," Scanning **7**, 97-108 (1985).
9. J. Bewersdorf, R. Pick, and S. W. Hell, "Multifocal multiphoton microscopy," Optics Letters **23**, 655-657 (1998).
10. A. H. Buist, M. Muller, J. Squier, and G. J. Brakenhoff, "Real time two-photon absorption microscopy using multi point excitation," Journal of Microscopy-Oxford **192**, 217-226 (1998).
11. L. Sacconi, E. Froner, R. Antolini, M. R. Taghizadeh, A. Choudhury, and F. S. Pavone, "Multiphoton multifocal microscopy exploiting a diffractive optical element," Optics Letters **28**, 1918-1920 (2003).
12. T. Nielsen, M. Frick, D. Hellweg, and P. Andresen, "High efficiency beam splitter for multifocal multiphoton microscopy," Journal of Microscopy-Oxford **201**, 368-376 (2001).
13. J. M. Squirrell, D. L. Wokosin, J. G. White, and B. D. Bavister, "Long-term two-photon fluorescence imaging of mammalian embryos without compromising viability," Nature Biotechnology **17**, 763-767 (1999).
14. P. T. C. So, H. Kim, and I. E. Kochevar, "Two-photon deep tissue ex vivo imaging of mouse dermal and subcutaneous structures," Optics Express **3**, 339-350 (1998).
15. P. T. C. So, C. Buehler, K. H. Kim, C. Y. Dong, and B. R. Masters, "Two photon imaging of skin structures," Scanning **21**, 135-135 (1999).
16. J. H. Strickler, and W. W. Webb, "3-Dimensional Optical-Data Storage in Refractive Media by 2-Photon Point Excitation," Optics Letters **16**, 1780-1782 (1991).
17. D. Yang, S. J. Jhaveri, and C. K. Ober, "Three-dimensional microfabrication by two-photon lithography," Mrs Bulletin **30**, 976-982 (2005).
18. S. Maruo, and J. T. Fourkas, "Recent progress in multiphoton microfabrication," Laser & Photonics Reviews **2**, 100-111 (2008).
19. M. J. Rust, M. Bates, and X. W. Zhuang, "Sub-diffraction-limit imaging by stochastic optical reconstruction microscopy (STORM)," Nature Methods **3**, 793-795 (2006).
20. B. Huang, S. A. Jones, B. Brandenburg, and X. W. Zhuang, "Whole-cell 3D STORM reveals interactions between cellular structures with nanometer-scale resolution," Nature Methods **5**, 1047-1052 (2008).
21. E. Betzig, G. H. Patterson, R. Sougrat, O. W. Lindwasser, S. Olenych, J. S. Bonifacino, M. W. Davidson, J. Lippincott-Schwartz, and H. F. Hess, "Imaging intracellular fluorescent proteins at nanometer resolution," Science **313**, 1642-1645 (2006).
22. A. Vaziri, J. Y. Tang, H. Shroff, and C. V. Shank, "Multilayer three-dimensional super resolution imaging of thick biological samples," Proceedings of the National Academy of Sciences of the United States of America **105**, 20221-20226 (2008).

23. D. R. Larson, W. R. Zipfel, R. M. Williams, S. W. Clark, M. P. Bruchez, F. W. Wise, and W. W. Webb, "Water-soluble quantum dots for multiphoton fluorescence imaging in vivo," Science **300**, 1434-1436 (2003).
24. T. Wilson, and C. Sheppard, *Theory and practice of scanning optical microscopy* (Academic Press, London ; Orlando, 1984).
25. M. Gu, *Principles of three dimensional imaging in confocal microscopes* (World Scientific, Singapore ; River Edge, NJ, 1996).
26. M. Born, E. Wolf, and A. B. Bhatia, *Principles of optics : electromagnetic theory of propagation, interference and diffraction of light* (Cambridge University Press, Cambridge [England] ; New York, 1999).
27. E. Hecht, *Optics* (Addison-Wesley, Reading, Mass., 2002).
28. C. Palmer, *Diffraction Grating Handbook* (Newport, 2005).
29. M. G. Bawendi, M. L. Steigerwald, and L. E. Brus, "The Quantum-Mechanics of Larger Semiconductor Clusters (Quantum Dots)," Annual Review of Physical Chemistry **41**, 477-496 (1990).
30. A. P. Alivisatos, "Semiconductor clusters, nanocrystals, and quantum dots," Science **271**, 933-937 (1996).
31. X. Michalet, F. F. Pinaud, L. A. Bentolila, J. M. Tsay, S. Doose, J. J. Li, G. Sundaresan, A. M. Wu, S. S. Gambhir, and S. Weiss, "Quantum Dots for Live Cells, in Vivo Imaging, and Diagnostics," Science **307**, 538-544 (2005).
32. V. Biju, T. Itoh, A. Anas, A. Sujith, and M. Ishikawa, "Semiconductor quantum dots and metal nanoparticles: syntheses, optical properties, and biological applications," Analytical and Bioanalytical Chemistry **391**, 2469-2495 (2008).
33. M. Nirmal, B. O. Dabbousi, M. G. Bawendi, J. J. Macklin, J. K. Trautman, T. D. Harris, and L. E. Brus, "Fluorescence intermittency in single cadmium selenide nanocrystals," Nature **383**, 802-804 (1996).
34. P. Frantsuzov, M. Kuno, B. Janko, and R. A. Marcus, "Universal emission intermittency in quantum dots, nanorods and nanowires," Nature Physics **4**, 519-522 (2008).
35. D. Loss, and D. P. DiVincenzo, "Quantum computation with quantum dots," Physical Review A **57**, 120-126 (1998).
36. J. M. Luther, M. Law, M. C. Beard, Q. Song, M. O. Reese, R. J. Ellingson, and A. J. Nozik, "Schottky Solar Cells Based on Colloidal Nanocrystal Films," Nano Letters **8**, 3488-3492 (2008).
37. M. J. Bowers, J. R. McBride, and S. J. Rosenthal, "White-Light Emission from Magic-Sized Cadmium Selenide Nanocrystals," Journal of the American Chemical Society **127**, 15378-15379 (2005).
38. M. Bruchez, M. Moronne, P. Gin, S. Weiss, and A. P. Alivisatos, "Semiconductor nanocrystals as fluorescent biological labels," Science **281**, 2013-2016 (1998).
39. W. C. W. Chan, and S. M. Nie, "Quantum dot bioconjugates for ultrasensitive nonisotopic detection," Science **281**, 2016-2018 (1998).
40. X. Y. Wu, H. J. Liu, J. Q. Liu, K. N. Haley, J. A. Treadway, J. P. Larson, N. F. Ge, F. Peale, and M. P. Bruchez, "Immunofluorescent labeling of cancer marker Her2 and other cellular targets with semiconductor quantum dots (vol 21, pg 41, 2003)," Nature Biotechnology **21**, 452-452 (2003).

41. M. Dahan, S. Levi, C. Luccardini, P. Rostaing, B. Riveau, and A. Triller, "Diffusion dynamics of glycine receptors revealed by single-quantum dot tracking," Science **302**, 442-445 (2003).
42. J. O. Winter, T. Y. Liu, B. A. Korgel, and C. E. Schmidt, "Recognition molecule directed interfacing between semiconductor quantum dots and nerve cells," Advanced Materials **13**, 1673-1677 (2001).
43. S. Hohng, and T. Ha, "Near-complete suppression of quantum dot blinking in ambient conditions," Journal of the American Chemical Society **126**, 1324-1325 (2004).

Chapter 4

DRWFI Applications: I. Live Cellular Imaging with Quantum Dots

4.1 Introduction

In previous chapter, TPE DRWFI microscopy was introduced and its capabilities for diffraction-limited optical sectioning, high sensitivity detection, and high-speed imaging were demonstrated. Two-photon microscopy has several advantages over the conventional confocal microscopy in that it leads to less photodamage, slower photobleaching and higher cell viability during cellular imaging. Compared with the wide-field microscopy, its imaging speed is ultimately slow due to the need for a sequential scanning. The use of TPE DRWFI microscopy improves the imaging speed to a level comparable to that of the wide-field imaging, enabling cellular processes to be observed at video-rate with 3D resolution. The use of photobleaching resistant and high two-photon cross section contrast agents such as QDs, further allows cellular imaging with high sensitivity. Therefore, TPE DRWFI microscopy has many potential applications in cellular studies, one of which is single particle tracking (SPT). SPT is a very useful technique for studying a variety of transport processes in cells such as receptor diffusion inside lipid rafts [1], cargo transport along microtubule [2], and viral transport in cells [3, 4]. The possibility of high frame rate and high sensitivity imaging of TPE DRWFI microscopy is critical for SPT to follow the relevant dynamics of transporting molecules in cells. More importantly, there are only a few other SPT techniques with 3D capability similar to TPE DRWFI microscopy-based SPT [5-7]. Another potential application of TPE DRWFI microscopy is image correlation spectroscopy (ICS) or image cross-correlation spectroscopy (ICCS). ICS is a powerful method to obtain spatial and temporal correlations of molecular concentration by acquiring a sequence of cellular images allowing aggregation and transport of molecules to be studied. Since the sensitivity of the correlation spectroscopy is inversely proportional to the molecular number, depth discriminated

imaging is critical to reduce the observation volume and the number of molecules contained within. Depth discriminated images for ICS have been taken using confocal microscopy [8], TPM [9], or total internal reflection fluorescence microscopy (TIRFM). With TIRFM and laser scanning microscopy, there is a trade-off between depth selectivity and imaging speed. TIRFM microscopy is wide-field imaging method providing excellent temporal resolution, but can image only a few hundred microns above the cover glass due to the limited penetration depth of the evanescent wave. Laser scanning microscopy can image at any depth within the cell, but it is relatively slow due to sequential scanning. TPE DRWFI microscopy has the advantage of having both excellent imaging speed and depth selectivity. Furthermore, the approach based on TPE DRWFI microscopy allows the extension of ICS to 3D.

In this chapter, novel SPT and ICS approaches based on TPE DRWFI microscopy are applied to live cellular imaging applications: SPT and ICS are demonstrated in living cells. First, live cellular imaging capability is evaluated with embedding QD in the cell. Then, QD-conjugated antibody is conjugated to integrin $\alpha 5$, an important transmembrane protein, and its dynamics in live cell are observed through image analysis including SPT and ICS.

4.2 Theoretical Background

4.2.1 Single Particle Tracking

SPT [10] is a very powerful method to study molecular transport and trafficking processes in biological systems. By monitoring the motion of single molecules with nanometer scale resolution, their trajectories can be analyzed to reveal the mechanisms driving motions of these molecules. For example, in the study of membrane biophysics, normal diffusion is not observed; instead, the presence of local protein domains and lipid rafts results in the observation of anomalous [11, 12] and confined [13, 14] diffusion on the cell membrane. In addition, directed motions driven by molecular motors [15, 16] are observed. A powerful method to quantify particle trajectory is to compute the mean square displacement (MSD) defined as:

$$MSD(\tau) = \left\langle \left| r(t+\tau) - r(t) \right|^2 \right\rangle \qquad (4.2.1)$$

where τ is temporal lag, $r(t)$ is 2D position for single particle, and $\langle \bullet \rangle$ is temporal average. For normal diffusion, the MSD is linearly proportion to time:

$$MSD(\tau) = 4D\tau \tag{4.2.2}$$

where D is diffusion coefficient. In the case of anomalous diffusion, eq. (4.2.2) is modified as:

$$MSD(\tau) \sim \tau^{\alpha} \tag{4.2.3}$$

where α is constant characterizing the power law dependence [17]. If $\alpha > 1$, it is considered to be superdiffusion indicating the presence of flow or active cellular transport mechanisms [18]. If $\alpha < 1$, it is called subdiffusion, resulting from diffusion within a molecular "cage". For example, subdiffusion is observed due to macromolecular crowding in the cytoplasm [19], or due to the presence of protein domains in the cell membrane. In addition, the MSD in the presence of both diffusion and directed motion or flow is expressed as:

$$MSD(\tau) = 4D\tau + v_f t^2 \tag{4.2.4}$$

4.2.2 Image Correlation Spectroscopy

Protein aggregation and association regulates a complex array of cellular processes such as migration and proliferation. The resolution of the optical microscopy is limited by diffraction to about 250 nm, and thus individual protein molecules cannot be identified. However, protein association and aggregation can be detected by optical methods such as autocorrelation spectroscopy. Fluorescence correlation spectroscopy (FCS), which was developed several decades ago [20-22], measures the aggregation of labeled proteins in solutions by quantifying their number density based on Poissonian intensity fluctuation of light in time. This technique was extended to study receptor aggregation processes in cell membranes, resulting in the development of ICS and ICCS [8, 23]. In ICS, the molecules of interest are either labeled with endogenous chromophores such as green fluorescence proteins (GFPs) or exogenous chromophores. A 2D image is acquired and analyzed by quantifying the spatial fluctuation of light intensity of the labeled proteins. If a sequence of time-lapse images is acquired, spatio-temporal correlation analysis can be performed to study both aggregation and diffusion of proteins. Figure 4.1 describes pictorially the procedure for ICS analysis.

In this thesis, we focus on autocorrelation while it is straightforward to extend this methodology to cross-correlation analysis. Generalized spatio-temporal autocorrelation $g(\xi,\eta,\tau)$ is defined as a function of spatial lag (ξ,η) and temporal lag τ, and by the following expression [9]:

$$g(\xi,\eta,\tau)=\frac{\langle \delta I(x,y,t)\cdot \delta I(x+\xi,y+\eta,t+\tau)\rangle}{\langle I(x,y,t)\rangle\cdot\langle I(x,y,t+\tau)\rangle} \tag{4.2.5}$$

where $\delta I(x,y,t)=I(x,y,t)-\langle I(x,y,t)\rangle$, $I(x,y,t)$ is the intensity in given location at time t from the image, and $\langle\bullet\rangle$ represents the spatial average. If the temporal evolution of molecular distribution is ignored or is slow, the temporal correlation can be ignored and eq. (4.2.5) can be modified as below [8]:

$$g(\xi,\eta,0)=g(0,0,0)e^{-\frac{\xi^2+\eta^2}{\omega_0^2}}+g_0 \tag{4.2.6}$$

where ω_0 is $1/e^2$ radius of laser beam and g_0 is baseline or DC component. The number of particles can be estimated with $g(0,0,0)$ and ω_0.

$$N=\frac{A_{img}}{g(0,0,0)\pi\omega_0^2} \tag{4.2.7}$$

where A_{img} is the imaging area. When intensity distribution is evolving temporally, temporal correlation should also be included. Following equations describe the autocorrelation function for diffusion (4.2.8) and for diffusion with flow (4.2.9) in a 2D system [24].

$$g(0,0,\tau)=g(0,0,0)\left(1+\frac{\tau}{\tau_d}\right)^{-1}+g_1 \tag{4.2.8}$$

$$g(0,0,\tau)=g(0,0,0)\left(1+\frac{\tau}{\tau_d}\right)^{-1}\cdot e^{\left(\frac{\tau}{\tau_f}\right)^2\left(1+\frac{\tau}{\tau_d}\right)^{-1}}+g_2 \tag{4.2.9}$$

where τ_d is characteristic diffusion time, τ_f is characteristic flow time, and g_1, g_2 are baseline parameters.

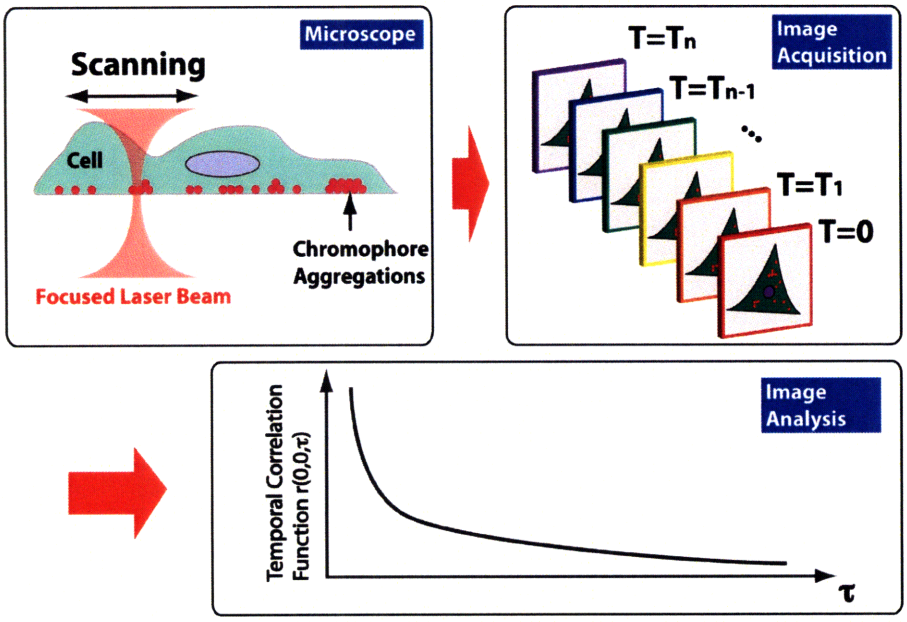

Figure 4.1 General procedure for ICS. In microscope inset, only laser scanning microscope is shown. In image analysis, only temporal autocorrelation function analysis is depicted.

4.3 Observation of Quantum Dot Conjugated Protein Dynamics in Live Cell

4.3.1 Live Cell Imaging with Non-Targeted Quantum Dot

We demonstrate that live cell labeled non-specifically with QD can be imaged with TPE DRWFI microscopy. The sample was prepared via following protocol: NIH 3T3 cell was purchased from American Type Culture Collection (CRL-1658, ATCC, Manassas, VA), and DMEM (30-2002, ATCC, Manassas, VA) was supplemented with 10% FBS (30-2021, ATCC, Manassas, VA) and penicillin-streptomycin (100 units of penicillin per mL media, and 100 µg streptomycin per mL media; 30-2300, ATCC, Manassas, VA). Cells were cultured in DMEM at 37 °C and 5% CO_2 in sterile condition. A day or two prior to imaging, cells were incubated in glass bottom microwell dish (P35G-1.5-14-C, MatTek Co., Ashland, MA). After checking ~70% confluency in the dish, cells were washed three times for 30 seconds with 1X DPBS (21-031-CV, Mediatech Inc., Herndon, VA) at pH 7.4. 1 µM streptavidin-conjugated QD (Q10111MP, Invitrogen, Carlsbad, CA) was diluted with DMEM at 1:100 ratio and then added to the dish. Two hours after embedding QDs in the cells, cells were washed three times for 30 seconds with 1X DPBS at pH

7.4 and DMEM was added to cells to keep them alive during imaging. The QDs were not targeted to specific receptors. Figure 4.2 depicts live cell sample prepared with above protocol.

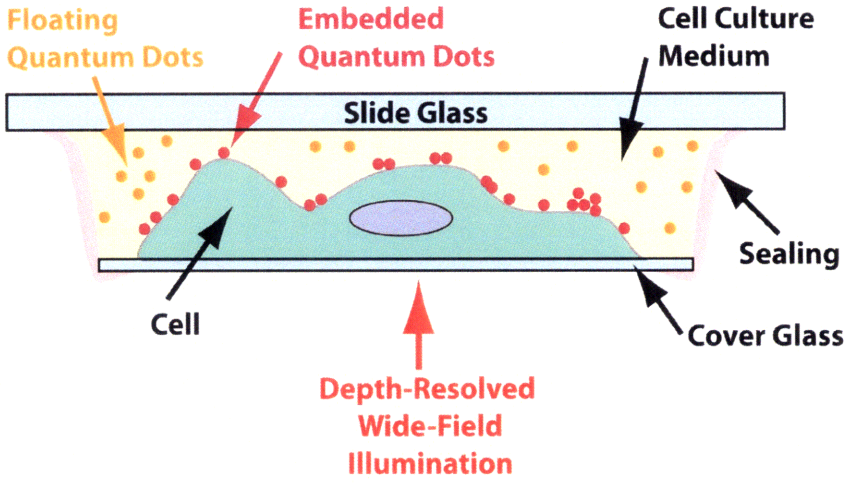

Figure 4.2 Schematic diagram for QD binding non-specifically live cell

Live cell images were obtained by DRWFI using the instrument described in Chapter 3. A high NA objective (Fluar, 40X / 1.30 Oil Immersion, Carl Zeiss MicroImaging Inc., Thornwood, NY) is used and the images were acquired by an iCCD (PI-MAX, Princeton Instrument, Trenton, NJ). 201 images were acquired continuously with exposure time of 100 msec. Illumination laser power was 500 mW before the grating. Figure 4.3 shows a time lapse sequence of images. Most of QDs were non-specifically bound to the cell membrane while a fraction of the QD is endocytosed. Blinking behavior is observed at some locations, indicating that DRWFI has sufficient sensitivity to observed single QD at video rate on living cells.

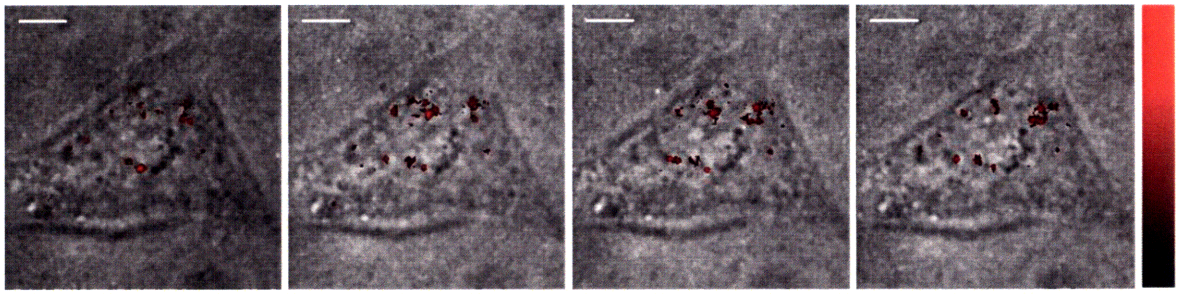

(a) **(b)** **(c)** **(d)**

Figure 4.3 Live cellular imaging with embedded QD: each image was taken at (a) 0 sec (b) 5 sec (c) 10 sec (d) 15 sec. Scale bar is 5 μm.

4.3.2 Live Cell Imaging with Quantum Dot Conjugated Integrin

QDs were conjugated to integrins to study receptor dynamics on the cell membrane. The protocol used is similar to section 4.2 unless otherwise stated. NIH 3T3 cells were incubated in glass bottom microwell dish a day or two before sample preparation. After attaining ~70% confluency, cells were washed three times for 30 seconds with 1X DPBS at pH 7.4. 50 µL of 200 µg/mL anti-integrin α5 monoclonal antibody (sc-71419, Santa Cruz Biotechnology, Inc., Santa Cruz, CA), as a primary antibody, was added at 10 µg/mL in DMEM and cells were incubated for 30 minutes at 37 °C. Cells were then washed again three times for 30 seconds with 1X DPBS at pH 7.4. 1 µM anti-mouse IgG-QD conjugate (Q11002MP, Invitrogen, Carlsbad, CA) as a secondary antibody was diluted to 1:100 with DMEM, and the solution was added to cell to fill imaging chamber (~0.25 mL/chamber). Cells were incubated for 30 minutes at 4 °C then washed three times for 30 seconds with 1X DPBS at pH 7.4. Dish was filled with DMEM during the imaging. Figure 4.4 represents the schematic diagram for live cell with QD-tagged integrin α5 antibodies. Time-lapse images were obtained every 100 milliseconds for 20 seconds. Optical power was 500 mW before the grating.

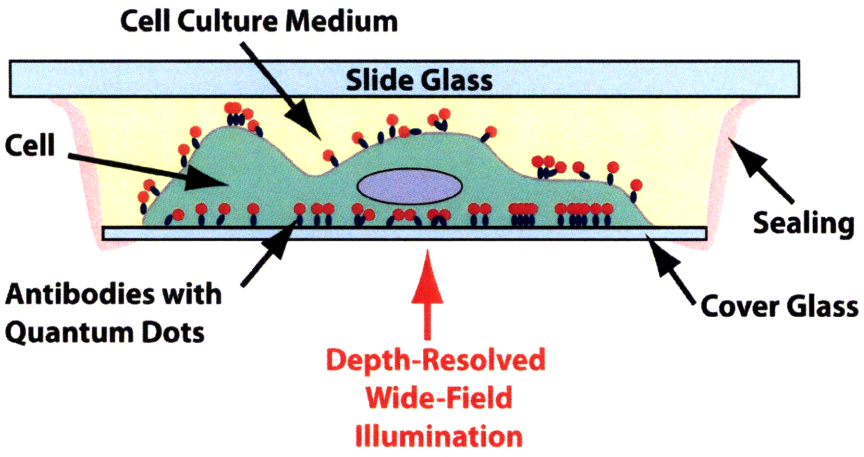

Figure 4.4 Schematic diagram for cell preparation with anti-integrin α5 antibodies and anti-mouse IgG-QD conjugates.

4.3.3 Single Particle Tracking

Prior to SPT for QD in live cell, the mechanical stability of TPE DRWFI microscopy apparatus was quantified by imaging stationary particles [10]. As a specimen, QDs were attached to BSA on the cover glass as described in Chapter 3. Time-lapse images were acquired for 20 seconds at the interval of 100 milliseconds. Figure 4.5 shows the MSD of the stationary particle. In this figure, MSD remains constant as a function of time indicating a lack or diffusion or flow as expected. We further observed a MSD noise floor of 0.02 μm^2, which originates from the quantization noise and photon shot noise (SNR=10). It is demonstrated that TPE DRWFI microscopy was mechanically stable.

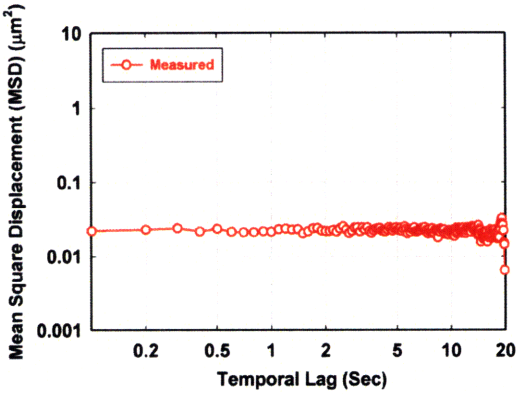

Figure 4.5 Single particle tracking for immobilized QD attached to BSA on the cover glass.

The particle tracking algorithm written in MATLAB 2008a (The Mathworks, Natick, MA) was used to analyze the trajectory of the single QD tagged to integrin α5. A bright-field image is overlaid on the fluorescence image at different time-point imaging time as shown in figure 4.6(a). At t=15 sec, the particle seemed to disappear due to QD blinking but emitted signal again later. MSD of its trajectory was computed and plotted in figure 4.6(b). The MSD shows two temporal regimes with different power law dependence. The MSD data were fitted using nonlinear least square optimization in MATLAB optimization toolbox. Power law coefficient α was estimated in two different time regimes. For 0.1 – 1.3 seconds, subdiffusion ($\alpha = 0.409$) behavior is shown, whereas superdiffusion ($\alpha = 1.790$) is dominant in 1.3 – 20 seconds. Based on the observation, it is shown that the particle is undergoing active transport in the longer time scale and confined motion in the shorter time scale. To calculate diffusion coefficient and flow

velocity, MSD was fitted to eq. (4.2.4). Diffusion coefficient was 7.7×10^{-11} cm^2/sec, and flow velocity was 0.29 μm/min; they are on the same order of magnitude as published results [24-26].

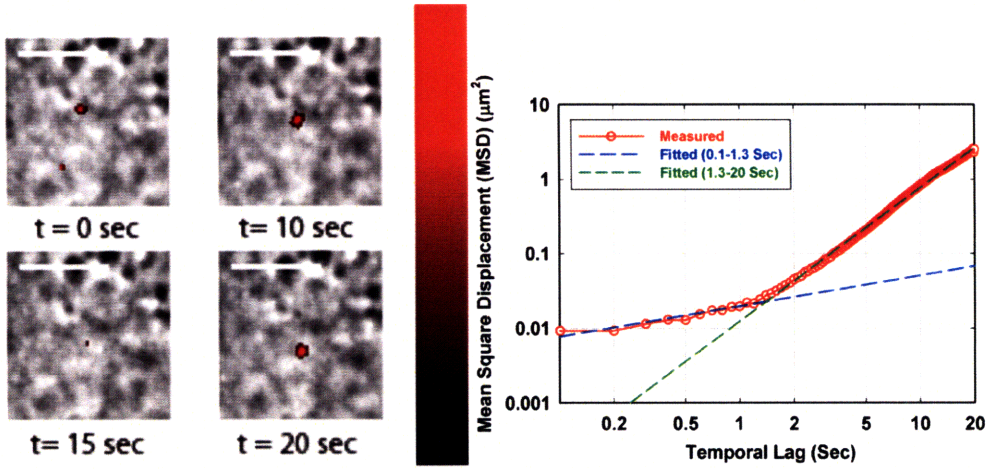

(a) **(b)**

Figure 4.6 Single particle tracking for a diffusing QD in the living cell: (a) Fluorescent images are overlaid with bright-field images at different time scale (scale bar: 5μm) (b) MSD vs. time. It was fitted at different time scales.

4.3.4 Image Correlation Spectroscopy

Figure 4.7(a) shows a fluorescence image overlaid by a bright-field image. In an expanded view, figure 4.7(b), several QD particles (N=5) are seen to be attached to cell membrane. We used this image to test the capability of ICS to quantify particle number. All the images were analyzed by using customized MATLAB codes. With a time-lapse image sequence, spatial autocorrelation $g(\xi,\eta,0)$ was calculated at each time point (See figure 4.8(a)). $g(0,\eta,0)$ was fitted to a Gaussian function expressed in eq. (4.2.6) to estimate $g(0,0,0)$. Measuring $g(0,0,0)$ allows us to quantify the number of particles in the image via eq. (4.2.7). The number of particles is estimated to be 3.56, which is not accurate compared to the actual number.

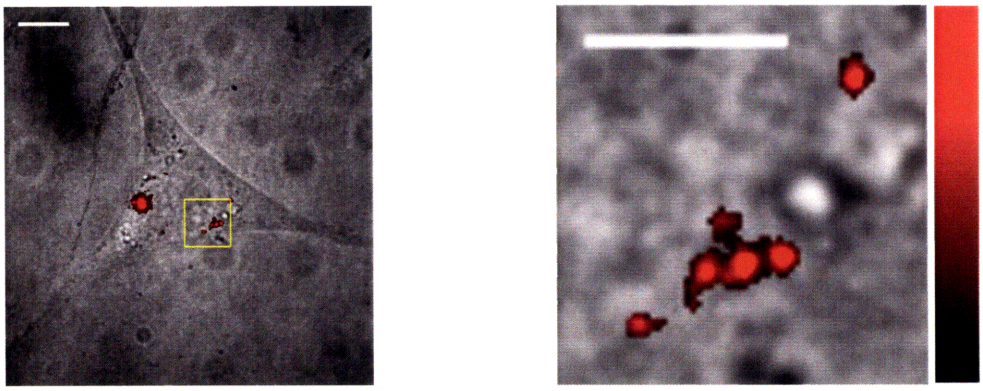

(a) **(b)**

Figure 4.7 QD distribution in the cell: (a) overlaid image with bright field and fluorescence and (b) zoomed-in image from the rectangle in (a). Scale bar is (a) 10 μm and (b) 5 μm.

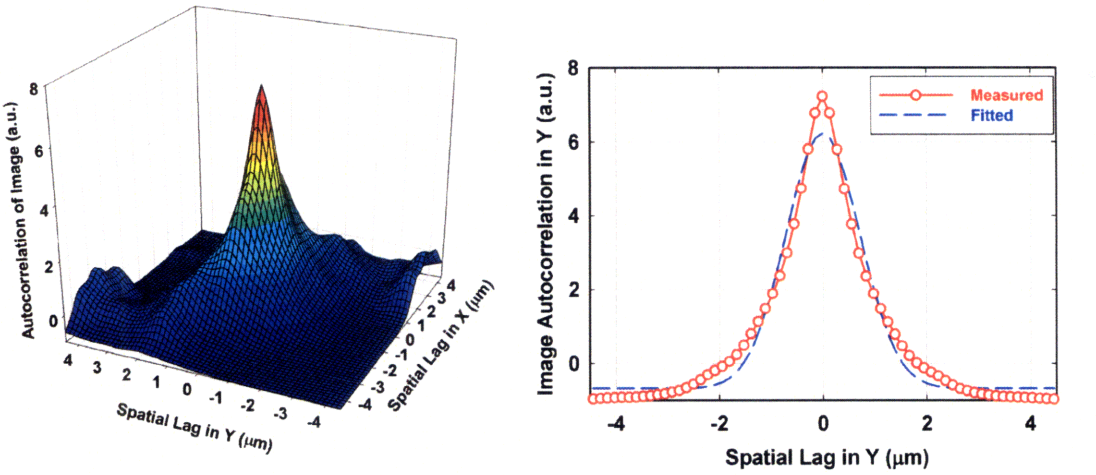

(a) **(b)**

Figure 4.8 (a) Spatial image autocorrelation $g(\xi,\eta,0)$ (b) Spatial image autocorrelation along y axis $g(0,\eta,0)$: It was fitted to Gaussian function.

There are two main factors affecting the accuracy of particle number estimation. The first one is QD blinking effect. Unlike single particle tracking, ICS is more sensitive to the blinking and results in losing accuracy for estimating the number of particles in the area where image is analyzed. For example, one of the key procedures is to correctly estimate ω_0, but it is not easy due to QD blinking. A calibration procedure with the fluorescent microsphere is needed. The second one is the total number of particles involved in ICS. Since ICS is a statistical analysis

method, at least 50 particles, as a rule of thumb, should be included to provide statistically meaningful results. However, only 5 particles were involved in this analysis due to the difficulty of sample preparation, and further analysis involving more particles is needed. Despite relatively low accuracy, the order of magnitude of the number of particles is close to the actual number. In figure 4.9, the change of the number of particles is plotted against time. Due to the cell membrane mobility, the number of particles was not constant in time, and this fluctuation range is similar to the actual number.

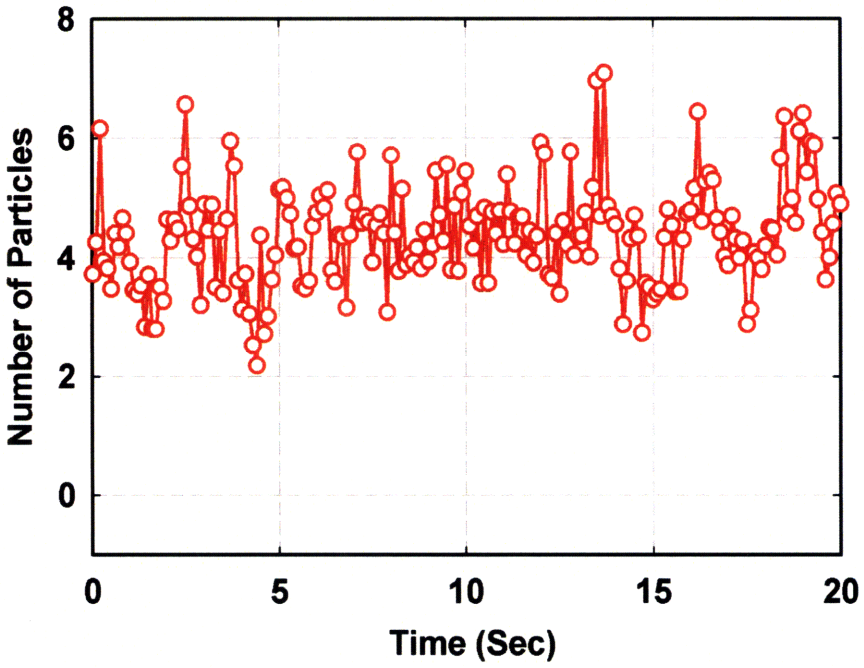

Figure 4.9 The change of the number of QD particles in time

4.4 Summary

In this chapter, we have demonstrated images acquired using TPE DRWFI microscopy is amendable for SPT and ICS analysis. Transport of QD-tagged integrins was imaged using TPE DRWFI microscopy and analyzed with SPT and ICS. For SPT, we observed that integrin exhibits confined diffusion at time scale shorter than 1.3 seconds while transport is observed on the longer time scale. Using ICS, we demonstrated that number density of receptors can be quantified using spatial correlation. For future studies, DRWFI may be expanded for two or

multiple particle tracking. More advanced ICS techniques such as spatio-temporal image correlation spectroscopy (STICS) and k-space image correlation spectroscopy (k-ICS) may be also applied to 3D resolved wide-field images [27-29].

References

1. C. Dietrich, B. Yang, T. Fujiwara, A. Kusumi, and K. Jacobson, "Relationship of lipid rafts to transient confinement zones detected by single particle tracking," Biophysical Journal **82**, 274-284 (2002).
2. B. Nitzsche, F. Ruhnow, and S. Diez, "Quantum-dot-assisted characterization of microtubule rotations during cargo transport," Nature Nanotechnology **3**, 552-556 (2008).
3. H. P. Babcock, C. Chen, and X. W. Zhuang, "Using single-particle tracking to study nuclear trafficking of viral genes," Biophysical Journal **87**, 2749-2758 (2004).
4. B. Brandenburg, and X. W. Zhuang, "Virus trafficking - learning from single-virus tracking," Nature Reviews Microbiology **5**, 197-208 (2007).
5. H. P. Kao, and A. S. Verkman, "Tracking of Single Fluorescent Particles in 3 Dimensions - Use of Cylindrical Optics to Encode Particle Position," Biophysical Journal **67**, 1291-1300 (1994).
6. V. Levi, Q. Q. Ruan, and E. Gratton, "3-D particle tracking in a two-photon microscope: Application to the study of molecular dynamics in cells," Biophysical Journal **88**, 2919-2928 (2005).
7. T. Ragan, H. D. Huang, P. So, and E. Gratton, "3D particle tracking on a two-photon microscope," Journal of Fluorescence **16**, 325-336 (2006).
8. N. O. Petersen, P. L. Hoddelius, P. W. Wiseman, O. Seger, and K. E. Magnusson, "Quantitation of Membrane-Receptor Distributions by Image Correlation Spectroscopy - Concept and Application," Biophysical Journal **65**, 1135-1146 (1993).
9. P. W. Wiseman, J. A. Squier, M. H. Ellisman, and K. R. Wilson, "Two-photon image correlation spectroscopy and image cross-correlation spectroscopy," Journal of Microscopy-Oxford **200**, 14-25 (2000).
10. M. J. Saxton, and K. Jacobson, "Single-particle tracking: Applications to membrane dynamics," Annual Review of Biophysics and Biomolecular Structure **26**, 373-399 (1997).
11. J. P. Bouchaud, and A. Georges, "Anomalous Diffusion in Disordered Media - Statistical Mechanisms, Models and Physical Applications," Physics Reports-Review Section of Physics Letters **195**, 127-293 (1990).
12. M. J. Saxton, "Anomalous Diffusion Due to Obstacles - a Monte-Carlo Study," Biophysical Journal **66**, 394-401 (1994).
13. Q. A. Hong, M. P. Sheetz, and E. L. Elson, "Single-Particle Tracking - Analysis of Diffusion and Flow in 2-Dimensional Systems," Biophysical Journal **60**, 910-921 (1991).
14. E. D. Sheets, R. Simson, and K. Jacobson, "New Insights into Membrane Dynamics from the Analysis of Cell-Surface Interactions by Physical Methods," Current Opinion in Cell Biology **7**, 707-714 (1995).
15. J. W. Dai, and M. P. Sheetz, "Axon Membrane Flows from the Growth Cone to the Cell Body," Cell **83**, 693-701 (1995).

16. G. M. Lee, F. Zhang, A. Ishihara, C. L. Mcneil, and K. A. Jacobson, "Unconfined Lateral Diffusion and an Estimate of Pericellular Matrix Viscosity Revealed by Measuring the Mobility of Gold-Tagged Lipids," Journal of Cell Biology **120**, 25-35 (1993).
17. H. Qian, M. P. Sheetz, and E. L. Elson, "SINGLE PARTICLE TRACKING ANALYSIS OF DIFFUSION AND FLOW IN TWO-DIMENSIONAL SYSTEMS," Biophysical Journal **60**, 910-921 (1991).
18. A. Caspi, R. Granek, and M. Elbaum, "Diffusion and directed motion in cellular transport," Physical Review E **66**, - (2002).
19. M. Weiss, M. Elsner, F. Kartberg, and T. Nilsson, "Anomalous subdiffusion is a measure for cytoplasmic crowding in living cells," Biophysical Journal **87**, 3518-3524 (2004).
20. E. L. Elson, and D. Magde, "Fluorescence Correlation Spectroscopy .1. Conceptual Basis and Theory," Biopolymers **13**, 1-27 (1974).
21. D. Magde, E. L. Elson, and W. W. Webb, "Fluorescence Correlation Spectroscopy .2. Experimental Realization," Biopolymers **13**, 29-61 (1974).
22. D. Magde, W. W. Webb, and E. L. Elson, "Fluorescence Correlation Spectroscopy .3. Uniform Translation and Laminar-Flow," Biopolymers **17**, 361-376 (1978).
23. P. W. Wiseman, and N. O. Petersen, "Image correlation spectroscopy. II. Optimization for ultrasensitive detection of preexisting platelet-derived growth factor-beta receptor oligomers on intact cells," Biophysical Journal **76**, 963-977 (1999).
24. P. W. Wiseman, C. M. Brown, D. J. Webb, B. Hebert, N. L. Johnson, J. A. Squier, M. H. Ellisman, and A. F. Horwitz, "Spatial mapping of integrin interactions and dynamics during cell migration by Image Correlation Microscopy," Journal of Cell Science **117**, 5521-5534 (2004).
25. H. F. Chen, I. Titushkin, M. Stroscio, and M. Cho, "Altered membrane dynamics of quantum dot-conjugated integrins during osteogenic differentiation of human bone marrow derived progenitor cells," Biophysical Journal **92**, 1399-1408 (2007).
26. D. F. Kucik, T. E. O'Toole, A. Zheleznyak, D. K. Busettini, and E. J. Brown, "Activation-enhanced alpha(IIb)beta(3)-integrin-cytoskeleton interactions outside of focal contacts require the alpha-subunit," Molecular Biology of the Cell **12**, 1509-1518 (2001).
27. B. Hebert, S. Costantino, and P. W. Wiseman, "Spatiotemporal image correlation Spectroscopy (STICS) theory, verification, and application to protein velocity mapping in living CHO cells," Biophysical Journal **88**, 3601-3614 (2005).
28. R. P. Kulkarni, D. D. Wu, M. E. Davis, and S. E. Fraser, "Quantitating intracellular transport of polyplexes by spatio-temporal image correlation spectroscopy," Proceedings of the National Academy of Sciences of the United States of America **102**, 7523-7528 (2005).
29. D. L. Kolin, D. Ronis, and P. W. Wiseman, "k-Space image correlation spectroscopy: A method for accurate transport measurements independent of fluorophore photophysics," Biophysical Journal **91**, 3061-3075 (2006).

Chapter 5

DRWFI Applications: II. Three-Dimensional Lithographic Microfabrication

5.1 Introduction

Lithographic fabrication is a cornerstone of semiconductor industry and the extension of the techniques to the micro- or nano-scale recently has found applications in many areas including photonics [1] and biomedicine [2, 3]. Photolithography, the most common microlithography technology, uses light to transfer the desired patterns on the substrate through several photochemical processes, but its resolution is limited by the diffraction limit of the light. To overcome this limitation, several nano-scale fabrication methods have been reported: electron beam lithography [4] which scans electron beam over the surface in patterned fashion, nanoimprinting lithography [5] that stamps patterns on thin layer, dip-pen nanolithography [6] which transfers specific molecules on the surface, nanosphere lithography [7] which uses nanosphere layer as a mask, and soft lithography [8] which replicates structures with elastomer stamps or mold. Most nano-scale fabrications are limited to thin 2D applications, and there is a need to further develop 3D microfabrication techniques.

3D fabrication techniques based on solid freeform fabrication have been used extensively for making prototypes during manufacturing. Stereolithography is one of the most commonly used rapid prototyping techniques in this class. It uses curable photopolymer resin: Laser traces the cross section of the parts at each layer curing the polymer, and the 3D structure is generated by stacking these patterned layers together. While this technique is very useful in generating the macro-scale 3D prototypes, its fabrication resolution is limited to couple of hundred microns. Several 3D micron-scale fabrication techniques have been proposed, and one popular method is TPE microfabrication. The technology of TPE microfabrication [9-11] has been under

development for over twenty years. Importantly, this microfabrication technique can utilize a variety of photo-interactions to alter material properties in 3D. The available processes include photochromism, photobleaching, photopolymerization, and others. Photochromism [12, 13] is a reversible process which optically transforms chemical species between two forms with different physicochemical properties such as absorption spectra, refractive index, or dielectric constant. This process may find application in creating erasable memory media [13] and display devices [14]. Photobleaching [15] is an irreversible process in which fluorescence capability is permanently lost after repeated excitations and emissions. It is caused by photolysis, which is a very complex process. One of the major mechanisms for photobleaching is photodynamic reaction between oxygen and fluorophore. Additionally, it has been revealed, both theoretically and experimentally, that photobleaching is not a single exponential process except for few special cases. Moreover, the reaction order and the photobleaching rate are affected by factors such as light intensity, illumination type (pulsed or continuous), and molecular environment. Photopolymerization [16] is a polymerization process within which the material is exposed to light, especially ultraviolet (UV) light. It is generally modeled as radical chain polymerization. Either photoinitiator or photosensitizer is required to initiate polymerization, but they have different roles in the polymerization process. During photoinitiation, a photoinitiator absorbs energy by excitation and is decomposed into radicals, whereas a photosensitizer absorbs energy by excitation and its molecular interaction and transfers energy to other molecules which become radicals. Regardless of their different roles, polymerization rate is determined by their characteristics. Unlike other polymerization processes, photopolymerization can occur in the spatially confined specific region where the light is irradiated, but the process is affected by the material thickness due to the limited penetration depth of the light. Fabrication resolution by photopolymerization can be higher than diffraction-limited optical resolution since the photopolymerization requires a threshold optical energy to initiate the polymerization process. TPE microfabrication has found a broad range of applications in the fields such as 3D optical storage [17, 18], tissue scaffold [19, 20], photonic crystal structure [21, 22], and microfluidic devices [23, 24].

Several other methods of 3D fabrication besides TPE microfabrication have been introduced. Setting a 3D interference patterns inside a solid specimen by illuminating the object with

multiple coherent plane waves [25-27] is another 3D fabrication method that allows high throughput manufacturing, but its applications are limited to building periodic structures. Soft lithography [28] including self-assembly [29] and microtransfer molding (μTM) [30] has a variety of applications including 3D microfabrication, but it is only applied to large-volume manufacturing since it is mold-cast based fabrication. 3D fabrication with dip pen [31] enables ink direct writing, but it cannot be applied to high-aspect-ratio or nail-shaped structures. Finally, 3D nanoimprinting lithography [32] has also been reported, but the range of 3D structures that have been made is also quite limited.

One of the limits of many 3D microfabrication techniques, including TPE microfabrication, is their low throughput. TPE typically achieves 3D resolution by focusing ultrafast optical pulses to a diffraction-limited focus using a high NA lens. The nonlinear dependence of material responses to the excitation power distribution provides the depth discrimination. Since this fabrication processing is carried out on a point-by-point basis, known as laser direct writing, the throughput of fabrication is ultimately limited by the sequential nature of this method and the mechanical limit of the scanner. Although TPE microfabrication provides very attractive submicron lateral resolution and 3D optical sectioning, the use of the TPE approach is limited to laboratory investigations and prototype fabrication. Therefore, there is a need to improve the throughput of TPE microfabrication to enable commercial mass-production. One approach, which can enhance the speed of TPE microfabrication beyond that of laser direct writing, is based on using multiple beamlets [33, 34] to generate multiple foci on the sample. This parallelization increases fabrication speed by a factor equal to the number of excitation foci. One limitation of this technique lies in the difficulty of individually controlling the scan pattern of an individual beamlet and registering the patterns produced by the different foci.

In this chapter, we introduce a novel 3D lithographic microfabrication technique based on DRWFI. DRWFI has found a number of applications in the nonlinear microscopy [35-38], but using this approach for 3D microfabrication has remained unexplored. As a proof-of-concept, a TPE microfabrication station based on DRWFI is assembled, micropatterning based on photobleaching is demonstrated, and fabrication resolution is evaluated. To the best of our knowledge, this is the first demonstration of 3D lithographic microfabrication using DRWFI.

5.2 3D Lithographic Microfabrication

5.2.1 Design and Implementation of 3D Lithographic Microfabrication

Currently, 3D volumetric microstructures are generated by focusing pulsed laser into a focal volume, scanning laser beam laterally and translating the objective lens or the sample axially (See figure 5.1(a)). By controlling the laser power and exposure time, sub-diffraction limited fabrication resolution can be achieved, but this requires complicated system integration that includes a high-speed programmable mechanical shutter and a 3D scanner. The sequential nature of this system and the limited bandwidth of the mechano-optical scanners slow the fabrication rate and confine TPE microfabrication application to prototyping. For the technology proposed in this thesis, there is no need for lateral scanning and only axial scanning of the objective (or sample platform) is required for fabrication in 3D. As seen in figure 5.1(b), DRWFI is used to excite sample in a wide-field excitation format. At the image plane of the specimen, a mask is placed to project the specific pattern at the focal plane of the specimen. 3D objects are then created by stacking up 2D lithographic produced structures layer-by-layer. This approach significantly improves the throughput of the fabrication and may enable applications which require mass-production.

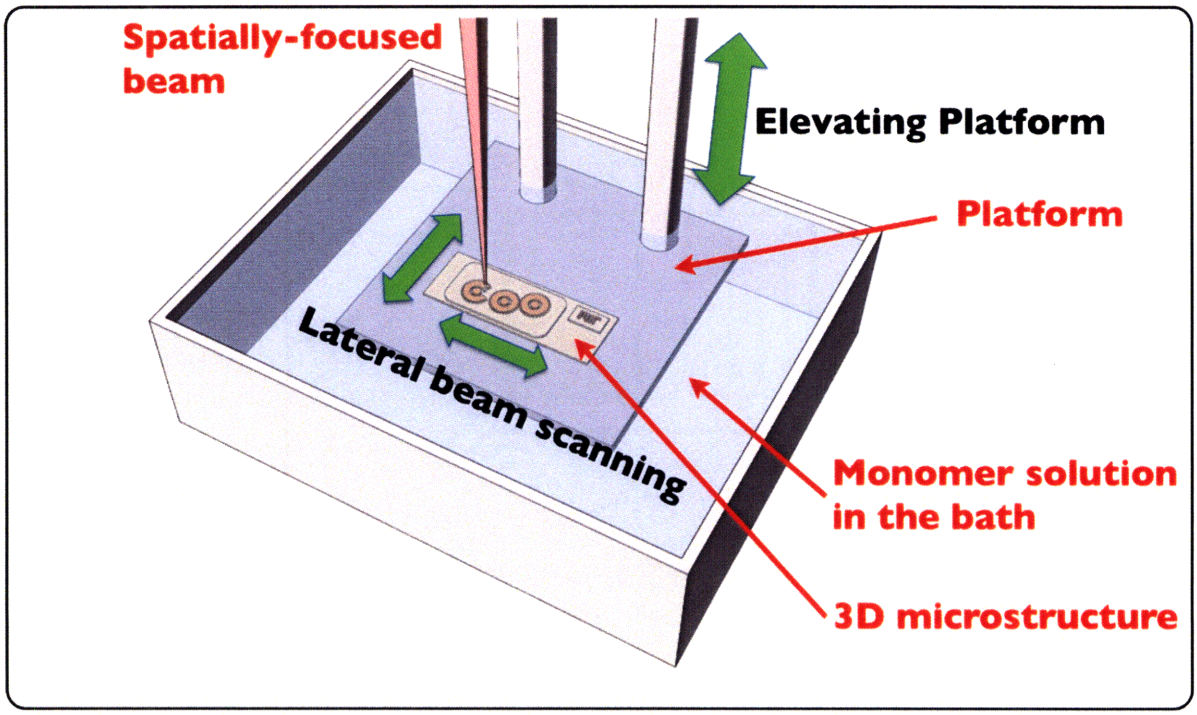

(a)

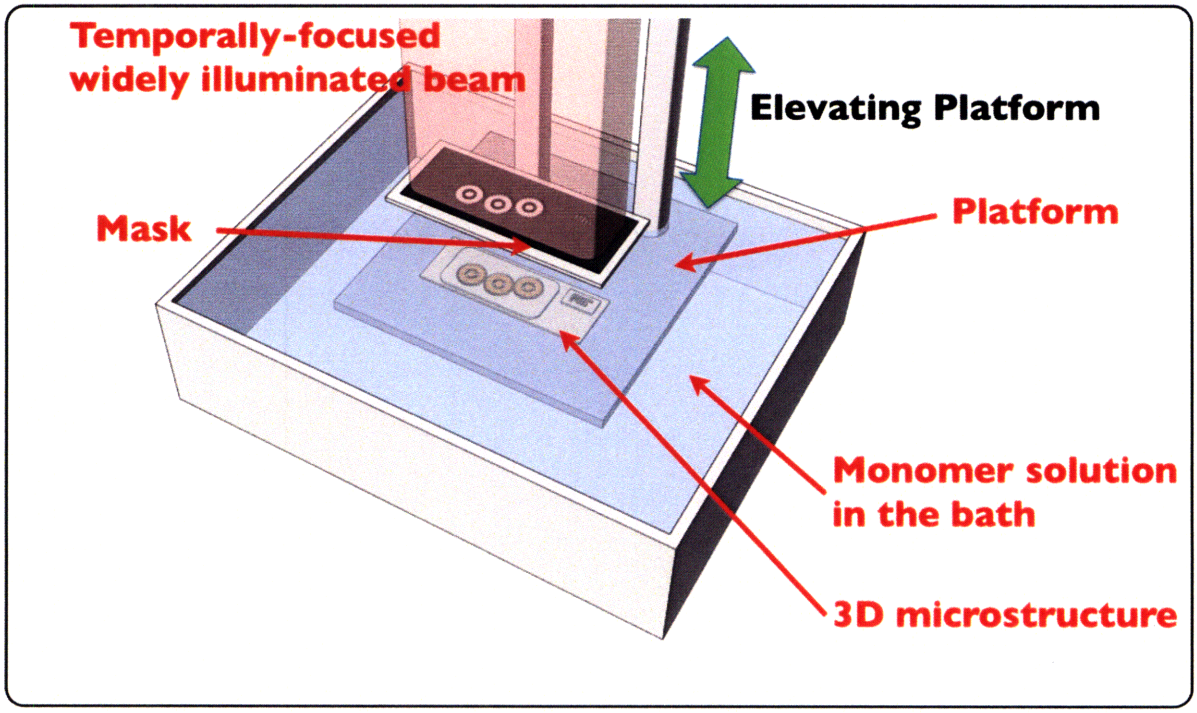

(b)

Figure 5.1 3D Microfabrication based on two-photon absorption process: (a) current technology (laser direct writing) and (b) proposed technology (3D lithographic microfabrication)

The design of the 3D lithographic microfabrication system is shown in figure 5.2. It is very similar to the imaging system shown in chapter 3 except for inserting different masks to generate the specific patterns. As a light source, Ti:Sapphire femtosecond laser (Tsunami, Spectra-Physics, Mountain View, CA) pumped by a CW DPSS laser (Millennia V, Spectra-Physics, Mountain View, CA) was used. It has pulse width of about 100 fs and pulse repetition rate of 80 MHz. The center wavelength of the ultrafast optical pulses was chosen as 780 nm. It consists of reflective diffraction grating with a groove frequency of 600 glooves/mm (53004BK02-35IR, Richardson Grating Lab, Rochester, NY), the high NA objective (Fluar, 40X/1.30 Oil, Zeiss MicroImaging, Thornwood, NY), and customized masks (Fine Line Imaging Inc., Cololado Springs, CO). The diffraction grating surface and the mask surface are placed at the conjugate planes of the objective specimen plane. This organization ensures that the pattern of the mask is projected at the specimen plane, and the optical pulse width is restored at the same location. Fabrication is accomplished one plane at a time. After a pattern is fabricated, the objective is moved to the next axial position, and the mask for this position is inserted. To observe the fabrication result, an image sensor (iCCD, PI-MAX, Princeton Instrument, Trenton, NJ) is used. In future high throughput fabrication, we plan to replace these fixed masks with a dynamic mask generator such as a digital mirror device (DMD) with a digital light processor (DLP), a spatial light modulator (SLM), or a micromirror array (MA).

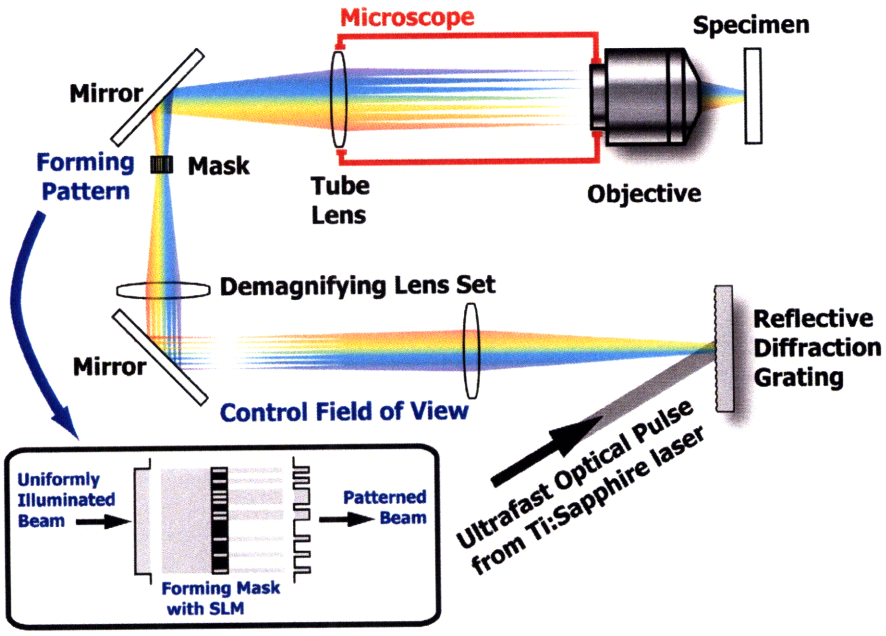

Figure 5.2 Schematic diagram for 3D lithographic microfabrication

5.2.2 Evaluating Axial Resolution of Fabricated Patterns

We demonstrate the feasibility of using DRWFI for lithographic fabrication by photobleaching depth-resolved patterns in fluorescent materials. Photobleaching process is also useful for simulating another useful fabrication process based on photopolymerization. Photopolymerization requires interaction with reactive oxygen species, which is similar to photobleaching [15, 39]. One of the challenges to quantify the axial resolution is that prolonged photobleaching will result in resolution degradation while too short exposure may result in poor SNR. Using a specimen with a high concentration of non-diffusing fluorophores is critical to obtain high SNR patterns. For this purpose, 15μm diameter yellow-green (505/515) fluorescent polystyrene microspheres (F-8844, Invitrogen, Carlsbad, CA) were used. It is critical that these microspheres be embedded with medium with very similar refractive index (RI). With index mismatch, the spherical surfaces of these microspheres lead to wave front distortion and aberration. The RI of polystyrene-based microsphere is known to be 1.590 at 589.25 nm from the manufacturer data. However, since RI is a function of wavelength, the RI is unknown at our patterning wavelength of 780 nm. To select the best embedded medium, we applied diffraction phase contrast microscopy [40] to quantify the RI difference between the microsphere and the

embedding medium. Several embedding media were tested, and the RI difference for each is listed in table 5.1. For large refractive index difference, RI difference is far from actual value since diffraction phase microscopy does not have a broad dynamic range. The RI of RI matching oils, UV adhesives, and laser liquids are close to that of microsphere at 589.25 nm. Among the candidates, laser liquid #2 has the closest RI to the microsphere at 800 nm, as shown in table 5.1, and is chosen as embedding medium for subsequent experiments.

Surrounding Medium	Known Refractive Index at 589.20 nm	Refractive Index difference between microsphere and medium at 800 nm
Air	1.000	0.18052
Water	1.333	0.13958
Glycerol	1.473	0.091311
Immersion Oil[a]	1.518	0.085085
RI matching Oil[b]	1.580	0.027417
UV Adhesive #1[c,e]	1.560	0.038172
UV Adhesive #2[d,e]	1.585	0.021119
Laser Liquid #1[b]	1.590	0.015945
Laser Liquid #2[b]	1.605	0.004802

a. 518F, Carl Zeiss Microimaging Inc., Thornwood, NY
b. custom, Cargille Laboratories, Cedar Grove, NJ
c. NOA 61, Norland Products Inc., Cranbury, NJ
d. OP-4-20658, Dymax Corporation, Torrington, CT
e. It was measured after fully curing UV adhesive.

Table 5.1 The list of refractive index difference between microsphere and surrounding media.

The specimen for evaluating axial fabrication resolution was prepared as follows: 15μm diameter fluorescent spheres were diluted with deionized water at the ratio of 1:20, centrifuged at 5000 rpm for two minutes, and removed of water with NaCl. They were dried on the square no.1.5 cover glass (48366-227, VWR, West Chester, PA) in a vacuum chamber. RI matching embedding medium was deposited on the cover glass around the microspheres. The cover glass was sealed to a microscope slide glass (3050, 25 mm X 75 mm & 1mm thick, BD, Short Hills, NJ). Figure 5.3 describes writing and reading process for photobleached micropatterns. For

writing photobleached micropattern, the DRWFI microfabrication system was used to write the MIT logo in the center of the microsphere. Each letter of micropattern in the microsphere was smaller than 4 μm in the lateral dimension. To minimize refractive index mismatching during the imaging process, standard point scanning TPM, as described in chapter 2, is used to read out these patterns since it has higher axial resolution than two-photon system based on DRWFI. 201 images were taken with axial step size of 100 nm. Averaged intensity profile for normal voxel and photobleached voxel were processed in ImageJ (Rasband, W.S., ImageJ, National Institutes of Health, Bethesda, Maryland, USA, http://rsb.info.nih.gov/ij/, 1997-2009), and photobleached intensity was subtracted from normal intensity profile. In this experiment, the laser power used for measurement was 500 mW before the grating, and the exposure time was controlled to observe the effects on axial fabrication resolution.

The axial resolution of the fabricated pattern measured by TPM imaging is a convolution of the fabrication resolution and the imaging resolution. Axial optical resolution for DRWFI observed in chapter 3 was 1.65 μm, and the TPM used in chapter 2 has an axial optical resolution of 1.16 μm. Therefore, we expect the images of the photobleached patterns has an axial resolution of 2.27 μm. Figure 5.4(a) shows the FWHM of the photobleached patterns imaged using TPM at different exposure time. For comparison, the axial resolutions with UV adhesive #2 and laser oil #1 and #2 embedding media were also plotted. It is observed that long exposure time results in fabrication resolution loss due to saturation; similar resolution degradation was observed, using laser direct writing [41]. As exposure time decreases, the fabrication resolution becomes closer to our theoretical expectation. For very short exposure, the accuracy of the measurement is limited by Poisson noise due to low contrast in this case. Figure 5.4(b) shows that the measured axial resolution intensity distribution closely matches that of the theoretical estimate.

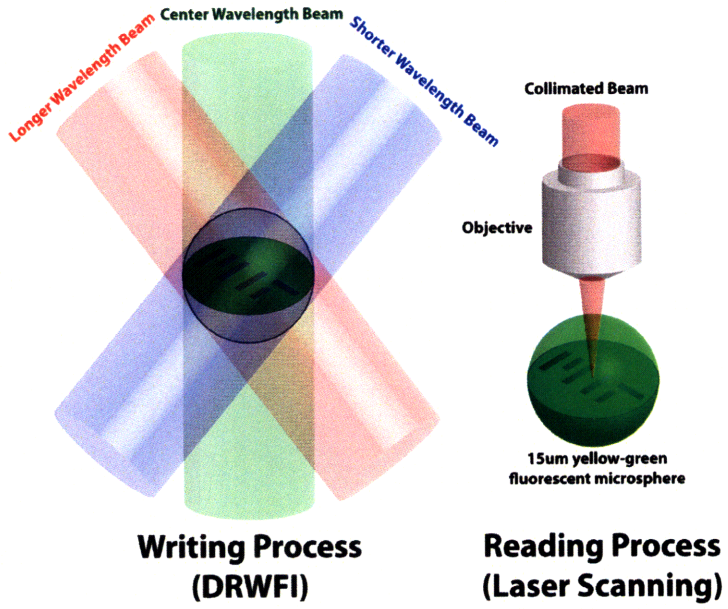

Figure 5.3 Photobleaching-based micropattern writing and reading

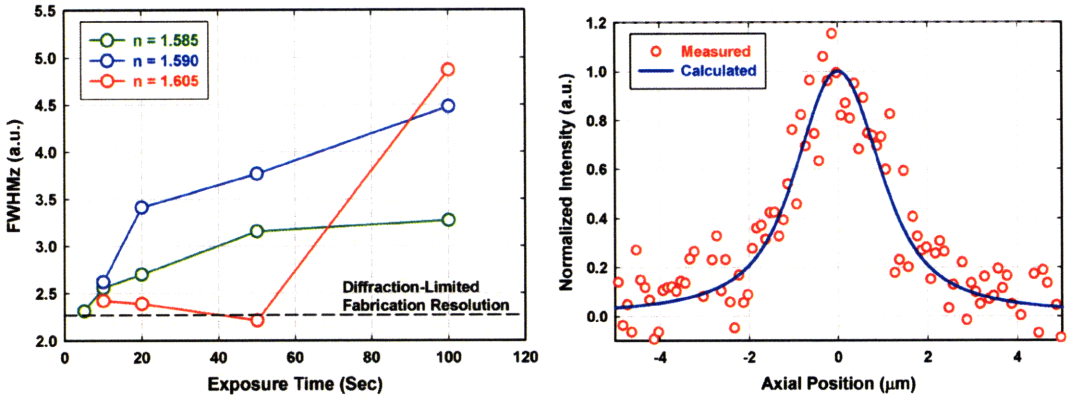

(a) (b)

Figure 5.4 Axial fabrication resolution: (a) Axial resolution with different exposure time and surrounding media (UV adhesive #2: green, laser liquid #1: blue, and laser liquid #2: red) (b) Intensity profiles for the measurement and the calculation of convolution of writing and reading intensity profiles (solid line) (For measurement, laser oil #2 was embedding medium, and exposure time was 50 seconds.)

5.3 3D Depth-Resolved Micropatterning

In this section, we demonstrate depth resolved micropatterning using DRWFI. Figure 5.5(a) explains how a depth-resolved micropattern is created in the microsphere. Customized chrome-coated mask was used to generate different patterns at different depths. The focal plane was controlled by a microscope objective piezoelectric positioner (MIPOS500, Piezosystem jena Inc., Hopedale, MA) with closed-loop controller (NV 40/1 CLE, Piezosystem jena Inc., Hopedale, MA). In this case, the 'M', 'I', and 'T' of the MIT logo were written with 5 μm axial separation in the microsphere. During writing process, 500 mW average laser power before the grating and 20 second exposure time were used for each pattern. For reading these micropatterns, TPM was used as discussed in the previous section. Figure 5.5(b) shows the fluorescence images at the depths where letters were written. Each letter was clearly identified at different depths. The crosstalk between layers is very small. This level of cross talk may be reduced by further minimizing aberration.

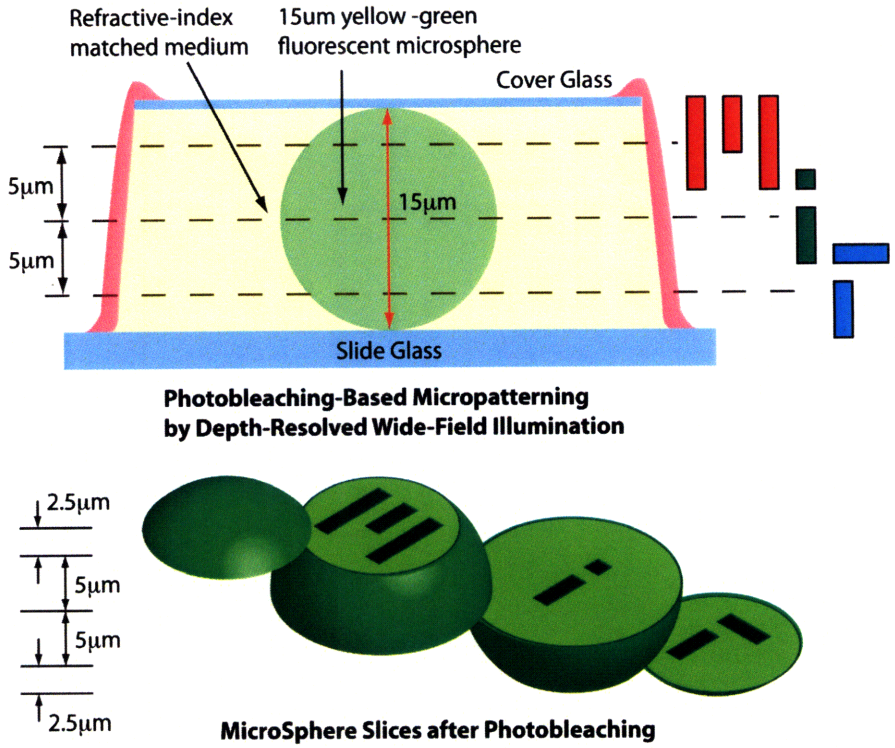

(a)

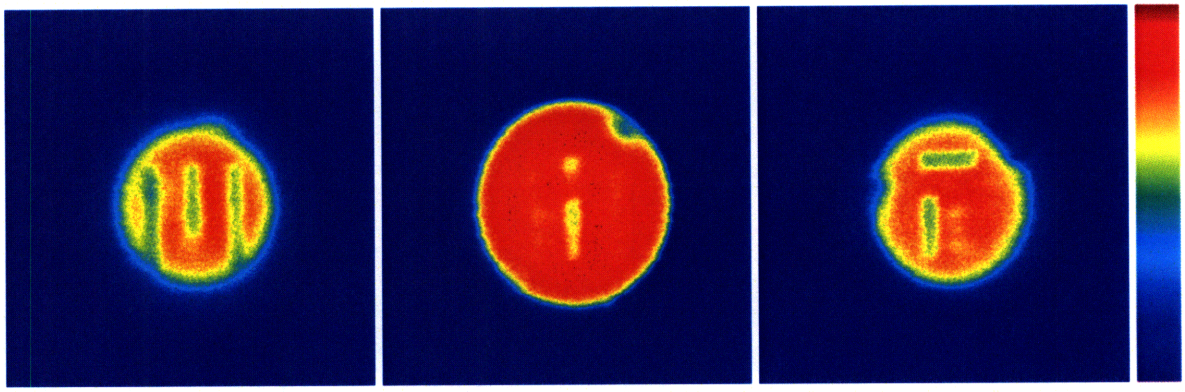

(b)

Figure 5.5 3D depth-resolved micropatterning in the microsphere (a) pictorial illustration of micropatterning at the different depths. 'MIT' logo was written: 'M' at top, 'I' at middle, 'T' at bottom (b) reading patterns at different layer. (from left to right) 5μm above center, at the center, and 5 μm below center.

5.4 Summary

In this chapter, 3D lithographic microfabrication system was introduced and implemented. This system can be exploited for mass-production thanks to its DRWFI capability to improve fabrication rate. Photobleaching process was used in these proof-of-concept experiments. We have demonstrated that diffraction-limited writing resolution can be achieved. We have further demonstrated that DRWFI can pattern structures at multiple depths with minimal crosstalk.

While we have demonstrated that the utility of DRWFI for 3D lithography based on photobleaching process, we expect that other patterning mechanisms such as photopolymerization can also be readily used. In the photopolymerization process, photoinitiators are excited by the laser to form radicals. These excited photoinitiators transfers energy to mononers forming radicals starting the polymerization process. For photopolymerization, structures with features below the optical diffraction limit may be produced due to the presence of a threshold energy level below which polymerization cannot be initiated [42]. The presence of this threshold further reduces the undesirable effect of crosstalk between planes that is caused by aberration and the relatively broad axial PSF of DRWFI.

References

1. M. Campbell, D. N. Sharp, M. T. Harrison, R. G. Denning, and A. J. Turberfield, "Fabrication of photonic crystals for the visible spectrum by holographic lithography," Nature **404**, 53-56 (2000).
2. G. Vozzi, C. Flaim, A. Ahluwalia, and S. Bhatia, "Fabrication of PLGA scaffolds using soft lithography and microsyringe deposition," Biomaterials **24**, 2533-2540 (2003).
3. S. J. Hollister, "Porous scaffold design for tissue engineering," Nature Materials **4**, 518-524 (2005).
4. H. G. Craighead, "Ultra-High-Resolution Electron-Beam Lithography," Journal of Electron Microscopy Technique **2**, 147-155 (1985).
5. S. Y. Chou, P. R. Krauss, and P. J. Renstrom, "Imprint lithography with 25-nanometer resolution," Science **272**, 85-87 (1996).
6. R. D. Piner, J. Zhu, F. Xu, S. H. Hong, and C. A. Mirkin, ""Dip-pen" nanolithography," Science **283**, 661-663 (1999).
7. C. L. Haynes, and R. P. Van Duyne, "Nanosphere lithography: A versatile nanofabrication tool for studies of size-dependent nanoparticle optics," Journal of Physical Chemistry B **105**, 5599-5611 (2001).

8. Y. N. Xia, and G. M. Whitesides, "Soft lithography," Annual Review of Materials Science **28**, 153-184 (1998).
9. J. H. Strickler, and W. W. Webb, "3-Dimensional Optical-Data Storage in Refractive Media by 2-Photon Point Excitation," Optics Letters **16**, 1780-1782 (1991).
10. D. Yang, S. J. Jhaveri, and C. K. Ober, "Three-dimensional microfabrication by two-photon lithography," Mrs Bulletin **30**, 976-982 (2005).
11. S. Maruo, and J. T. Fourkas, "Recent progress in multiphoton microfabrication," Laser & Photonics Reviews **2**, 100-111 (2008).
12. Y. Hirshberg, "Reversible Formation and Eradication of Colors by Irradiation at Low Temperatures. A Photochemical Memory Model," Journal of the American Chemical Society **78**, 2304-2312 (1956).
13. M. Irie, "Photochromism: Memories and switches - Introduction," Chemical Reviews **100**, 1683-1683 (2000).
14. J. N. Yao, K. Hashimoto, and A. Fujishima, "Photochromism Induced in an Electrolytically Pretreated Moo3 Thin-Film by Visible-Light," Nature **355**, 624-626 (1992).
15. J. B. Pawley, *Handbook of biological confocal microscopy* (Springer, New York, NY, 2006).
16. G. G. Odian, *Principles of polymerization* (Wiley-Interscience, Hoboken, N.J., 2004).
17. C. E. Olson, M. J. R. Previte, and J. T. Fourkas, "Efficient and robust multiphoton data storage in molecular glasses and highly crosslinked polymers," Nature Materials **1**, 225-228 (2002).
18. B. H. Cumpston, S. P. Ananthavel, S. Barlow, D. L. Dyer, J. E. Ehrlich, L. L. Erskine, A. A. Heikal, S. M. Kuebler, I. Y. S. Lee, D. McCord-Maughon, J. Q. Qin, H. Rockel, M. Rumi, X. L. Wu, S. R. Marder, and J. W. Perry, "Two-photon polymerization initiators for three-dimensional optical data storage and microfabrication," Nature **398**, 51-54 (1999).
19. G. D. Pins, K. A. Bush, L. P. Cunningham, and P. J. Carnpagnola, "Multiphoton excited fabricated nano and micro patterned extracellular matrix proteins direct cellular morphology," Journal of Biomedical Materials Research Part A **78A**, 194-204 (2006).
20. F. Claeyssens, E. A. Hasan, A. Gaidukeviciute, D. S. Achilleos, A. Ranella, C. Reinhardt, A. Ovsianikov, S. Xiao, C. Fotakis, M. Vamvakaki, B. N. Chichkov, and M. Farsari, "Three-Dimensional Biodegradable Structures Fabricated by Two-Photon Polymerization," Langmuir **25**, 3219-3223 (2009).
21. M. Straub, M. Ventura, and M. Gu, "Multiple higher-order stop gaps in infrared polymer photonic crystals," Physical Review Letters **91**, - (2003).
22. R. Guo, Z. Y. Li, Z. W. Jiang, D. J. Yuan, W. H. Huang, and A. D. Xia, "Log-pile photonic crystal fabricated by two-photon photopolymerization," Journal of Optics a-Pure and Applied Optics **7**, 396-399 (2005).
23. J. Wu, D. Day, and M. Gu, "A microfluidic refractive index sensor based on an integrated three-dimensional photonic crystal," Applied Physics Letters **92**, - (2008).
24. M. Stoneman, M. Fox, C. Y. Zeng, and V. Raicu, "Real-time monitoring of two-photon photopolymerization for use in fabrication of microfluidic devices," Lab on a Chip **9**, 819-827 (2009).
25. T. Kondo, S. Matsuo, S. Juodkazis, and H. Misawa, "Femtosecond laser interference technique with diffractive beam splitter for fabrication of three-dimensional photonic crystals," Applied Physics Letters **79**, 725-727 (2001).

26. S. Shoji, and S. Kawata, "Photofabrication of three-dimensional photonic crystals by multibeam laser interference into a photopolymerizable resin," Applied Physics Letters **76**, 2668-2670 (2000).
27. H. B. Sun, A. Nakamura, S. Shoji, X. M. Duan, and S. Kawata, "Three-dimensional nanonetwork assembled in a photopolymerized rod array," Advanced Materials **15**, 2011-2014 (2003).
28. Y. N. Xia, and G. M. Whitesides, "Soft lithography," Angewandte Chemie-International Edition **37**, 551-575 (1998).
29. G. M. Whitesides, and B. Grzybowski, "Self-assembly at all scales," Science **295**, 2418-2421 (2002).
30. C. N. LaFratta, T. Baldacchini, R. A. Farrer, J. T. Fourkas, M. C. Teich, B. E. A. Saleh, and M. J. Naughton, "Replication of two-photon-polymerized structures with extremely high aspect ratios and large overhangs," Journal of Physical Chemistry B **108**, 11256-11258 (2004).
31. G. M. Gratson, M. J. Xu, and J. A. Lewis, "Microperiodic structures - Direct writing of three-dimensional webs," Nature **428**, 386-386 (2004).
32. M. T. Li, L. Chen, and S. Y. Chou, "Direct three-dimensional patterning using nanoimprint lithography," Applied Physics Letters **78**, 3322-3324 (2001).
33. D. N. Fittinghoff, and J. A. Squier, "Time-decorrelated multifocal array for multiphoton microscopy and micromachining," Optics Letters **25**, 1213-1215 (2000).
34. D. N. Fittinghoff, C. B. Schaffer, E. Mazur, and J. A. Squier, "Time-decorrelated multifocal micromachining and trapping," Ieee Journal of Selected Topics in Quantum Electronics **7**, 559-566 (2001).
35. D. Oron, and Y. Silberberg, "Harmonic generation with temporally focused ultrashort pulses," Journal of the Optical Society of America B-Optical Physics **22**, 2660-2663 (2005).
36. M. E. Durst, G. H. Zhu, and C. Xu, "Simultaneous spatial and temporal focusing for axial scanning," Optics Express **14**, 12243-12254 (2006).
37. H. Suchowski, D. Oron, and Y. Silberberg, "Generation of a dark nonlinear focus by spatio-temporal coherent control," Optics Communications **264**, 482-487 (2006).
38. M. E. Durst, G. Zhu, and C. Xu, "Simultaneous spatial and temporal focusing in nonlinear microscopy," Optics Communications **281**, 1796-1805 (2008).
39. T. J. Farrell, R. P. Hawkes, M. S. Patterson, and B. C. Wilson, "Modeling of photosensitizer fluorescence emission and photobleaching for photodynamic therapy dosimetry," Applied Optics **37**, 7168-7183 (1998).
40. Y. K. Park, G. Popescu, K. Badizadegan, R. R. Dasari, and M. S. Feld, "Diffraction phase and fluorescence microscopy," Optics Express **14**, 8263-8268 (2006).
41. T. Asavei, T. A. Nieminen, N. R. Heckenberg, and H. Rubinsztein-Dunlop, "Fabrication of microstructures for optically driven micromachines using two-photon photopolymerization of UV curing resins," Journal of Optics a-Pure and Applied Optics **11**, 7 (2009).
42. H. B. Sun, T. Kawakami, Y. Xu, J. Y. Ye, S. Matuso, H. Misawa, M. Miwa, and R. Kaneko, "Real three-dimensional microstructures fabricated by photopolymerization of resins through two-photon absorption," Optics Letters **25**, 1110-1112 (2000).

Chapter 6

Conclusion and Outlook

6.1 Conclusion

In this thesis, we examined several aspects of ultrafast optical pulse manipulation for nonlinear microscopy and microfabrication. To make the nonlinear microscopes portable, ultrafast optical pulse delivery with fiber was investigated. When TIR-based optical fibers are used, the shape of ultrafast optical pulse is affected temporally and spectrally due to dispersion and nonlinear effects. Dispersion can be compensated with a pulse compressor that provides prechirping, but nonlinear effects become dominant as optical power increases. PCFs, especially hollow-core PCF, are excellent in preserving ultrafast optical pulse shape and also shown to be power-independent. In the realm of nonlinear microscopy, all the fiber delivery methods have lower TPE efficiency than free-space delivery case. Dispersion compensation with pulse compressor partly recovers TPE efficiency in some fibers.

We have further designed DRWFI systems based on temporal focusing. A mathematical model for DRWFI was derived based on diffraction theory. Numerical simulation was used since the mathematical model does not provide a closed-form solution. Through the numerical simulations for different design parameters, we found that axial optical resolution for DRWFI becomes diffraction-limited as spectral components in ultrafast optical pulse are close to filling the back aperture of the objective. A TPE microscope based on DRWFI was built and the experimental resolution was shown to be well matched with the theoretical prediction. Single particle detection sensitivity was demonstrated by imaging single QD at video rate. Single QD blinking and photobleaching dynamics were observed. High-speed cellular imaging was confirmed by imaging fixed cells labeled with QDs at a frame speed that is equivalent to super-video rate.

Additionally, two specific applications of DRWFI were investigated. First, DRWFI was applied to study integrin dynamics in live cell membrane using SPT and ICS. Second, a 3D lithographic microfabrication system was designed and implemented. Its 3D fabrication capability was quantified through photobleaching experiment. Micropatterns produced by the photobleaching process were clearly depth-resolved at the different depths in fluorescent microspheres.

6.2 Outlook

This thesis demonstrates the potential of ultrafast pulse manipulation for microscopic imaging and fabrication. Most importantly, we have demonstrated that temporal focusing is an excellent method for DRWFI. While only a few obvious applications of DRWFI were demonstrated, there are many future possibilities in advancing this class of technology.

6.2.1 Improving Axial Resolution by Standing-Wave DRWFI

As stated in chapter 3, DRWFI can achieve diffraction-limited resolution with proper design parameters. However, compared with lateral resolution, the ultimate axial resolution is generally lower by the factor of at least two. This PSF is an axially-elongated spheroid. In some applications, better axial resolution is desirable. Axial resolution enhancement can be achieved using a standing-wave excitation geometry [1]. Standing-wave depth-resolved wide-field illumination (SWDRWFI) uses two countering propagating pulses that are chirped such that their temporal pulse widths are broadened while the pulses are far from the focal plane. Figure 6.1(a) shows SWDRWFI schematics. A single train of optical pulses is separated into two identical beams by a 50:50 beam splitter (BS). Considering each spectral component separately, the beamlets for each spectral component propagate through two different optical paths and recombine at the focal plane of the objective. Note that the propagation directions of these two beamlets are symmetrical about focal plane but asymmetric relative to the optical axis. With this standing-wave geometry, the beamlets of each wavelength component interfere and produce an interference pattern axially. The interference pattern for each spectral component is perpendicular to the optical axis and parallel to focal plane. The interference patterns of the different spectral components are designed to be in phase at the focal plane where the short pulse

temporal profile is restored, resulting in very high instantaneous power. The axial resolution should be approximately equal to the product of the interference fringe with the axial point spread function of the standard DRWFI. Since the interference fringe is much narrower than the DRWFI axial PSF, the axial resolution as defined by the FWHM of central peak is dominated by the width of the interference fringe that is on the order of 200 nm for 800 nm excitation light. In traditional standing wave microscopy, the planes at all the interference fringe maxima are equally excited, and the signals from these planes are degenerate and cannot be resolved. In SWDRWFI, the interference fringe maxima, which are not located at the focal plane, are attenuated due the temporal focusing effect (i.e. modulated by the standard DRWFI axial point spread function). This breaks the limitations of degeneracy plaguing standing-wave microscopy that persisted for years.

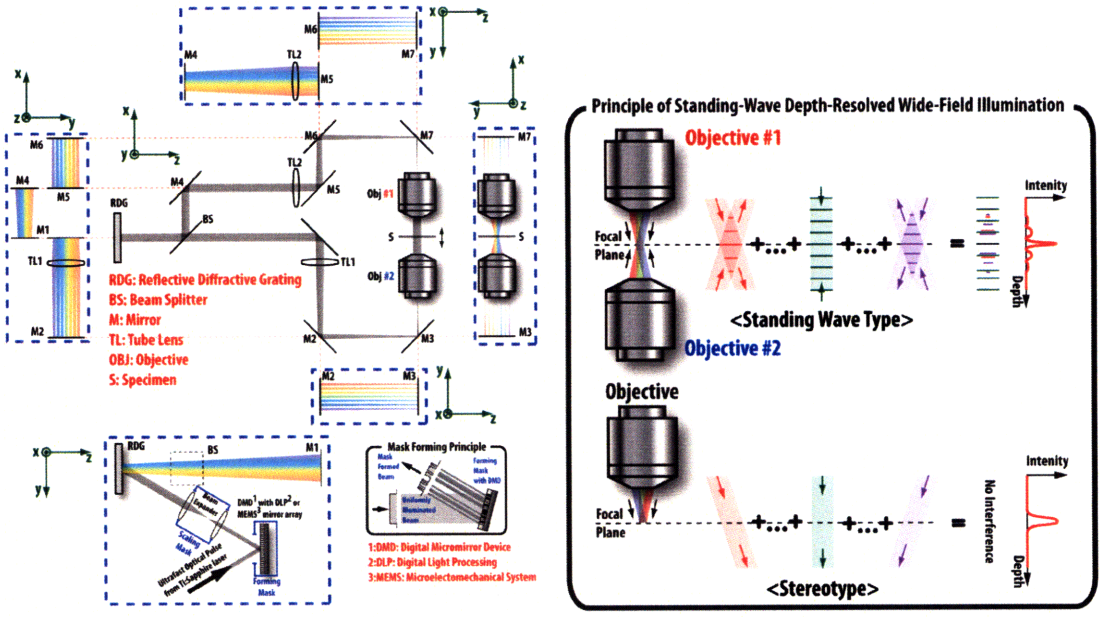

(a) **(b)**

Figure 6.1 (a) Schematic diagram for standing-wave depth-resolved wide-field illumination (b) Principle of SWDRWFI

6.2.2 Expanding Image/Fabrication Area in DRWFI

One advantage of the proposed 3D lithographic microfabrication is scalability. The parallel nature of this technique ensures that patterning a larger area does not take a longer time than doing a smaller area. However, DRWFI patterning is scalable only if there is sufficient laser

power. Microfabrication based on DRWFI is equivalent to simultaneous exciting an array of foci in terms of power requirement. As discussed in section 1.3.2, the quadratic dependence of excitation efficiency on laser power dictates that for the imaging or the fabrication, efficiency is maximized when excitation power is just below saturation limit and chromophores are excited with high probability. For typical photoinitators, at most 100 foci can be efficiently excited given the power available from a typical Ti:Sapphire lasers and this corresponds to a very modest FOV of a few tens of square microns. Given the quadratic nature of TPE, this limitation can be overcome, using a laser source with similar average power but much higher peak power and lower repetition rate. In practice, ultrafast optical pulse with much higher peak power can be produced by regenerative amplifier or OPA. Another approach to enhance laser power is using customized photoinitiator or photosensitizer with high two-photon cross section. One of conjugated polymer nanoparticles (CPNs) was recently confirmed to have high two-photon cross section of 10^3-10^4 GM (A. Abdul Rahim, W. McDaniel, K. Bardon, S. Srinivasan, V. Vickerman, P. T. C. So, and J. H. Moon, "Conjugated Polymer Nanoparticles for Two-photon Imaging of Endothelial Cells in a Tissue Model", Adv. Mater. In press (2009)). Photoinitiators based on conjugated polymers may be developed with significantly higher two-photon cross sections. Figure 6.2 tabulates the expected fabrication area for different laser types and photosensitizers without fluorescence saturation. As shown in figure 6.2, the combination of high peak power laser and large two-photon cross section improves illumination FOV, especially in the case of using regenerative amplifier as light source and CPN based initiators.

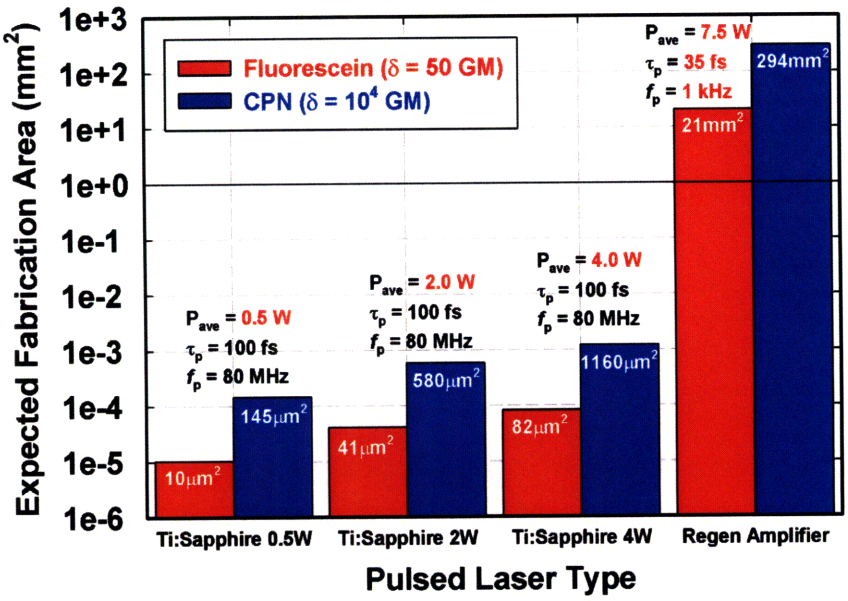

Figure 6.2 Minimum fabrication area with different laser types and fluorescence-based photosensitizers (δ is two-photon cross section). Each pulsed laser specification is described in the figure.

6.2.3 Developing STICS based on DRWFI

In chapter 4, the potential of ICS and ICCS based DRWFI was demonstrated. ICS and ICCS are excellent tools for observing molecular dynamics in cells, but their measurements provide either spatial or temporal information, but not both simultaneously. These tools have been extended to STICS [2, 3] to combine temporal and spatial autocorrelation. STICS has been applied to studying protein dynamics in space and in time simultaneously by measuring transport and diffusion rates and the degree of protein aggregation. The high frame rate and 3D resolved nature of DRWFI makes it ideal for STICS analysis. While QDs have many desirable properties, they also suffer from being often trapped in dark states that is the origin of their blinking behavior. For ICS and ICCS, this blinking dynamics hinders accurate measurement. To overcome this problem, k-ICS [4] has been recently introduced, which is applied to detect QD-tagged macromolecule [5]. We will explore the use of k-ICS to compensate for the blinking behavior in QDs. Finally, other high two-photon cross section probes such as CPNs may also be used with similar performance as QDs, but do not exhibit the undesirable blinking behavior.

6.2.4 Developing Two-Photon Microendoscopy Using DRWFI

An important clinical application of TPE microscopy is in optical biopsy. For optical biopsy, the TPM system must be miniaturized to the format of an endoscope. Several TPE microendoscopies [6-8] have been developed. Most of these devices require 2D or 3D scanning mechanism in the proximal end. Despite the advance in micro-electro-mechanical system (MEMS) technology, these probe designs are quite complex. One may envision designing endoscopies based on DRWFI that eases many design constraints since only scanning along axial direction is required. Moreover, DRWFI is relatively insensitive to dispersion effects during fiber delivery, and it does not require pulse compressor in the proximal end. Two different design schematics are shown in figure 6.3. In both designs, single mode fiber delivers ultrafast optical pulse, and a fiber bundle relays the image from the distal end of the microendoscopy to an external high sensitivity detector. The first design is a side-viewing system (See figure 6.3(a)). Ultrafast optical pulse is delivered by the fiber and collimated by a graded index (GRIN) lens. Subsequently, a grating disperses the spectral content of the light pulse to different angles. A series of silver coated prisms is used to increase the effective path length to ensure sufficient spatial dispersion of the spectral content when the light pulse reaches the objective back aperture after the excitation tube lens and the dichroic mirror (both the tube lens and the objective are high NA GRIN lens). The grating plane and the objective focal plane are designed to be conjugated. Therefore, the different spectral content of the light pulse recombines only at the specimen plane, enabling depth resolved wide-field imaging. The fluorescence signal emitted from the focal plane is imaged by the objective, reflected by dichroic mirror, and projected onto the detection fiber bundle. An alternative design is a front-viewing microendoscopy (See figure 6.3(b)). Front-viewing design has the advantage of small size and easy alignment. Without the right-angle objective-tube lens geometry, it is easier to design a system that is small enough (3-5 mm dia.) to fit into the diagnostic channel of a commercial gastrointestinal endoscope. Furthermore, it is easier to align since the series of GRIN lenses, prisms, and dichroic mirror is cascaded. One of the challenges in this design is the need for custom fabricated GRIN lenses with very specific gradient constant and focal length.

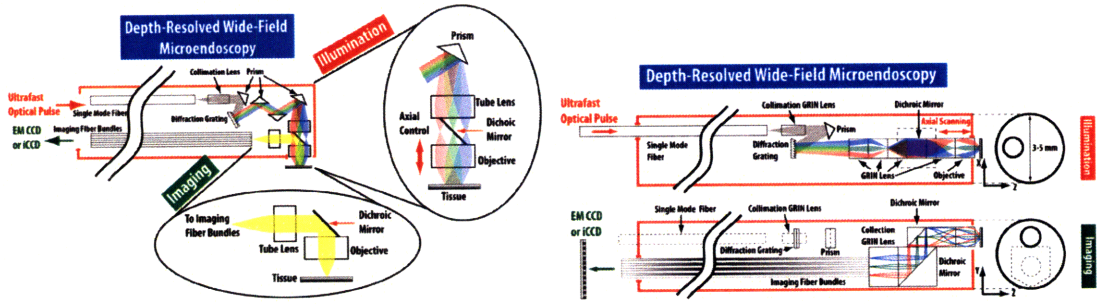

(a) **(b)**

Figure 6.3 Schematic diagram for TPE wide-field microendoscopy: (a) Side-viewing type and (b) front-viewing type

6.2.5. Developing High-Speed 3D Lithography with Dynamic Mask Generation

The 3D lithographic microfabrication system described in this thesis used fixed mask. While it is sufficient for proof-of-concept experiments, it is not efficient for mass-production. For 3D fabrication, each layer has different pattern, and 3D microstructure is built by stacking these different patterns. High-speed lateral pattern generator is required in order not to delay the fabrication process. Several state-of-art devices to enable high-speed pattern generation have been proposed: DMD with DLP, SLM, and MA. In case of SLM, the fixed mask is replaced with transmission type mask. Devices with reflective type mask, such as DMD with DLP and MA, need extra apparatus, i.e. polarization beam splitter (PBS) that reflects p-polarized (or s-polarized) beam to digital mirror device. Quarter-wave plate (QWP) is placed between PBS and DMD so that the polarizations of incident beam and reflected beam are orthogonal. The patterned s-polarized (or p-polarized) beam reflected from DMD is transmitted through PBS and delivered to tube lens and the objective. Figure 6.4 depicts this mechanism.

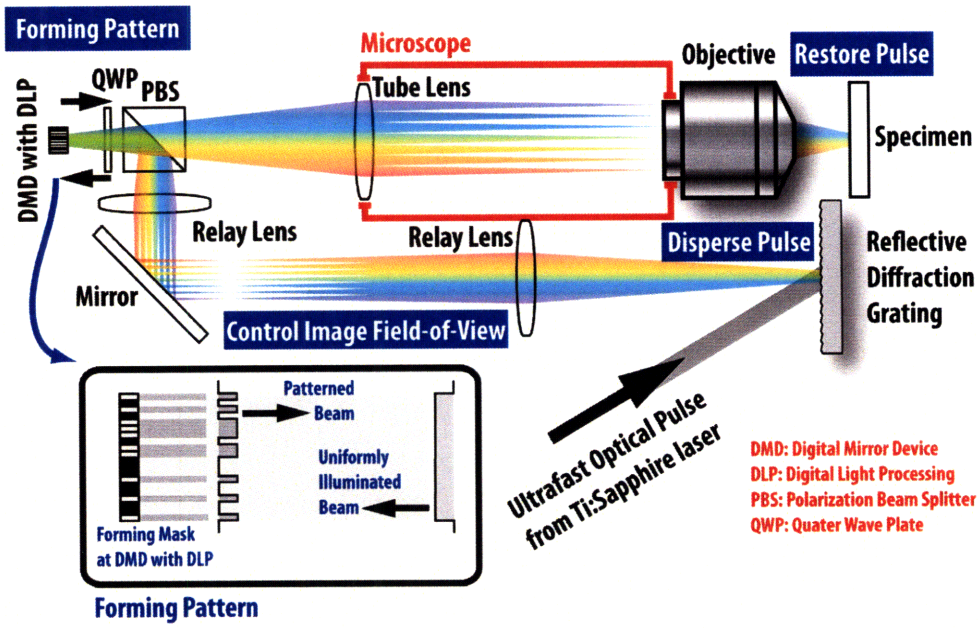

Figure 6.4 3D lithographic microfabrication with DMD with DLP

References

1. B. Bailey, D. L. Farkas, D. L. Taylor, and F. Lanni, "Enhancement of Axial Resolution in Fluorescence Microscopy by Standing-Wave Excitation," Nature **366**, 44-48 (1993).
2. B. Hebert, S. Costantino, and P. W. Wiseman, "Spatiotemporal image correlation Spectroscopy (STICS) theory, verification, and application to protein velocity mapping in living CHO cells," Biophysical Journal **88**, 3601-3614 (2005).
3. R. P. Kulkarni, D. D. Wu, M. E. Davis, and S. E. Fraser, "Quantitating intracellular transport of polyplexes by spatio-temporal image correlation spectroscopy," Proceedings of the National Academy of Sciences of the United States of America **102**, 7523-7528 (2005).
4. D. L. Kolin, D. Ronis, and P. W. Wiseman, "k-Space image correlation spectroscopy: A method for accurate transport measurements independent of fluorophore photophysics," Biophysical Journal **91**, 3061-3075 (2006).
5. N. Durisic, A. I. Bachir, D. L. Kolin, B. Hebert, B. C. Lagerholm, P. Grutter, and P. W. Wiseman, "Detection and correction of blinking bias in image correlation transport measurements of quantum dot tagged macromolecules," Biophysical Journal **93**, 1338-1346 (2007).
6. W. Gobel, J. N. D. Kerr, A. Nimmerjahn, and F. Helmchen, "Miniaturized two-photon microscope based on a flexible coherent fiber bundle and a gradient-index lens objective," Optics Letters **29**, 2521-2523 (2004).
7. W. Piyawattanametha, R. P. J. Barretto, T. H. Ko, B. A. Flusberg, E. D. Cocker, H. J. Ra, D. S. Lee, O. Solgaard, and M. J. Schnitzer, "Fast-scanning two-photon fluorescence imaging based on a microelectromechanical systems two-dimensional scanning mirror," Optics Letters **31**, 2018-2020 (2006).

8. L. Fu, A. Jain, C. Cranfield, H. K. Xie, and M. Gu, "Three-dimensional nonlinear optical endoscopy," Journal of Biomedical Optics **12**, - (2007).